



# University of HUDDERSFIELD

## University of Huddersfield Repository

Zhang, Tao

A NEW METHOD OF WAVELENGTH SCANNING INTERFEROMETRY FOR INSPECTING SURFACES WITH MULTI-SIDE HIGH-SLOPED FACETS

### Original Citation

Zhang, Tao (2018) A NEW METHOD OF WAVELENGTH SCANNING INTERFEROMETRY FOR INSPECTING SURFACES WITH MULTI-SIDE HIGH-SLOPED FACETS. Doctoral thesis, University of Huddersfield.

This version is available at <http://eprints.hud.ac.uk/id/eprint/34763/>

The University Repository is a digital collection of the research output of the University, available on Open Access. Copyright and Moral Rights for the items on this site are retained by the individual author and/or other copyright owners. Users may access full items free of charge; copies of full text items generally can be reproduced, displayed or performed and given to third parties in any format or medium for personal research or study, educational or not-for-profit purposes without prior permission or charge, provided:

- The authors, title and full bibliographic details is credited in any copy;
- A hyperlink and/or URL is included for the original metadata page; and
- The content is not changed in any way.

For more information, including our policy and submission procedure, please contact the Repository Team at: [E.mailbox@hud.ac.uk](mailto:E.mailbox@hud.ac.uk).

<http://eprints.hud.ac.uk/>

**A NEW METHOD OF WAVELENGTH SCANNING  
INTERFEROMETRY FOR INSPECTING SURFACES WITH  
MULTI-SIDE HIGH-SLOPED FACETS**

**TAO ZHANG**

A thesis submitted to the University of Huddersfield in partial fulfilment of the requirements for  
the degree of Doctor of Philosophy

The University of Huddersfield

July 2018

## Copyright statement

- i. The author of this thesis (including any appendices and/or schedules to this thesis) owns any copyright in it (the “Copyright”) and he has given The University of Huddersfield the right to use such copyright for any administrative, promotional, educational and/or teaching purposes.
- ii. Copies of this thesis, either in full or in extracts, may be made only in accordance with the regulations of the University Library. Details of these regulations may be obtained from the Librarian. This page must form part of any such copies made.
- iii. The ownership of any patents, designs, trademarks and any and all other intellectual property rights except for the Copyright (the “Intellectual Property Rights”) and any reproductions of copyright works, for example graphs and tables (“Reproductions”), which may be described in this thesis, may not be owned by the author and may be owned by third parties. Such Intellectual Property Rights and Reproductions cannot and must not be made available for use without the prior written permission of the owner(s) of the relevant Intellectual Property Rights and/or Reproductions

## **Acknowledgements**

I would like to express my sincere and profound gratitude to my supervisor Prof. Dame X. Jane Jiang for offering the opportunity as well as the guidance and support throughout the project. I deeply appreciate all her dedication!

I also have to express my deepest appreciation to my co-supervisors Dr. Feng Gao and Dr. Haydn Martin for the encouragement, valuable advice and technical guidance on my research work. You make me more confident to face the difficulties in my life!

I also need to thank all the members in the Centre for Precision Technologies & EPSRC Future Metrology Hub including Prof. Liam Blut, Prof. Paul Scott, Prof. Zonghua Zhang, Dr. Dawei Tang, Dr. Hongyu Ren, Dr. Wenhan Zeng, Dr. Shan Lou, Dr. Hussam Muhamedsalih, Dr. Prashant Kumar, Mr. Yongjia Xu, Mr. Duo Li, Mr. Chris Dawson, Mr. Christian Young, Mr. Ashley Cusack, Ms Yue Liu, I cannot name so many! I really appreciate all the precious help and company from them during this period.

Thanks also go to Dr. Graeme Greaves of MIAMI, Mr. James Rooney, both within University of Huddersfield, as well as Jonathan Kiernan, Director of Opus Metrology, for the help in my calibration work.

Last but definitely not the least, I would like to thank my mum and dad, my two sisters, my two nephews and my niece. Without your support, I could never have completed this work.

## Abstract

With the development of modern advanced manufacturing technologies, the requirements for ultra-precision structured surfaces are increasing rapidly for both high value-added products and scientific research. Examples of the components encompassing the structures include brightness enhancement film (BEF), optical gratings and so forth. Besides, specially designed structured surfaces, namely metamaterials can lead to specified desirable coherence, angular or spatial characteristics that the natural materials do not possess. This promising field attracts a large amount of funding and investments. However, owing to a lack of effective means of inspecting the structured surfaces, the manufacturing process is heavily reliant on the experience of fabrication operators adopting an expensive trial-and-error approach, resulting in high scrap rates up to 50-70% of the manufactured items. Therefore, overcoming this challenge becomes increasingly valuable.

The thesis proposes a novel methodology to tackle this challenge by setting up an apparatus encompassing multiple measurement probes to attain the dataset for each facet of the structured surface and then blending the acquired datasets together, based on the relative location of the probes, which is achieved via the system calibration. The method relies on wavelength scanning interferometry (WSI), which can achieve areal measurement with axial resolutions approaching the nanometre without the requirement for the mechanical scanning of either the sample or optics, unlike comparable techniques such as coherence scanning interferometry (CSI). This lack of mechanical scanning opens up the possibility of using a multi-probe optics system to provide simultaneous measurement with multi adjacent fields of view.

The thesis presents a proof-of-principle demonstration of a dual-probe wavelength scanning interferometry (DPWSI) system capable of measuring near-right-angle V-groove structures in a single measurement acquisition. The optical system comprises dual probes, with orthogonal measurement planes. For a given probe, a range of V-groove angles is measurable, limited by the acceptance angle of the objective lenses employed. This range can be expanded further by designing equivalent probe heads with varying angular separation. More complicated structured surfaces can be inspected by increasing the number of probes. The fringe analysis algorithms for WSI are discussed in detail, some improvements are proposed, and experimental validation is conducted. The scheme for calibrating the DPWSI system and obtaining the relative location

between the probes to achieve the whole topography is implemented and presented in full. The appraisal of the DPWSI system is also carried out using a multi-step diamond-turned specimen and a sawtooth brightness enhancement film (BEF). The results showed that the proposed method could achieve the inspection of the near-right-angle V-groove structures with submicrometre scale vertical resolution and micrometre level lateral resolution.

# Table of Contents

<b>Copyright statement</b> .....	<b>1</b>
<b>Acknowledgements</b> .....	<b>2</b>
<b>Abstract</b> .....	<b>3</b>
<b>Table of Contents</b> .....	<b>5</b>
<b>List of Tables</b> .....	<b>9</b>
<b>List of Figures</b> .....	<b>10</b>
<b>List of abbreviations</b> .....	<b>13</b>
<b>1 Introduction</b> .....	<b>16</b>
1.1 Overview .....	16
1.2 Measurement of structured surfaces .....	18
1.2.1 Background .....	18
1.2.2 State of the art .....	19
1.3 Motivation .....	23
1.4 Aim .....	23
1.5 Research objectives .....	23
1.6 Thesis structure.....	24
1.7 Novel contributions .....	25
1.8 Publication.....	25
<b>2 Surface Metrology</b> .....	<b>26</b>
2.1 Introduction .....	26
2.2 Surface metrology.....	26
2.2.1 Overview .....	26
2.2.2 Development of instrumentation.....	27
2.2.3 Filtration .....	28
2.2.4 Characterisation.....	29
2.3 Instrumentation technologies for surface metrology .....	30
2.3.1 Overview .....	30
2.3.2 Contact method .....	30
Stylus profilometer .....	31
Scanning probe microscopy .....	32
2.3.3 Non-contact methods.....	35

Optical scatterometry .....	35
Focus variation .....	37
Confocal Microscopy .....	40
2.4 Comparison of various types of instruments .....	42
2.5 Summary.....	43
<b>3 Optical interferometry .....</b>	<b>44</b>
3.1 Introduction .....	44
3.2 Light interference and coherence .....	44
3.3 Phase-shifting interferometry .....	45
3.4 White light interferometry .....	47
3.5 Dual-wavelength and multi-wavelength interferometry.....	50
3.6 Wavelength scanning interferometry.....	51
3.7 Dispersive interferometry .....	54
3.8 Summary.....	55
<b>4 Subaperture stitching interferometry .....</b>	<b>56</b>
4.1 Overview .....	56
4.2 Image stitching .....	56
4.2.1 Image registration.....	56
4.2.2 Image blending .....	58
4.3 Stitching interferometry.....	60
4.4 Summary.....	61
<b>5 Dual-probe wavelength scanning interferometry measurement system .....</b>	<b>62</b>
5.1 Introduction .....	62
5.2 System scheme .....	62
5.3 Light source .....	63
5.4 Console .....	66
5.4.1 AOTF controller.....	66
5.4.2 Software console .....	67
5.5 Interferometer module .....	69
5.5.1 Interferometric objectives .....	69
5.5.2 Objective selection .....	73
5.5.3 Alignment strategy .....	74
5.6 Summary.....	78
<b>6 Fringe analysis .....</b>	<b>79</b>
6.1 Introduction .....	79

6.2	Interferogram processing principle.....	79
6.3	Simulation and experimental results.....	84
6.3.1	Simulation results.....	84
6.3.2	Filter validation.....	92
6.4	Vertical calibration for the probes.....	98
6.5	Summary.....	99
<b>7</b>	<b>DPWSI system calibration.....</b>	<b>101</b>
7.1	Introduction.....	101
7.2	System calibration principle.....	101
7.3	Artefact manufacturing.....	103
7.3.1	Focused ion beam.....	104
7.3.2	Machining of the artefact.....	105
7.4	Acquisition of the reference topography.....	107
7.4.1	Scanning electron microscopy.....	107
7.4.2	SEM dataset processing.....	109
7.4.3	Topography dataset processing.....	111
7.4.4	Outlier filtration.....	114
7.4.5	Surface fitting.....	118
7.4.6	Reference topography blending.....	119
7.5	Measurement results with DPWSI probes.....	120
7.6	3D registration.....	122
7.6.1	Overview.....	122
7.6.2	Iterative closest points (ICP) algorithm.....	124
7.6.3	Improvement of the lateral calibration.....	126
7.6.4	System calibration.....	127
7.7	Measurement data fusion.....	127
7.8	Summary.....	130
<b>8</b>	<b>System verification.....</b>	<b>132</b>
8.1	Overview.....	132
8.2	A diamond-turned specimen.....	132
8.3	A sawtooth metallised prismatic film.....	134
8.4	Error source discussion.....	136
8.5	Summary.....	138

<b>9 Discussion, Conclusions and Future Work .....</b>	<b>139</b>
9.1 Introduction .....	139
9.2 Discussion.....	139
9.3 Conclusion.....	140
9.4 Future work.....	141
<b>References .....</b>	<b>144</b>
<b>Publications and Awards .....</b>	<b>154</b>
Refereed Journal Papers .....	154
Refereed Conference Papers .....	154
Awards .....	154
<b>Appendix A. Calibration certificate .....</b>	<b>155</b>
<b>Appendix B. The light box design .....</b>	<b>156</b>
Assembly.....	156
Front panel .....	157
Cover 157	
Back panel.....	158
AOTF holder .....	158
Base 159	
Collimation lens holder .....	159
Fibre coupler holder block .....	160
<b>Appendix C. A brief introduction about Muhamedsalih's thesis .....</b>	<b>161</b>
<b>Appendix D. Simulation code for fringe analysis .....</b>	<b>163</b>
<b>Appendix E. Feature extraction code .....</b>	<b>167</b>
SEM data.....	167
Topography data.....	168
<b>Appendix F. Taylor Hobson CCI 3000 specification .....</b>	<b>169</b>

**List of Tables**

Table 5.1 Performance targets.....62  
Table 5.2 Specifications for different objectives .....73  
Table 6.1 An example lookup table acquired by the simulation.....94

## List of Figures

Figure 1.1 A schematic diagram of a roll-to-roll manufacturing system. ....	16
Figure 1.2 Examples of the structured surfaces.. ....	19
Figure 1.3 Schematic of the deviation caused by the stylus tip. ....	20
Figure 1.4 Illustration of numerical aperture (NA) issue.. ....	21
Figure 1.5 The setup for the autostereoscopy-based three-dimensional on-machine measuring system.....	22
Figure 1.6 The scanning double side Fizeau interferometer. ....	22
Figure 2.1 Schematic of a stylus profiler. ....	31
Figure 2.2 Schematic of scanning tunnelling microscope.....	33
Figure 2.3 Schematic of an atomic force microscope. ....	35
Figure 2.4 The principle of optical scatterometry. ....	36
Figure 2.5 Schematic diagram of a focus variation instrument.....	38
Figure 2.6 The variation of the focus level with regard to the vertical position. ....	39
Figure 2.7 Schematic of confocal microscope. ....	41
Figure 2.8 Measurement scale and resolution for 3 different types of instruments. ....	43
Figure 3.1 Schematic of a phase-shifting interferometer. ....	46
Figure 3.2 Schematic of a white light interferometer based on a Mirau objective. ....	48
Figure 3.3 Interference signal of WLI.....	49
Figure 3.4 Wavelength scanning interferometer based on Michelson geometry. ....	52
Figure 3.5 A schematic setup of spectrally-resolved white light interferometry. ....	54
Figure 4.1 The subaperture stitching measurement. ....	60
Figure 5.1 Block diagram of the DPWSI system. ....	63
Figure 5.2 The mechanical design of the light source.....	64
Figure 5.3 Spectral characteristics of AOTF.....	65
Figure 5.4 A screenshot of the software.....	68
Figure 5.5 The wavelength scanning and data-capturing process.....	69
Figure 5.6 Different types of interference objectives.....	71
Figure 5.7 The assembled stage for holding the specimen. ....	75
Figure 5.8 Thorlabs CPS532-C2.....	76
Figure 5.9 The practical apparatus of the DPWSI system. ....	77

Figure 5.10 The interferograms captured by the two probes of the system. ....	77
Figure 6.1 (a). The captured interferograms. (b)(c). the intensity signals captured by 2 pixels. ...	79
Figure 6.2 Schematic of the traditional fringe analysis process.....	80
Figure 6.3 The signal in time domain and in frequency domain.....	84
Figure 6.4 The simulation results of the signal with different SNR processed by phase slope method with different windows.....	86
Figure 6.5 The simulation results of the signal with different SNR processed by height estimation through phase algorithm with different windows .....	88
Figure 6.6 The simulation results of the signal with different SNR multiplying a Hamming window (Hadamard product) processed by phase slope method and height estimation through phase algorithm with optimised windows.....	91
Figure 6.7 The measurement noise of a standard flat .....	92
Figure 6.8 The measurement result of a specimen with different methods. ....	97
Figure 6.9 An adaptive phase analysis algorithm for wavelength scanning interferometry. ....	98
Figure 6.10 The measurement result of a 178 nm standard step-height sample by one of the probes. ....	99
Figure 7.1 The coordinate systems of the probes.....	102
Figure 7.2 A schematic diagram of the calibration artefact with features on two adjoining faces .....	102
Figure 7.3 A schematic diagram of focused ion beam.....	104
Figure 7.4 The calibration artefact. ....	106
Figure 7.5 An interferogram of one polished face of the machined artefact. ....	106
Figure 7.6 A schematic diagram of a scanning electron microscope.....	108
Figure 7.7 The SEM images and the dimensions of the machined artefact.....	110
Figure 7.8 (a). the extracted edges of the selected features; (b). the fitted edges of the features after outlier removal. ....	111
Figure 7.9 The measurement result of the two faces using Taylor Hobson CCI 3000. ....	113
Figure 7.10 The extracted edges of the distinctive features. ....	114
Figure 7.11 The flow chart of the procedure for clustering filtering. ....	118
Figure 7.12 The reconstructed surface topography of the calibration artefact plotted with CloudCompare. ....	120
Figure 7.13 The measurement result of the two faces using DPWSI. ....	121

Figure 7.14 The extracted edges of the distinctive features. ....	122
Figure 7.15 The flow chart of the ICP process. ....	125
Figure 7.16 The measurement result of the calibration artefact by the DPWSI system plotted with CloudCompare. ....	128
Figure 7.17 (a) The residual error of the topography compared to the reference topography measured with Taylor Hobson CCI 3000 and FEI Quanta 200 3D FIB-SEM. (b) The extended 2D plots of the DPWSI topography .....	129
Figure 8.1 (a). A photo of the specimen. (b). A micrograph measured by optical microscope (Keyence VHX-500F). ....	132
Figure 8.2 The measurement result of the diamond turned specimen by DPWSI.....	133
Figure 8.3 The measurement result of the diamond turned specimen by Taylor Hobson CCI 3000 .....	134
Figure 8.4 The measurement result of a metallised prismatic film.....	135
Figure 8.5 Top. The comparison of the measured profiles. ....	136
Bottom. Plot of the residual error.....	136

## List of abbreviations

AM	Additive Manufacturing
R2R	Roll-to-Roll
CAD	Computer-Aided Design
BEF	Brightness Enhancement Film
LCD	Liquid Crystal Display
WDM	Wavelength Division Multiplexing
NA	Numerical Aperture
CSI	Coherence Scanning Interferometers
SPM	Scanning Probe Microscopy
WSI	Wavelength Scanning Interferometry
PSI	Phase Shifting Interferometry
WLI	White Light Interferometry
DPWSI	Dual-Probe Wavelength Scanning Interferometry
NPL	National Physics Laboratory
STM	Scanning Tunnelling Microscopy
AFM	Atomic Force Microscopy
LVDT	Linear Variable Differential Transformer

PZT	Piezoelectric Transducers
DOF	Depth of Field
CCD	Charge-Coupled Device
FOV	Field of View
PSF	Point Spread Function
NURBS	Non-Uniform Rational Basis Spline
LED	Light-Emitting Diodes
VSI	Vertical Scanning Interferometry
OPD	Optical Path Difference
DSP	Digital Signal Processing
SLED	Super Luminescent Light Emitting Diode
SRWLI	Spectrally-Resolved White Light Interferometry
RANSAC	RANdom SAmples Consensus
AOTF	Acousto Optical Tunable Filter
SDK	Software Development Kit
SNR	Signal to Noise Ratio
LUT	Lookup Table
FIB	Focused Ion Beam

LMIS	Liquid Metal Ion Sources
TEM	Transmission Electron Microscopy
SEM	Scanning Electron Microscopy
BSE	Backscatter Electron Detector
EBS	Diffracted Backscatter Detector
EDS	X-ray Detector
DIP	Digital Image Processing
SVD	Singular Value Decomposition
PCA	Principal Component Analysis
ICP	Iterative Closest Point
SASI	Subaperture Stitching Interferometry

# 1 Introduction

## 1.1 Overview

Surfaces, as interfaces between components, directly affect the product's functional behaviour (De Chiffre *et al.*, 2003; Whitehouse, 1997). Statistics show that 90% of the failures in engineering components are relevant to surfaces, owing to mechanisms such as wear, erosion and so forth (Blunt & Jiang, 2003). For example, an optical freeform surface is a decisive element in freeform optics, which is a branch in modern optics (Fess, 2012; Thompson & Rolland, 2012). Freeform surfaces can be utilised for directing the light propagation, such as beam shaping and illumination in a non-imaging field. Freeform surfaces are also widely used in imaging optics to increase the imaging quality and compactness of the optical system (Ye *et al.*, 2017). Ultraviolet objectives for lithography, head-mounted displays and off-axis three-mirror reflective imaging systems (Xie *et al.*, 2016) all adopt freeform surfaces. The high-precision manufacturing is crucial for the functioning of the freeform components. Therefore, surface metrology, as the inspection and verification technology for the fabricated specimens, has an increasingly large impact on manufacturing industries.

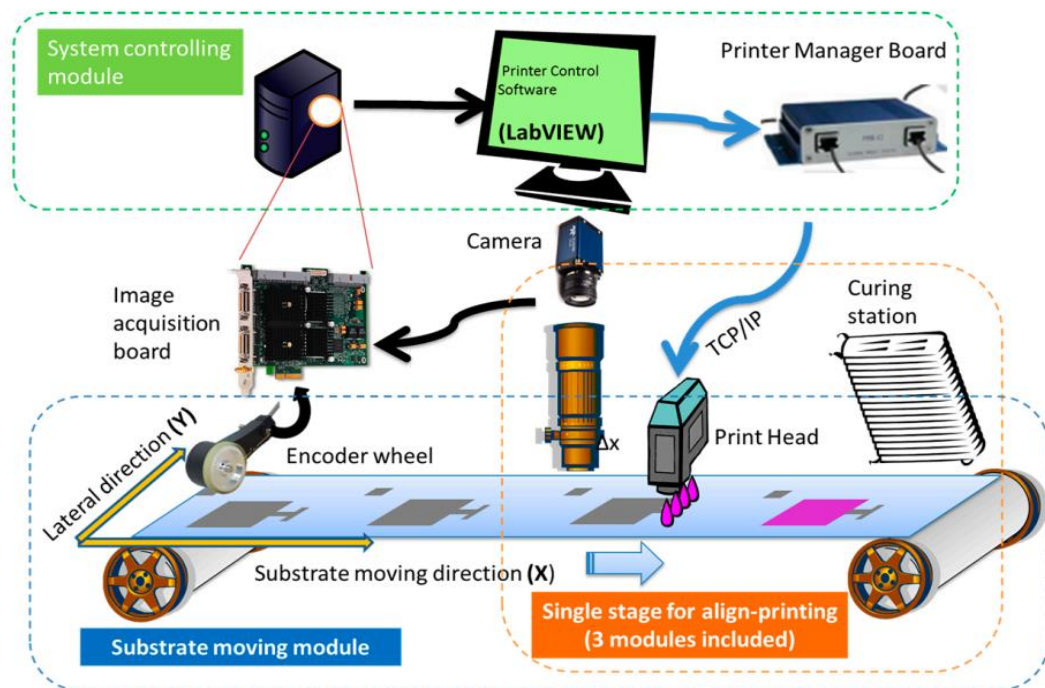


Figure 1.1 A schematic diagram of a roll-to-roll manufacturing system (adapted from Lin *et al.*, 2014).

The manufacturing technologies are continuously developing, generating numerous requirements for better inspection techniques (Jiang & Whitehouse, 2012). Advanced manufacturing technologies, such as diamond turning, micro milling, molecular nanotechnology, additive manufacturing (AM) and roll-to-roll (R2R) manufacturing, enable the fabrication of various ultra-precision surfaces such as surfaces with increasingly large areas, customised structures, as well as complex curvatures (Church & Zavada, 1975; Gregg *et al.*, 2005; Grimm *et al.*, 2015; Grous, 2013; Krebs *et al.*, 2010; Blunt *et al.*, 2013). Compared to the traditional subtractive manufacturing methodologies, AM represents an innovative process that binds materials together to produce components according to the 3D computer-aided design (CAD) models, usually layer by layer (Technologies & Terminology, 2012). AM is suitable for manufacturing high added-value components, as it reduces the part number and shortens the development cycle, which finds increasingly many applications in a wide variety of sectors including, but not limited to, the military, aerospace, automotive, and healthcare industries (Platform, 2014; Triantaphyllou *et al.*, 2015). Roll to roll (R2R) is a collection of fabrication technologies that involve continuous processing of a flexible substrate when it is conveyed between two rotating rolls of material, as illustrated in Figure 1.1 (Kimbrough *et al.*, 2015; Krebs *et al.*, 2010). Both additive and subtractive processes can be applied to build structures continuously. R2R manufacturing has the merits of high throughput and low cost, which distinguishes it from conventional manufacturing techniques because of the multiple steps involved. Although the initial investment is high to build up such an installation, the cost can often be recovered through mass fabrication. Today, R2R processing is employed in many industrial fields such as printed/flexible thin-film batteries (Keränen *et al.*, 2012), bendable displays (Gregg *et al.*, 2005), rollable solar panels (Schulz-Ruhtenberg *et al.*, 2014), flexible and large-area electronic devices (Søndergaard *et al.*, 2013; Willmann *et al.*, 2014), fibres and textiles, metallic foil and sheet fabrication, energy products in buildings, medical products, membranes, among others. The cutting-edge manufacturing technologies make the geometric features of the products become increasingly small, which makes surface texture one of the most critical functional indicators (Jiang *et al.*, 2007a). Currently, there are a great many of products with the surface specifically designed to realise a particular function, for example, the micro/nano electro-mechanical devices (Jiang & Whitehouse, 2012). At the phase of so-called “dawn of nanotechnology age”, microstructures and nanostructures are becoming increasingly important in the high added-value critical components and high-end manufacturing is rapidly shifting to the design and fabrication of these structures (Jiang *et al.*, 2007b). The surface finish of

the components is vital for system functionality. The importance of surface metrology, as a discipline for understanding the surface characterisations, is rising rapidly (Whitehouse, 2010). In turn, the development of manufacturing technology also advances the techniques used for surface metrology, enabling the production of more compact instruments with higher resolution and faster response.

## **1.2 Measurement of structured surfaces**

### **1.2.1 Background**

The development trend of surface metrology is in the direction of enabling the better measurement of structured surfaces and freeform surfaces (Jiang *et al.*, 2007b). Micro-fabricated structured surfaces with multi-side high sloped facets are widely applied across industries (Evans & Bryan, 1999; Zhang *et al.*, 2017). For example, brightness enhancement film (BEF) is a prismatic film frequently applied in liquid crystal displays (LCD) for power saving or thermal management. Optical gratings, which are comprised of periodic structures, find widespread application in optical instruments, such as spectrometers, lasers, wavelength division multiplexing (WDM) devices, and so forth (Fang *et al.*, 2016). Specially designed structured surfaces, namely metamaterials, can result in specified desirable coherence, angular, or spatial characteristics that the natural materials do not possess and are very promising in optics, terahertz technology, etc. (Leskova *et al.*, 2007; Maradudin, 2011). Some of the representative products with the structured surfaces are shown in Figure 1.2, such as an optical grating, a brightness enhancement film (BEF) comprising micro-V-groove structures, a Fresnel lens, and a PVC film with micropyramidal arrays embossed on it. It is worth mentioning that a large proportion of the structured surfaces feature nearly orthogonal sidewalls. However, owing to the manufacturing process, which is heavily reliant on the experience of fabrication workers adopting an expensive trial-and-error approach, the manufactured items are reported to suffer from high scrap rates up to 50-70% (Singleton *et al.*, 2002). Therefore, overcoming this challenge becomes increasingly valuable.

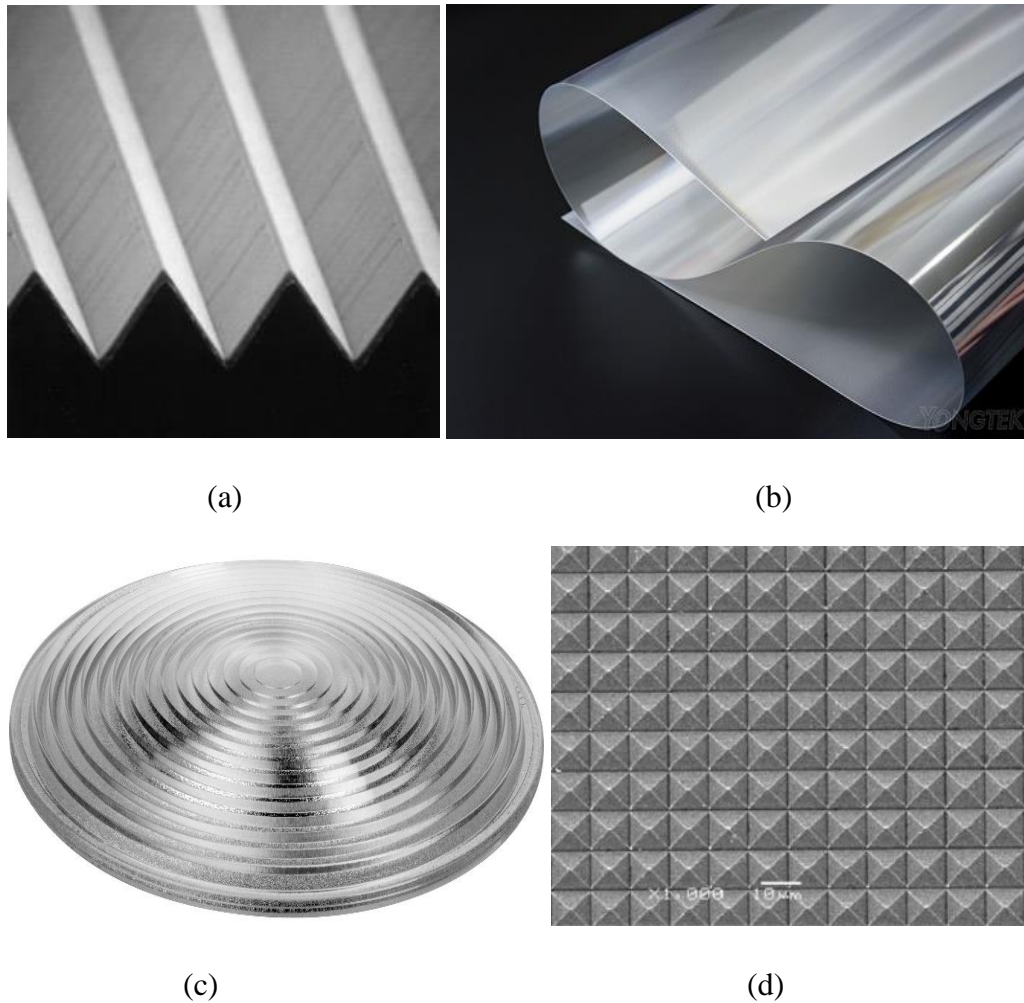


Figure 1.2 Examples of the structured surfaces: (a). an optical grating; (b). a brightness enhancement film (BEF) comprising micro-V-groove structures; (c). a Fresnel lens; and (d). a PVC film with micropyramidal arrays embossed on it.

### 1.2.2 State of the art

Currently, structured surfaces are mainly inspected using the contact stylus profilometer and optical instruments. Although the stylus profilometer features high vertical resolution (nanometre level), it is potentially destructive and, regarding areal measurement, it is relatively time-consuming (Bennett & Dancy, 1981; Vorburger *et al.*, 2007). In addition, the size of the stylus tip might induce large deviations when measuring microstructures with a high aspect ratio (Malacara, 2007), as illustrated in Figure 1.3. Optical scanning techniques, such as confocal microscopes, focus variation instruments, and interferometers, are commonly confined by the well-defined numerical aperture (NA) issue, namely the maximum measurable angle is limited by the NA (Hecht, 2016). The inspection difficulty increases with the angle getting larger, as illustrated in Figure 1.4, the measurement difficulties rank in the order of blue, green, yellow and red from low

to high. Either the data for the areas of the surface that scatter light beyond the NA is missing, or the resolution is reduced for the areas where the measurement angle is large. Sometimes, it is even impossible to obtain accurate topography. For example, some highly repeatable systematic errors are reported when measuring these types of structures using coherence scanning interferometers (CSI) (Gao *et al.*, 2006; Gao *et al.*, 2007). Other instruments are also restricted in this area. SEM provides high lateral resolution when observing the structures; however, it cannot acquire the height information (Tafti *et al.*, 2015). The powerful scanning probe microscope (SPM) family of instruments are restricted by the measurable axial range (normally just several microns) in this area (Ju *et al.*, 2012; Schneir *et al.*, 1989). Some researchers have attempted to tackle this problem. Purcell *et al.* presented a method by enlarging the NA using index matching liquid (Purcell *et al.*, 2010). Li *et al.* achieved fast on-machine measurement by developing a compact autostereoscopy-based three-dimensional on-machine measuring (ATDOM) system illustrated in Figure 1.5 (Li *et al.*, 2014; Li *et al.*, 2015). However, the measurement repeatability is low. Jansen *et al.* developed a scanning Fizeau interferometer, which measures the thickness and flatness of a silicon wafer by simultaneously probing both the front and back sides (Jansen *et al.*, 2004), as shown in Figure 1.6. Although the system is designed for inspecting two nearly parallel faces, it provides confidence that the topography acquisition of the structured surfaces with multi-side high-sloped facets can potentially be fulfilled by utilising a measurement system encompassing two or more interferometers.

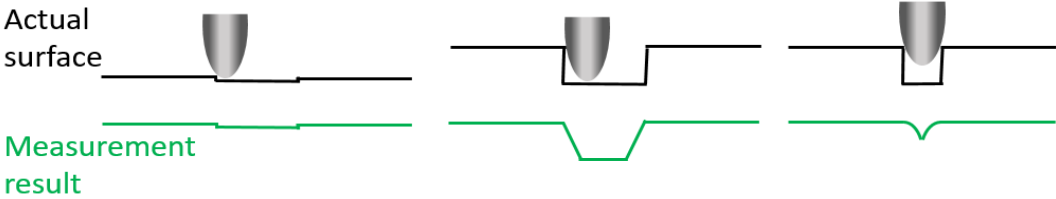


Figure 1.3 Schematic of the deviation caused by the stylus tip.

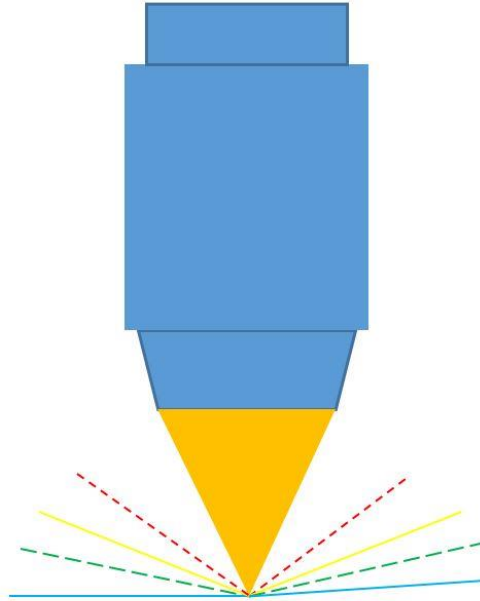


Figure 1.4 Illustration of numerical aperture (NA) issue. The measurement difficulty ranks in the order of blue, green, yellow, and red from low to high.

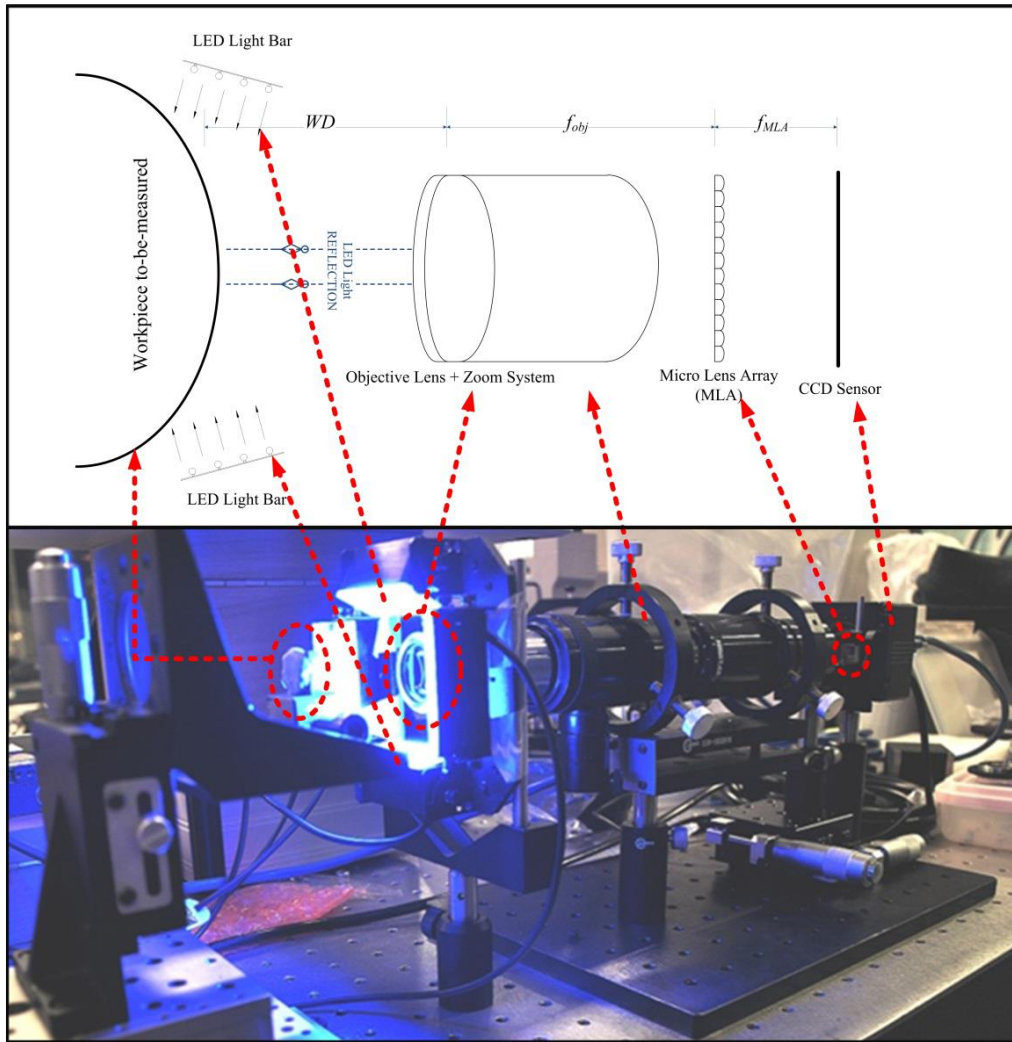


Figure 1.5 The setup for the autostereoscopy-based three-dimensional on-machine measuring system (ATDOM, adapted from Li *et al.*, 2014).

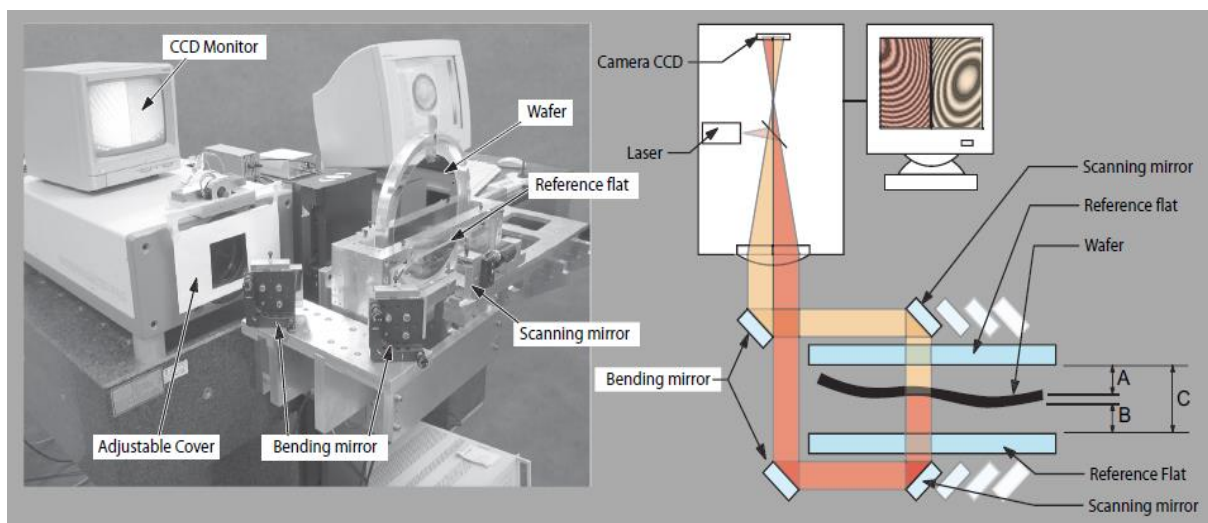


Figure 1.6 The scanning double-sided Fizeau interferometer (adapted from Jansen *et al.*, 2004).

### 1.3 Motivation

Jiang *et al.* of the University of Huddersfield developed a fast topography acquisition system based on wavelength scanning interferometry (WSI) with compensation of environmental noise (Jiang *et al.*, 2010). This system was a success in the inspection of surfaces with the presence of environmental disturbances such as in the workshop or for on-line measurement (Jiang *et al.*, 2010; Blunt *et al.*, 2013; Gao *et al.*, 2012). However, the system was not able to measure structured surfaces, comprising multi-side high-sloped facets (the measurable slope is dependent on the NA of the objective adopted), owing to the above-mentioned limited acceptance angle issue. Like many other optical inspection approaches, by tilting the interferometer, only the facets in one direction could be measured. It was incapable of inspecting all the facets in different orientations and blending them together to obtain the whole topography because, between different measurements, the relative location was unidentified, which makes it impossible to set up the spatial relationship between these measurement results. This thesis aims to tackle this problem through developing an opto-mechanical system based on the WSI technique to enable the measurement of a structured surface encompassing multi-side high-sloped facets by simultaneously carrying out measurements in different directions and then blending the datasets together to achieve the whole topography.

### 1.4 Aim

The aim of the thesis is to investigate the potential of applying wavelength scanning interferometry (WSI) in inspecting structured surfaces comprising multi-side high-sloped facets. The proof-of-principle study mainly focuses on the inspection of near-right-angle V-groove structured surfaces. The measurable dihedral angle is dependent on the NA of the objectives, the range in this thesis is between  $(90 - 5.7)^\circ$  and  $(90 + 5.7)^\circ$ .

### 1.5 Research objectives

- To develop an improved WSI system incorporating two measurement probes to simultaneously inspect the two sidewalls of near-right-angle V-groove structured surfaces.
- To investigate, improve and optimise the fringe analysis algorithm for WSI.

- To develop and verify a system calibration scheme for achieving relative position between the probes of the measurement system to obtain the whole topography of near-right-angle V-groove structured surfaces.

## **1.6 Thesis structure**

The thesis presents the development of an improved WSI system for obtaining the topography of double-sided near-right-angle structured surfaces. The layout of the thesis is as below:

Chapter 2 briefly describes the development of the discipline of surface metrology and its applications in manufacturing industries, including some important concepts and terminologies. Some representative instrumentation techniques for obtaining surface topographic information are then reviewed, including both contact and optical technologies (excluding interferometric techniques).

Chapter 3 describes the basics of the interference phenomenon between two beams of light and the coherence. Then different types of mainstream interferometers are reviewed in detail, such as phase-shifting interferometry (PSI), white light interferometry (WLI), wavelength scanning interferometry (WSI), etc.

Chapter 4 discusses subaperture stitching interferometry, which combines the image stitching technique and interferometry to realise large-scale measurement. Subaperture stitching interferometry has some similarities to this study.

Chapter 5 presents the design and implementation of the apparatus of the dual-probe wavelength scanning interferometry (DPWSI) system for measuring near-right-angle V-groove structured surfaces in detail.

Chapter 6 investigates the fringe analysis algorithm for WSI to retrieve the height information, mainly focusing on the phase-slope method and the height estimation through the fringe phase algorithm. This chapter starts by reviewing the principle of the algorithms and then proposes a method to improve the performance by optimising the filter design based on simulation. Experimental validation is performed and the results support the proposal.

Chapter 7 presents the DPWSI system calibration process to establish the positional relationship between the two probes for blending the two measurement datasets together to attain the whole

topography. A novel methodology based on a combination of high-precision instruments and 3D registration algorithm is proposed and implemented.

Chapter 8 presents verification of the investigated apparatus and implemented methodologies using some specimens containing the target microstructures.

Chapter 9 makes an overall summarisation and conclusion of the thesis. The directions for further investigation and improvement are also considered.

## **1.7 Novel contributions**

The work undertaken in completing this thesis has produced the novel contributions listed as below:

- Development and demonstration of an optic-mechanical system encompassing two wavelength scanning interferometers to simultaneously probe the two facets of near-right-angle V-groove structured surfaces.
- Investigation and improvement of the fringe analysis algorithm for WSI.
- Investigation, development, and verification of a system calibration scheme for acquiring relative position between the probes of the measurement system to enable high-precision topography acquisition of near-right-angle V-groove structured surfaces.

## **1.8 Publication**

The work in this thesis has produced three peer-reviewed journal papers and one conference paper. A full publication list may be found in the “Publications and Awards” section at the end of this thesis.

## 2 Surface Metrology

### 2.1 Introduction

This chapter provides an overview of the discipline of surface metrology and its applications in manufacturing industries. Some important concepts and terminologies used are also presented.

The instrumentation technologies for obtaining surface topographic information are discussed, including both contact and non-contact technologies and excluding interferometric techniques, which are discussed in detail in the next chapter.

### 2.2 Surface metrology

#### 2.2.1 Overview

Surface metrology is a branch discipline of metrology that is focused on the measurement of small-scale features of surfaces (Hocken *et al.*, 2005; Whitehouse, 1997; Whitehouse, 2004). Surface metrology studies the deviation of a manufactured item from its predefined shape. Jiang *et al.* (2007a, p. 2049) gave another definition of surface metrology as “*the science of measuring small-scale geometrical features on surfaces: the topography of the surface*” (Jiang *et al.*, 2007a).

Surface measurement can usually be decomposed into two essential stages: physically acquiring surface topography with instrumentation, associated with the subsequent post-processing of the obtained information (i.e., characterisation). Although surface metrology is a relatively recent scientific subject, it has gone through a complicated and tortuous development. The main driving force has been the technological developments in other sectors. Instrumentation technology has been driven by the advances in optics, sensory technology, digital technology, etc. Characterisation has been advanced by the development in computer science, numerical techniques such as digital filtering, wavelet theory, together with algorithm and software technologies (Jiang *et al.*, 2007a).

The genesis of surface metrology occurred with investigations into the friction between surfaces of a moving body centuries ago. The public interest in surface metrology originates primarily as a result of the necessity of controlling the production of armaments during World War II and the fabrication of domestic products and appliances after that (Jiang *et al.*, 2007a). Technological developments had brought disruptive changes, resulting in a fundamental advancement in the approach to surface metrology. For example, the development of instrumentation and digital

technology has led to several paradigm shifts. Currently, at the phase of ‘the dawn of the nanotechnology era’ and with the development of the next generation of ultra-precision surfaces, the discipline of surface metrology is witnessing an enormous paradigm shift: from profile to areal characterisation, from stochastic to structured surfaces, and from simple geometries to complex free-form geometries, all ranging from the millimetre to sub-submic scales (Jiang *et al.*, 2007b). The historical development and current paradigm shifts are discussed with regard to the following aspects, namely instrumentation, filtration, characterisation, and standardisation respectively in detail.

### **2.2.2 Development of instrumentation**

Surfaces were initially assessed in rudimentary ways, by either a fingernail or by eye, that were both subjective but effective only when conducted by a skilled operator. With the development of more advanced manufacturing techniques, the textural features of the surface became increasingly small and went far beyond the range capable of being assessed qualitatively by ‘touch and see’. Therefore, instrumentation was required to magnify geometrical features normal to the surface so they could be inspected.

Tomlinson at the National Physics Laboratory (NPL) successfully achieved a magnification of approximately 30X for the first time with a galvanometer associated with a mirror (Tomlinson, 1919). Schmalz was the first person seriously considering instrumentation, adopting both optical and tactile methods to inspect surfaces (Schmalz, 1936). After that, a number of companies entered in this field and Taylor Hobson in the UK developed the first commercial instrument ‘the Talysurf 1’, which included a chart showing a roughness profile to achieve quantitative assessment.

The emergence of the digital age dramatically enriched the characterisation parameters and analytical methods. The instrument that was able to measure both surface texture and form with a single profile measurement was devised (Garratt, 1977) and was subsequently commercialised by Taylor Hobson. However, the instrument had a very limited vertical measurable range, typically only 100–300  $\mu\text{m}$ . The phase grating interferometer transducer individually developed by Taylor Hobson in the UK (Mansfield & Buehring 1997) and Jiang in China (Jiang, 1995) significantly improved the range and resolution to 24 mm and 0.1 nm, respectively.

With the development of various instrumentation techniques in the past decades, there are many different types of commercial instruments that adopt a wide range of principles, including but not

limited to contacting stylus, phase-shifting interferometry (PSI), coherence scanning interferometry (CSI), confocal microscopy, focus variation, structured light techniques, scanning tunnelling microscopy (STM), and atomic force microscopy (AFM). Instruments dealing with the two big challenges, namely structured and freeform surfaces, are also under development.

### 2.2.3 Filtration

According to the wavelength bands, surface texture can be separated into form, waviness, and roughness, which result from the design, machine tool, and the fabrication process, respectively (ISO 25178-2: 2012). Filtration is the means by which the surface features of interest can be extracted from the measurement result for subsequent analysis.

Waviness is the most difficult wavelength band to define because it has no natural wavelength boundaries. Two competing filter systems, namely the mean line system (M-system, Reason, 1961) and the envelope system (E-system, von Weingraber, 1956) were presented to separate the waviness from the profile with a graphical and a mechanical method, respectively. The M-system was originally implemented with a completely analogue 2CR filter as a two-stage capacitor-resistance network, which strongly distorts profile features, while the E-system adopted a mechanical rolling circle filter.

With the advent of the digital age, digital techniques such as digital filtering, find widespread applications in surface metrology owing to the large advancement of digital computing (Whitehouse & Archard, 1969). Several types of profile filters had been developed and were standardised by the International Standards Organisation (ISO), including but not limited to the following:

1. Linear filters. The mean-line filters (M-system) including Gaussian filter, Spline filter (Krystek, 1996; Krystek, 1997), and the Spline-wavelet filter (Jiang *et al.*, 2000) are all classified into this class.
2. Morphological filters. The envelope filters (E-system) including closing and opening filters are categorised into this type.
3. Robust filters. Robust filters with regard to specific profile phenomena such as steps, spikes, scratches, etc., include the robust Spline filter (Zeng *et al.*, 2011) and the robust Gaussian filter (Seewig, 2005).

4. Segmentation filters. Filters segmenting a profile into portions while conforming to specific rules (Dunn & Higgins, 1995). The motif approach is classified into this class.

The concept of scale-limited surface was proposed for areal surface characterisation. The concept is primarily based on the following types of filters or operators:

- S-filter is a filter that removes small-scale lateral components from the surface.
- L-filter is a filter that removes large-scale lateral constituents of the surface.
- F-operator is an operator that removes the nominal form from the surface. It is achieved by removing the optimally fitted form from the surface.

The result obtained by applying a combination of an S-filter and an F-operator on a surface is called an SF surface while the result acquired after applying an L-filter on an SF surface is called an SL surface. SF and SL surfaces can both be called scale-limited surfaces.

The filtering techniques, such as those ones achieving multi-scale analysis based on wavelet theory (Chen *et al.*, 1995) and the ones for fractal analysis (Brown *et al.*, 1993; Jiang *et al.*, 2007a), are under development for more advanced metrology technologies.

#### **2.2.4 Characterisation**

Surface metrology is tightly related to other disciplines such as machine tool, fabrication processes, quality assessment of manufactured components, tribology and precision engineering, and so forth. The measurement of surface texture is very useful. For example, surface roughness can be applied for evaluating wear condition of machine tools (Coker & Shin, 1996). Another example is that surface texture of thin films can be used to characterise defects in the films, reducing unnecessary losses (Elrawemi *et al.*, 2015).

Surface texture was considered to be characterised quantitatively by surface texture parameters. In the beginning, two extreme camps existed. One camp thought that a single number should be utilised to evaluate surface texture while the other camp argued that a single number is too simplistic and proposed to characterise the surface with a profile. Later, Abbott and Firestone presented a simple curve (the Abbott–Firestone curve) to represent the surface, from which

realistic numbers could be determined and applied to control the manufacturing based on the application of the surface (Abbott & Firestone, 1933).

In the 1940s, various texture components, namely form, waviness and roughness, were identified according to the wavelength bands. A large variety of filters were then developed to separate the components. The approach of the digital age brought the so-called “Parameter Rash” (Whitehouse, 1982). A multitude of parameters was developed for evaluating the performance or process control, which also led to difficulties in terms of standardisation.

Although profile parameters provide a means of controlling the manufacturing process, they cannot diagnose the functional performance of the manufactured items intuitively. Areal surface characterisation attempted to depict the fundamental and functional features of the surface topography, such as texture shape and direction assessment, estimation of feature properties and differentiation between adjoining and separated features. Areal parameters can be divided into two classes, namely field and feature parameter sets (Blunt & Jiang, 2003). A field parameter set is based on statistics while a feature parameter set is based on the segmentation algorithm. Field parameter sets, including S-parameter and V-parameter sets, have been standardised (Jiang *et al.*, 2007b). Feature parameter sets are widely adopted to characterise structured surfaces. The characterisation methods for freeform surfaces are still under development, owing to the geometrical complexities.

## **2.3 Instrumentation technologies for surface metrology**

### **2.3.1 Overview**

Surface metrology instruments are based on either contact or non-contact methods (Whitehouse, 2010). This section specifically discusses the principle of the representative techniques based on contact method such as stylus profilometer, scanning probe microscopy (SPM), etc., associated with some typical techniques based on non-contact methods such as optical scatterometry, focus variation, confocal microscopy, and so forth.

### **2.3.2 Contact method**

The instruments based on contact method are usually called contact profilers, as they perform the measurement by scanning across the surface of the inspected specimen with a stylus probe. Stylus profilometers and SPM are typical and common representatives of contact profilers. These

instruments feature high lateral resolution but relatively low measurement speed (Conroy & Armstrong, 2005). The techniques are discussed in more detail in the succeeding sections.

### Stylus profilometer

The stylus profilometer, which is relatively inexpensive and simple to use, is a standard in many optical and mechanical workshops (Bennett & Dancy, 1981). Stylus profilometers measure by moving a small-tipped stylus over the surface and obtain the surface profile by sensing the height variations of the stylus tip in a way resembling a phonograph (Teague *et al.*, 1982). The detection of the vertical movement of the stylus is typically accomplished by a linear variable differential transformer (LVDT) and the signal is converted into height information, as illustrated in Figure 2.1. The lateral resolution of surface profilometers is partially determined by the stylus, which is made of a material with high hardness, such as diamond, featuring a tiny tip with the curvature radius ranging from 0.05 to 50  $\mu\text{m}$ . In addition, the stylus load should be carefully chosen to ensure that the surface under test is not deformed while the stylus tip is kept on the surface. A sharper tip with smaller radius makes it easier for the stylus to follow the surface shape but, when the tip is too sharp, the local force on the surface posed by the stylus tip may be so strong that the surface gets locally deformed. If the deformation is elastic, the surface profile may be inaccurate. Otherwise, if the deformation is plastic, the specimen may be permanently damaged and the surface profile would also be inaccurate (Malacara, 2007). The new low force technology with tip load lower than a milligram enables the measurement of soft materials.

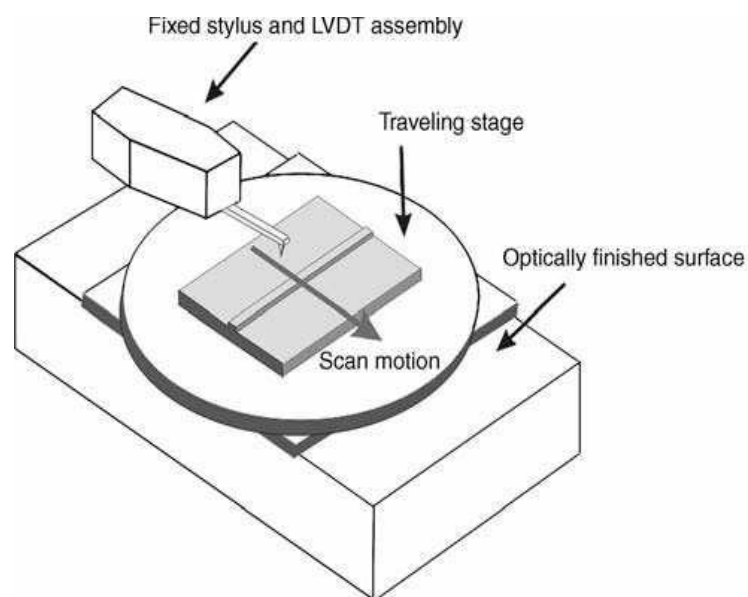


Figure 2.1 Schematic of a stylus profiler. (adapted from Malacara, 2007)

Surface shape and sampling interval between data points have a large impact on the lateral resolution of stylus profilometers, as the measurement result of these instruments is the convolution of the size and shape of the stylus tip with the surface profile. The maximum measurable aspect ratio of the trenches, equivalently the maximum measurable facet angle is determined by the cone angle of the stylus tip. Sharp styli have been developed for measuring high-aspect-ratio structures. Specialised tip geometries, such as “chisel-type”, are also fabricated to inspect challenging specimens (Tian, *et al.*, 2007). Stylus profilometers are usually verified with traceable height and roughness standards. A deconvolution operation can also be applied to correct the measurement results in the critical areas, such as the edge areas.

Owing to the large measurable range, as well as high precision, stylus profilometers are widely adopted in industries, such as the semiconductor industry.

### **Scanning probe microscopy**

Scanning probe microscope (SPM), which was developed after the stylus instrument, works by scanning a fine tip across the test surface in close proximity and can achieve atomic-scale resolution (Wiesendanger, 1994). It is widely applied in ultra-precision industries such as nanotechnology, semiconductor industries, etc. (Tseng *et al.*, 2005).

SPMs can be roughly categorised into scanning tunnelling microscopes (STM) and atomic force microscopes (AFM), which obtain surface topography by sensing the tunnelling current or atomic force, respectively. The resolution of SPMs is not limited by diffraction. The atomic scale resolution can partially be attributed to high-precision piezoelectric transducers (PZT) which execute motions with atomic level or even higher precision and accuracy in response to electronic commands (Wickramasinghe, 1990).

The first SPM was an STM, which brought a Nobel Prize in physics to the developers (Binnig & Rohrer, 1983). STM scans a metallic tip towards the surface under test, which is electrically conducting or semi-conducting until a tunnelling current between the tip and test surface is sensed owing to the voltage applied, as illustrated in Figure 2.2 (Anselmetti *et al.*, 2012; Schneir *et al.*, 1989). There should be only one atom at the end of the tip interacting with the test surface in order to achieve atomic resolution (Chen, 1993). The tunnelling current can only be detected when the distance between the probe tip and the surface is less than 1 nm. When the probe gets closer to the test surface, the tunnelling current surges. A shift of 0.1 nm varies the current by a factor of ten,

which provides STM with high measurement sensitivity at the atomic level (Van Loenen *et al.*, 1990). The stylus usually scans several angstroms over the surface with PZTs. The application of STMs is limited by the necessity for electrically conducting test surfaces.

STMs work in either constant-current or constant-height mode. Constant-current mode adopts a feedback loop to adjust the relative distance between the probe tip and the specimen to keep the tunnelling current constant during the scanning while constant-height mode records and analyses the tunnelling current by keeping the tip (or the specimen) at a constant height. Constant-current mode is more frequently applied as a result of larger measurable height variations. Although constant-height mode works faster, the tip can easily run into the specimen surface when the surface is coarse, causing damage to either the tip or the specimen (Chen, 1993).

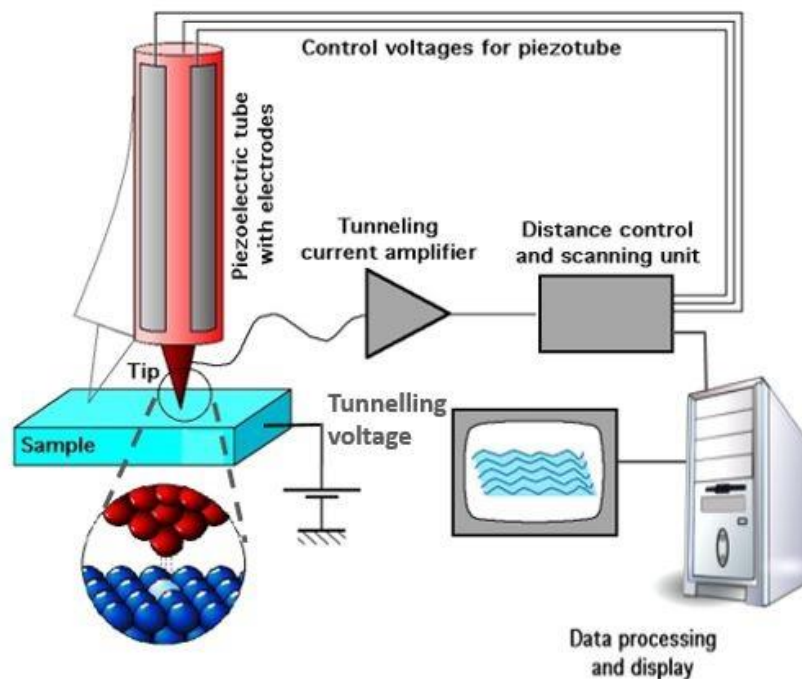


Figure 2.2 Schematic of scanning tunnelling microscope.

The atomic force microscope (AFM) is an extension of the STM for overcoming the inspection of nonconductive surfaces by making use of the force between the tip-surface interaction as the control parameter (Binnig *et al.*, 1986), as shown in Figure 2.3. There are two choices of atomic forces for AFMs, i.e., repulsive force or attractive force (Ng & Thirunavukkarasu, 2007).

In a way similar to a phonograph needle, the probe tip moves across in contact with the surface in repulsive force mode. The probe tip is attached to a cantilever at the free end, which is typically made of flexible materials such as silicon nitride. The cantilever is so flexible that it can be bent by the forces between the tip and the specimen surface during the scanning. The phenomenon is called cantilever deflection. Surface topography can be determined by measuring the deflection of the cantilever, which can be achieved in several ways (Rugar & Hansma, 1990). For example, Sarid *et al.* developed a readout technique that applies feedback into a diode laser from the reflection off the back of the cantilever made of piezoresistive material to achieve electrical measurement of the deflection (Sarid *et al.*, 1988). Alexander *et al.* presented another readout system by measuring the deflection of a laser beam reflected from a mirror attached to the cantilever based on optical triangulation technique (Alexander *et al.*, 1989).

In attractive force AFM, which is also called non-contact mode, nothing actually ever touches the surface so would not cause any damage to the specimen surface. As the attractive force is very low, and the probe tip is oscillating at a high frequency, only the variation of the phase and amplitude of the oscillation caused by gains or losses in kinetic energy during tip-specimen interaction is detected.

Apart from surface topography, AFM can also characterise a wide range of other properties of the specimen by applying variable signals and motions to the probe, such as material composition, adhesion, viscoelasticity, electric and magnetic material properties, etc. AFM is not restricted by the necessity of electrically conducting surfaces. Therefore, it finds widespread application in numerous sectors, for example, in medical and biological science. (Wilson *et al.*, 2002; Braga and Ricci, 2004)

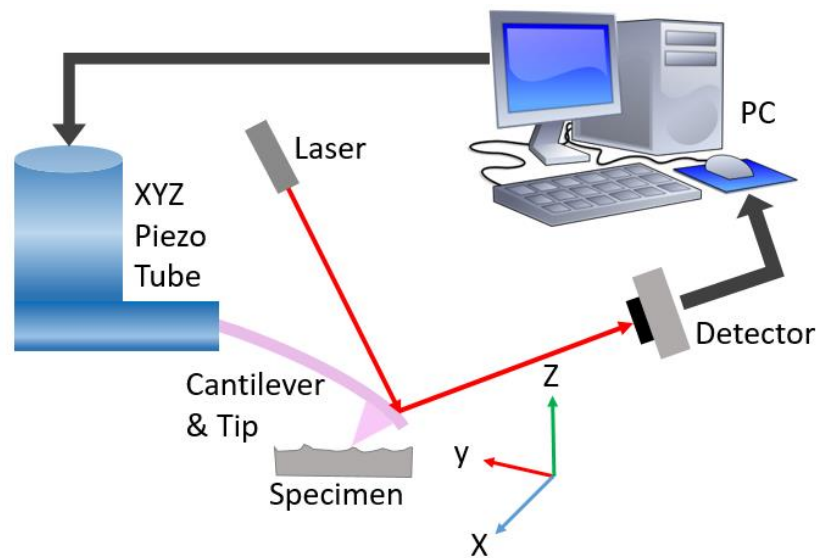


Figure 2.3 Schematic of an atomic force microscope.

### 2.3.3 Non-contact methods

Non-contact optical methods have many advantages compared to contact methods in surface texture measurement, especially in online/in-process measurement, as the data acquisition in optical techniques is speedy. Apart from the fine vertical and lateral resolution, optical methods are also non-destructive. Optical methods can be classified into non-interferometric and interferometric techniques. Some of the representative optical techniques are discussed in detail in the following sections, mainly focusing on non-interferometric techniques. Interferometric techniques will be discussed in the next chapter.

#### Optical scatterometry

As one of the area-blending metrological approaches with the most widespread applications, optical scatterometry senses a region of the specimen surface and characterises the surface texture of the region as a whole. Optical scatterometry has been adopted since the early 1960s (Bennett and Porteus, 1961). It finds wide application both in scientific research and in industrial sectors such as ultra-precision manufacturing industries, semiconductor industries, and so forth. Optical scatterometry provides very high precision from a few nanometres up to subnanometre level (Gawhary *et al.*, 2011; Logofatu *et al.*, 2004).

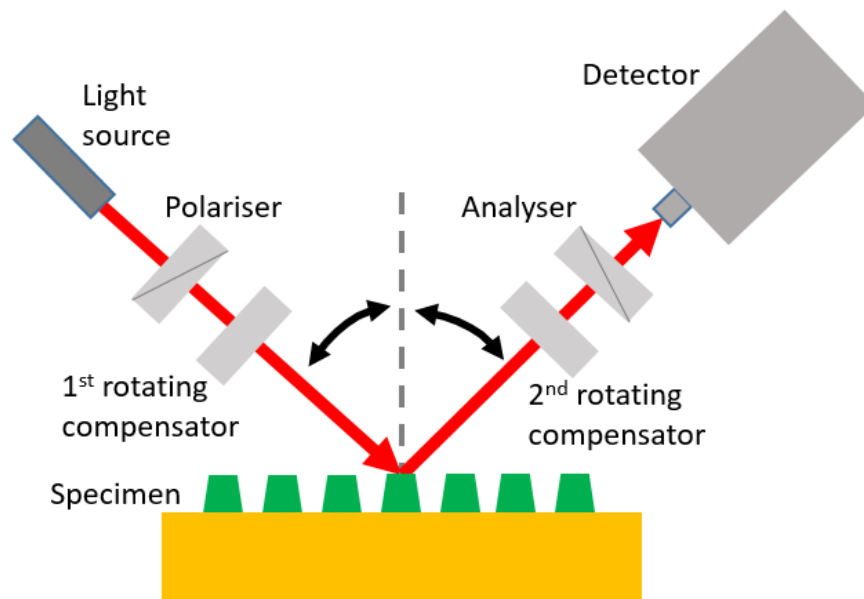


Figure 2.4 The principle of optical scatterometry.

As illustrated in Figure 2.4, the illumination light beam emanating from the light source propagates to the specimen, which scatters the light, before the scattered light is collected by the detector. The captured signal is then analysed to acquire the information about the surface texture. When a light beam hits on a smooth surface, the majority of the reflected light beam travels in the specular direction for which the reflection angle equals the incident angle. With the specimen surface getting rougher, the light beam is deflected in different directions and the specular reflection beam becomes weaker. By measuring and analysing alterations in the intensity of the reflected light beam, optical scatterometry achieves non-destructive characterisation of periodic features (Bennett & Mattsson, 1989; Stover, 1995), as well as surface roughness (Vorburger *et al.*, 1993).

Optical scatterometry has many advantages. For example, the measurement speed is high and the apparatus is relatively simple. The advantages of being immune to the ambient turbulence, free from contamination, unrestricted by diffraction limits and cost-effectiveness enable this technique to be widely adopted for in-process inspection such as tool condition monitoring and defect recognition. Persson developed an optical scatterometry-based instrument using a laser source for assessing the surface roughness in a grinding process (Persson, 1998). Gawhary *et al.* accomplished a theoretical analysis on optical scatterometry with a spatially coherent illuminating source (Gawhary *et al.*, 2011), which proved to be able to improve the accuracy in reconstructing the grating's profile compared to the incoherent source. However, optical scatterometry also has some shortcomings. For example, it cannot perform real-time measurements of the test surface.

Besides, optical scatterometry is not very suitable for measurement of individual features or non-periodic structures, as its primary goal is to achieve the measurement of gratings.

### **Focus variation**

Focus variation is an optical approach that achieves the acquisition of surface topography via axial scanning with small depths of field (DOF). A focus variation instrument generally comprises an illumination source, an optical sensor for addressing the focus, an optical system with small DOF and a high-precision mechanical translation unit for searching the focus.

Focus variation measures depth by searching for the best focus position of an optical system with a small DOF to the specimen under investigation (Scherer *et al.*, 2007). The focus position of the optical system with regard to a specimen is directly related to the topography of the specimen surface. The topography acquisition of the specimen is achieved by repeatedly searching for the optimal focus position for each and every lateral position within the region of interest (Hiersemenzel *et al.*, 2012; Danzl *et al.*, 2009; Danzl *et al.*, 2011). As illustrated in Figure 2.5, white light emanating from the illumination device propagates through the beam splitter and the objective lens to the specimen. The reflected light travels in various directions following the variations of the surface topography and the reflectivity of the specimen. After that, the reflected light is partially collected by the objective and captured by an optical sensor, which is typically a charge-coupled device (CCD) or CMOS camera after passing through the beam splitter and an imaging lens. The light is focused to different extents on the optical sensor dependent on the axial position of the specimen with regard to the objective. By translating the specimen in one direction along the optical axis of the objective, the focusing level varies from low to high and back to low, resulting in a contrast alteration of the images obtained by the optical sensor. The focus position of the specimen can be resolved correspondingly by analysing the contrast variation curve on the sensor. By repeating this process for all of the pixels on the optical sensor, the topography of the specimen in the field of view (FOV) can be obtained (Helmlí, 2011).

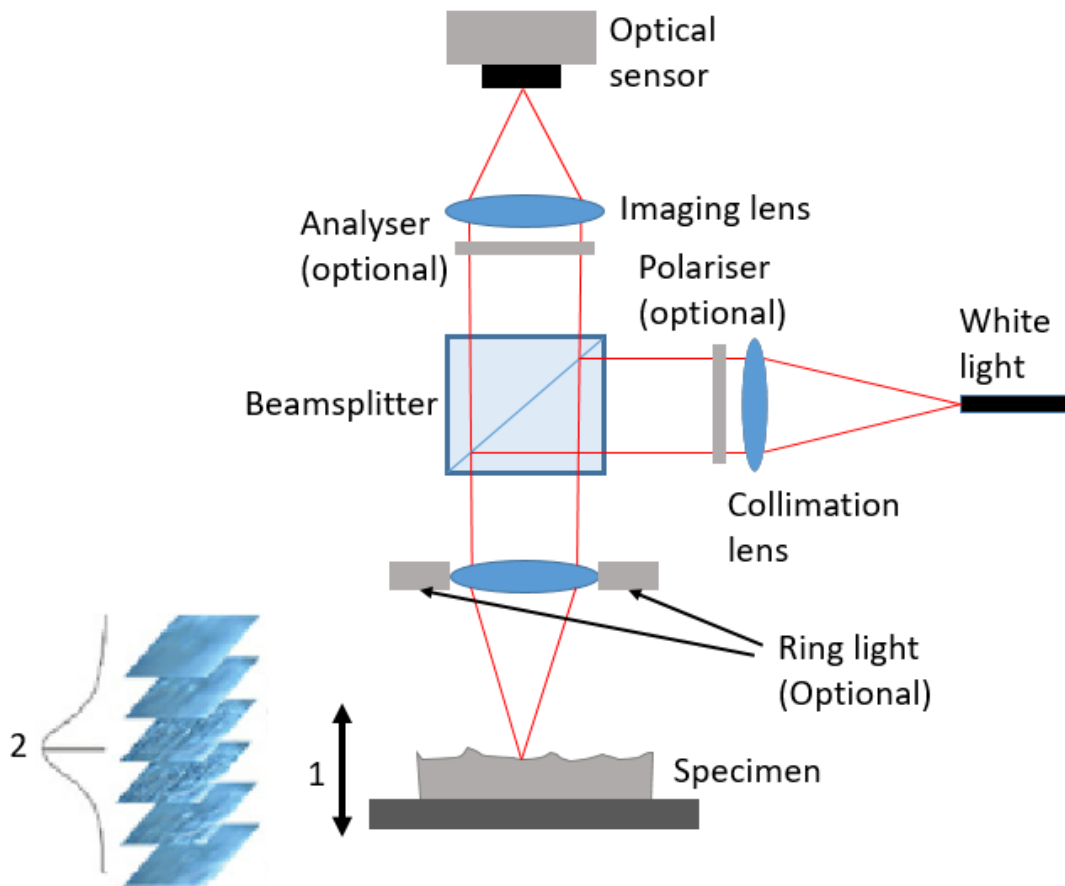


Figure 2.5 Schematic diagram of a focus variation instrument: (1) vertical movement with driving unit, (2) contrast curve calculated from the focal window.

A small region surrounding the concerned pixel needs to be considered in order to evaluate the contrast in the images captured by the optical sensor. Several approaches for assessing the contrast in the image have been developed. The focus can then be resolved by calculating the standard deviation of the grey values of the small region. When the focus level is low, i.e., the specimen surface is far away from the focal plane, identical grey values are obtained and the standard deviation is relatively low. Otherwise, for a highly focused area, the variation rate of the grey values is much higher and the standard deviation yields a higher value.

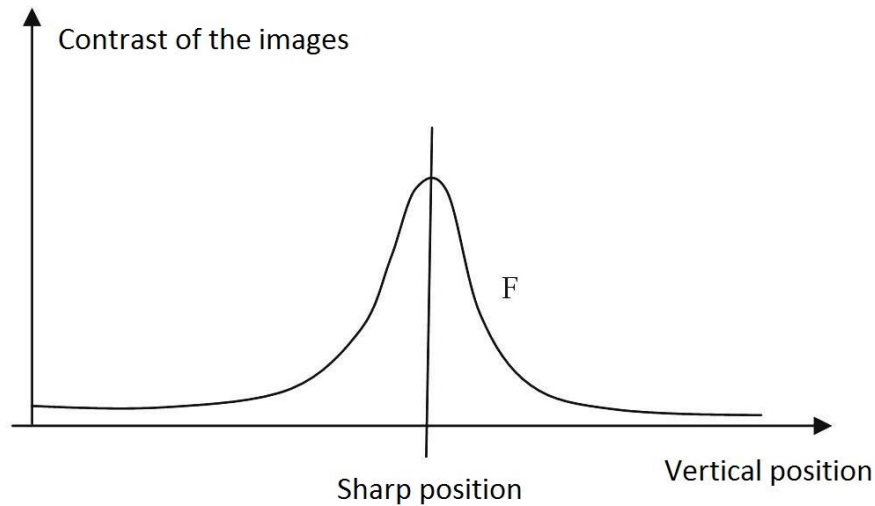


Figure 2.6 The variation of the focus level with regard to the vertical position.

The subsequent step is to calculate the focus curve and then to determine the peak. By calculating the focus at every pixel in the pile of images obtained during the vertical scanning process, the focus curve is achieved, with the peak corresponding to the maximally focused position, which is similar to the one illustrated in Figure 2.6. The position of the peak can be determined with one of the following methods, i.e., maximum point, polynomial curve fitting, and point spread function (PSF) curve fitting. The intuitive maximum point method offers the highest speed associated with the lowest accuracy among the three methods. The polynomial curve fitting method utilises a least square technique to fit a polynomial curve according to the scanned points around the maximum focus point. The advantage of this method is that the position of the focal point is resolved with a much higher resolution of the depth values compared to the scanning interval between the image planes. The point spread function (PSF) curve fitting method fits the PSF with the measured focus values and calculates the maximum to determine the depth value. Although it is the slowest method, it features the highest accuracy. After the maximum detection for all lateral points within the optical sensor FOV, a depth map is achieved.

A post-processing procedure is required after determining the depth map because of non-ideal focus and other optical distortions, usually involving several steps. One significant step is to delete the non-ideal depth values based on some criteria, such as the quality of the fitted curve and the colour information. There will be holes after the deletion of the outliers. In order to remove the holes, a filling algorithm needs to be applied based on the height information of the nearest valid points. In general, a spline or non-uniform rational basis spline (NURBS) interpolation is

employed based on the points on the border polygon around the holes. However, these interpolation steps should be avoided if the resultant dataset is utilised for surface texture calculation as they would affect the calculated results of the parameters.

The focus can be varied very flexibly with regard to the illuminating source, which helps to overcome many restrictions. Compared to other optical techniques adopting coaxial illumination, the focus variation has larger measurable range for the slope angle, owing to the employment of objectives with large NA, which yield a small depth of focus. Apart from that, the maximal measurable slope angle for focus variation successfully avoids the restriction posed by the NA of the objective because of the novel illuminating schemes. For example, various types of illumination sources such as ring light, diffuse illumination or point light source can be utilised, which makes the measurement of specimens with slope angles above  $80^\circ$  possible. Focus variation alters the degree of focus by translating the specimen relative to the objective using a scanning unit, such as a piezoelectric drive, direct drive, or spindle drive. Piezoelectric drives have very high resolution but relatively small scanning ranges. Direct drives scan quickly but are not very suitable for vertical scanning. Spindle drives feature high resolution, large scanning range, and the ability to drive high loads. As a consequence, they find widespread applications in focus variation.

Focus variation is widely applied in optical surface measurement, achieving simultaneous measurement of both form and roughness. Submicrometre lateral resolution and nanometre scale vertical resolution can be attained also with the ability to measure steep flanks. However, it is restricted by the necessity for vertical mechanical scanning and cannot be used for in-line inspection (Hiersemenzel *et al.*, 2012).

### **Confocal Microscopy**

Owing to the low quality of the imaging achieved by conventional light microscopy, Minsky proposed the modifications by filtering the stray light with confocal apertures to improve the image quality in 1961 (Minsky, 1961). However, confocal microscopes were not utilised for obtaining non-invasive 3D information of the specimens until the mid-1980s when the development of computer science brought sufficient computing power. After that, confocal microscopes became increasingly important and found widespread applications in many sectors, such as cell biology, physiology, microsystems, material applications, etc. (Semwogerere & Weeks, 2005; Petroll *et al.*, 1993).

As illustrated in Figure 2.7, confocal microscopy employs two conjugate apertures to eliminate out-of-focus and stray light, ensuring that only light reflected at the focal point on the inspected surface is able to reach the detector, which improves the quality of the images. In general, two small pinholes are utilised and located in planes conjugate to the focal plane of the objective, one in front of the illumination source and the other in front of the photodetector. However, in some systems where a spatially coherent light source is adopted, it is unnecessary to place a pinhole in front of the illumination source. 2D intensity images can be acquired with pixel-by-pixel scanning of the illuminating and detecting pinholes in lateral directions, whereas 3D irradiance images have to be obtained by scanning vertically so that each and every point on the sample surface within the field of view (FOV) passes through the focal plane of the objective.

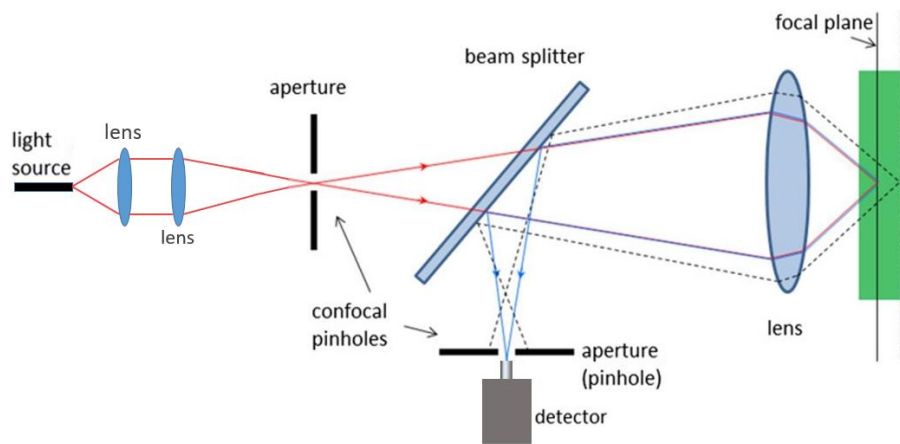


Figure 2.7 Schematic of confocal microscope.

When the sample surface is positioned accurately on the objective's focal plane, the light is reflected onto the confocal pinhole. Therefore, the signal acquired by the photodetector is strong. In contrast, when the sample surface is away from the objective's focal plane, the light is reflected away from the pinhole, which filters out the out-of-focus light, resulting in a relatively weak signal recorded by the photodetector. The recorded signal for each point on the sample during the vertical scanning is analysed to search for the position with maximal intensity where the imaged point is in focus. The intensity signal for a certain point on the sample, namely the axial point spread function (PSF) declines with the distance to the focal plane getting larger. The in-focus position, namely the location of the peak of the axial PSF can be more consistently determined with the fitting algorithms rather than the simplest low-resolution method of directly assigning the discrete position of the peak to achieve higher resolution. The fitting algorithms can be divided into

real-time and off-line fitting algorithms. Real-time algorithms process the images for each step of the axial scanning and then simply discard the images, with the advantage of very low requirement for memory, but cannot deal with multiple peaks. In contrast, off-line algorithms save the whole set of confocal images to memory and then determines the 3D topography of the surface. Off-line algorithms are capable of handling multiple peaks, with the expense of memory and time for computing. The width of the axial PSF, which is dependent on the objective NA and the wavelength of the illumination source, has significant impact on the vertical resolution. The vertical resolution can be improved by narrowing the axial signal, via different means, such as by increasing the objective NA or by applying annular filters (Conchello *et al.*, 1994).

Several efforts have been put into speeding up the data acquisition process in confocal microscopy, primarily by applying variations on the confocal aperture, such as Nipkow disks, microlenses, or scanning slits (Inoué, 2006). Another way of increasing the measurement speed is by applying simultaneous projection of an evenly spaced multiple slit or grid pattern.

## **2.4 Comparison of various types of instruments**

As a result of their different functioning mechanisms, each type of the instrument discussed has its own advantages and disadvantages. For example, stylus profilometers are suitable for measuring large-scale specimens made of hard materials, interferometers are more suited for specular and reflective surfaces, and focus variation microscopes perform better in inspecting relatively rough surfaces. Stylus-based instruments are potentially destructive while optical techniques would never damage the measurand in this respect. In general, contact methods are more time-consuming than non-contact methods (Conroy & Armstrong, 2005).

Different types of instruments typically feature different measurable dimensions and resolutions, as illustrated in Figure 2.8. It shows that the stylus-based instruments are most suitable for large-scale measurements. Optical techniques feature smaller measurable ranges but relatively higher resolution while the AFM family of instruments have the highest resolution with the expense of measurement range.

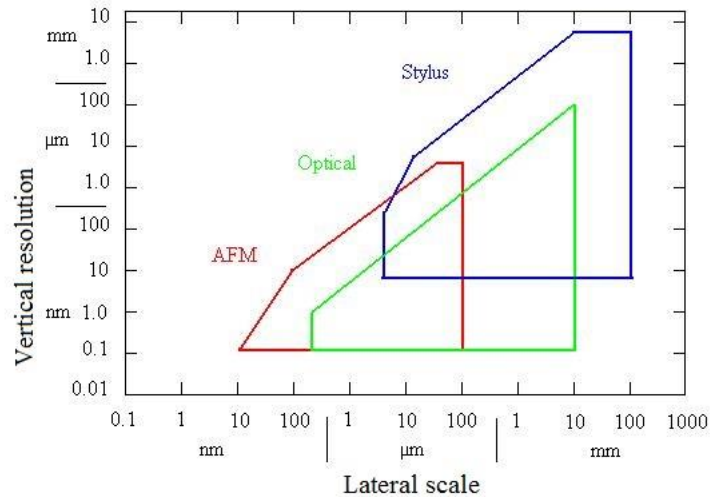


Figure 2.8 Measurement scale and resolution for 3 different types of instruments, AFM, optical and stylus (adapted from Jiang *et al.*, 2007b).

## 2.5 Summary

This chapter has presented some general knowledge about the discipline of surface metrology and the importance and applications in manufacturing industries. The development process was briefly reviewed, including the evolution of the filtration techniques, as well as the characterisation parameters. Some basic definitions and terminologies such as roughness, waviness, and form were also discussed. Further in the chapter, some modern instrumentation techniques were reviewed and compared, including some representative techniques for both contact method and non-interferometric optical methods, such as stylus profilometer, SPM, focus variation, confocal microscopy, and so forth. All these technologies are restricted in measuring the high-sloped structures. The next chapter will focus on reviewing the interferometric techniques in detail, such as phase-shifting interferometry (PSI), coherence scanning interferometry (CSI), wavelength scanning interferometry (WSI), etc.

### 3 Optical interferometry

#### 3.1 Introduction

Optical interferometry has found broad applications in surface metrology. This technique is based on the interference phenomenon, which is an important evidence of the wave nature of light (Hecht, 2016). This chapter begins by discussing the basics of light interference and the coherence properties of light, then several types of mainstream interferometric techniques are reviewed in detail, such as phase shift interferometry (PSI), white light interferometry (WLI), wavelength scanning interferometry (WSI), etc.

#### 3.2 Light interference and coherence

Light interference refers to a physical phenomenon when two or more light beams superimpose, leading to an irradiance distribution, which is not uniform in space as in Eq. (3.1).

$$I(x, y) = I_1(x, y) + I_2(x, y) + 2\sqrt{I_1(x, y)I_2(x, y)}\cos\Delta\varphi. \quad (3.1)$$

where  $I(x, y)$  represents the intensity distribution of the interference pattern,  $I_1(x, y)$  and  $I_2(x, y)$  denote the intensity distributions of the first and second light beams, respectively,  $\Delta\varphi$  refers to the phase difference between the two light beams, and  $x, y$  stand for the spatial coordinates. The interference is constructive if the superimposition strengthens the intensity. In contrast, destructive interference occurs when the superimposition lowers the intensity (Hariharan, 2010). The fringe visibility can be expressed as  $v = \frac{I_{max} - I_{min}}{I_{max} + I_{min}} = \frac{2\sqrt{I_1 I_2}}{I_1 + I_2}$ . Therefore, it is better to keep the intensities of the two beams balanced in order that high visibility can be achieved. The fringe visibility is also reliant on the coherence characteristics of the light beams, both temporal coherence and spatial coherence (Hariharan, 1991).

Temporal coherence is a metric of the monochromaticity of an illumination source. It characterises the coherence of a signal with itself shifted by a time interval. Temporal coherence can be assessed by coherence time or coherence length. Coherence time refers to the critical time shift when the correlation between the signal and the shifted signal declines to a certain low level. Coherence length refers to the distance the signal propagates during a period equal to coherence time

(Yoshizawa, 2015). Coherence length is inversely relevant to the bandwidth of the illumination light and can be calculated as Eq. (3.2).

$$L_c = \frac{\lambda^2}{\Delta\lambda}. \quad (3.2)$$

where  $\Delta\lambda$  denotes the linewidth and  $\lambda$  represents the central wavelength of the illumination beam. It can be seen clearly that a narrower spectral linewidth provides a longer coherence length and vice versa.

Spatial coherence allows by assessing the cross-correlation between two points located within a certain area on a wavefront. If the phase difference remains zero all the time with the propagation of the wavefront, the beam has impeccable spatial coherence. If the cross-correlation is limited, the beam is partially coherent (Hariharan, 2010).

### 3.3 Phase-shifting interferometry

Phase-shifting interferometry (PSI) was prototyped in the 1960s and remains a very important technology for surface metrology, especially in the field of high-precision polished and smooth surfaces (Creath, 1988). Phase-shifting techniques were initially applied for optical measurement in monochromatic interferometers, such as Fizeau and Twyman-Green interferometers (De Groot, 1995; Deck, 1996). A measurement resolution up to 1/1000 of peak-valley value has been presented under optimised conditions (Kemao *et al.*, 2000). Apart from that, the measurement is speedy and insensitive to the illumination variance. The majority of PSI instruments are equipped with highly coherent illumination sources, such as lasers. Only very few employ relatively incoherent sources. Nowadays, light-emitting diodes (LED) are widely adopted, irrespective of monochromatic LEDs or white-light LEDs, associated with narrow-bandwidth spectral filters, especially for bespoke PSI applications (Malacara, 2007; Leach, 2011).

PSI is a scheme depicting the routine of data acquisition and analysis that can be applied in a wide variety of inspecting applications. It is a well-defined technology for 3D surface characterisation that is reliant on digitisation of interference fringes captured during a series of controlled phase shifts, typically generated by precisely-controlled mechanical motions of the reference mirror, which is attached to a piezoelectric transducer (PZT), as shown in Figure 3.1. A frame of an interferogram is captured using a camera for each phase shift; thus, a certain number of

interferograms are attained. After that, a PSI algorithm is adopted to process the interferograms to resolve the original phase and then the surface height information, typically with the measurement repeatability below 1 nm, irrespective of the FOV. The interference microscopes based on PSI employ a wide range of interference objectives to achieve the measurement of form and roughness, such as objectives of the Michelson, Mirau, or Linnik setups featuring different magnifications (Hariharan *et al.*, 1997).

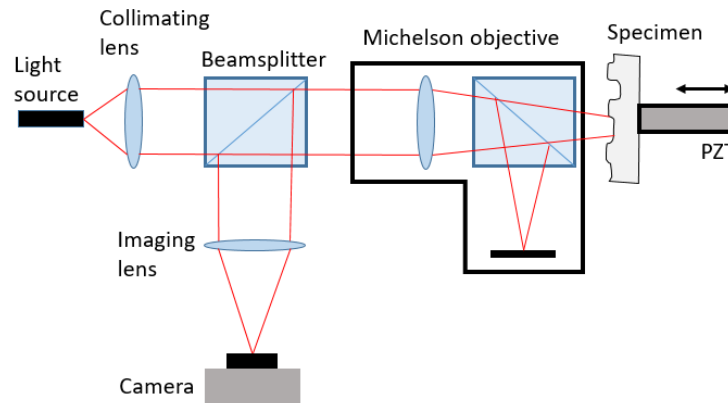


Figure 3.1 Schematic of a phase-shifting interferometer.

Apart from mechanical scanning, other approaches are also adopted to realise the phase shifting, such as an electro-optic or acousto-optic modulator, rotating a half-wave plate, tilting a glass plate and etc. The phase should be linearly shifted, irrespective of how the phase shifting is achieved. The interference pattern can be represented as follows:

$$I = I_0(1 + v \cos \varphi) . \quad (3.3)$$

where  $I_0$  refers to the DC intensity bias,  $v$  represents the visibility, and  $\varphi$  signifies the initial phase.

After the n-step phase shifts, the following mathematical equations must be satisfied:

$$\begin{pmatrix} I_1 \\ I_2 \\ I_3 \\ \vdots \\ I_n \end{pmatrix} = \begin{pmatrix} I_0(1+v\cos(\varphi(x,y)+\alpha_1)) \\ I_0(1+v\cos(\varphi(x,y)+\alpha_2)) \\ I_0(1+v\cos(\varphi(x,y)+\alpha_3)) \\ \vdots \\ I_0(1+v\cos(\varphi(x,y)+\alpha_n)) \end{pmatrix}. \quad (3.4)$$

where  $\alpha_1, \alpha_2, \dots, \alpha_n$  represent the phase shifts induced. There are numerous phase extraction algorithms, such as the three-step algorithm, five-step algorithm, Carré algorithm, and so forth (Malacara & Servin, 2016). Some algorithms require a certain number of phase shifts and some algorithms do not. For example, the three-step algorithm performs a phase shift of  $90^\circ$  each time but the Carré algorithm is independent of the amount of the phase shifts.

PSI suffers from the renowned  $2\pi$  phase ambiguity issue, which significantly restricts its field of applications (Malacara, 2007). Various phase unwrapping algorithms are designed to correct the  $2\pi$  phase ambiguity caused by noise or trigonometric functions (Huntley, 1989). However, the difficulty arises when there is a large OPD jump over  $\frac{\lambda}{2}$ . There are no effective means of resolving the phase ambiguity, which constrains the applications of PSI to only relatively smooth surfaces. To sum up, PSI offers high repeatability, precision, and accuracy, but is limited to only smooth surfaces within the  $2\pi$  phase limit (Malacara, 2007).

### 3.4 White light interferometry

White light interferometry (WLI), also known as vertical scanning interferometry (VSI) or coherence scanning interferometry (CSI), is a widespread and leading non-contact optical profilometry for the inspection of engineering surfaces such as machined surfaces, MEMS devices, and binary optics etc. With the development of electronics, computer science and software technologies, many powerful instruments based on WLI have been developed (Bowe & Toal, 1999; Wyant, 2002).

As shown in Figure 3.2, a WLI instrument typically encompasses an illuminating source, an interference objective, a signal detector and a mechanical scanner. The illuminating source for WLI is typically incoherent with a wide spectral band (normally white light). Incandescent lamps, such as a tungsten halogen bulb, are commonly employed. However, nowadays, the most widely

applied illuminating source is white-light LED (Yoshizawa, 2015). As both the spatial coherence and temporal coherence of the broadband illumination source are extremely low, the reference arm and measurement arm have to be exactly matched in order to achieve interference fringes. The interference objective must be compatible with the low coherence illumination, with the two arms balanced for the dispersion owing to different indices of refraction corresponding to the whole range of wavelengths. The best focus position should be coincident with the point with zero OPD. Non-planar reference mirrors can be utilised in order to match the specimen surface shape in the applications inspecting specimens with special shapes such as spherical or parabolic surfaces (Biegen, 1990). The scanner achieves mechanical scanning usually by precisely translating the interference objective, in some other circumstances by moving the specimen under test using a high-precision PZT, sometimes even by translating the reference mirror, beam-splitter or a combination of the optical components within the case of the objective instead of translating the interference objective as a whole. The scanning is normally along the optical axis of the interference objective perpendicular to the specimen surface. The scanning range is typically between 10  $\mu\text{m}$  and 200  $\mu\text{m}$  for scanners based on PZT, and several millimetres for motorised scanners (de Lega *et al.*, 2004).

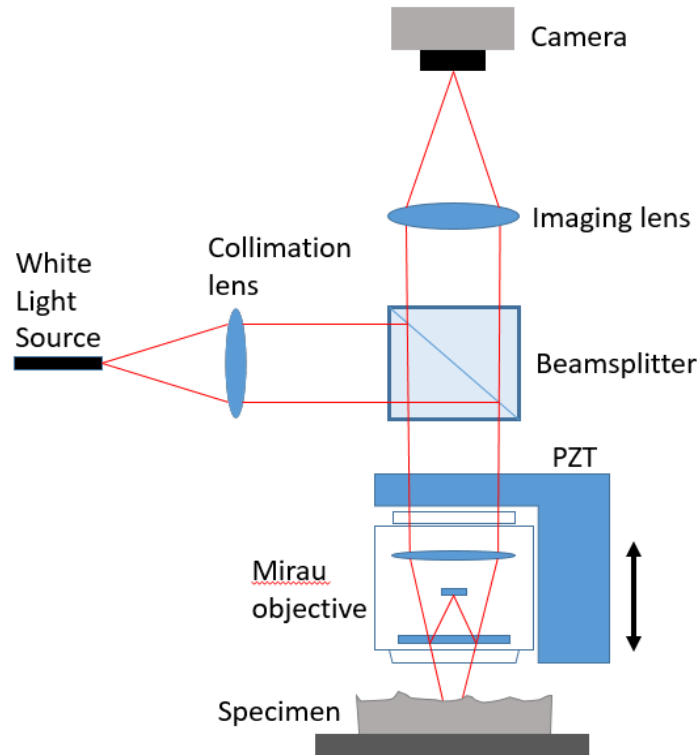


Figure 3.2 Schematic of a white light interferometer based on a Mirau objective.

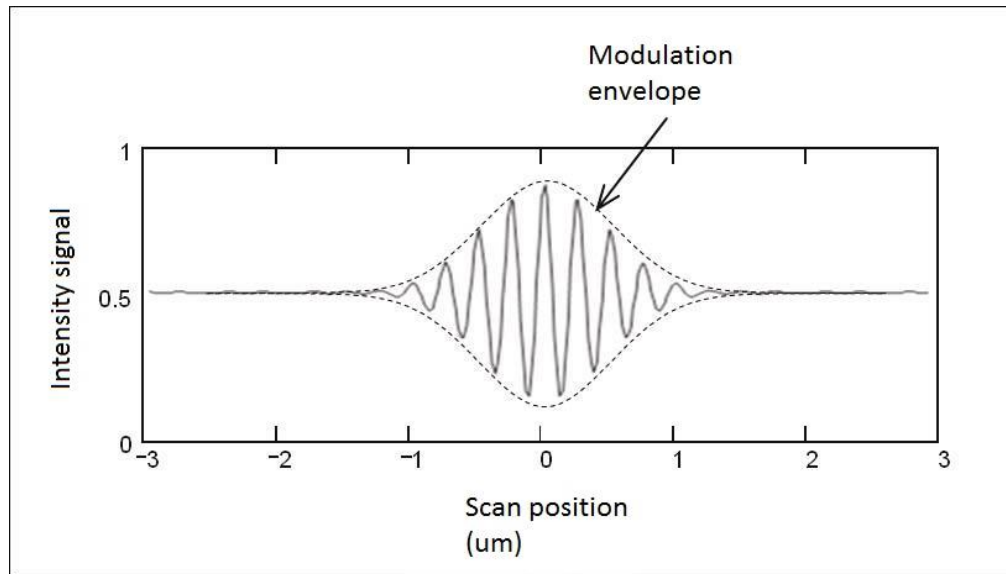


Figure 3.3 Interference signal of WLI.

Compared to monochromatic PSI, the fringe visibility of WLI is relatively low, as WLI employs a broadband illumination source covering a wide range of visible wavelengths. As demonstrated in Figure 3.3, the fringe visibility peaks when the length of the measurement arm equals the reference arm, i.e., the optical path difference (OPD) is zero. When the OPD increases, the visibility declines rapidly (Malacara, 2007). The topography of the specimen surface is resolved through the exhaustive investigation of the fringes at every spatial point of the captured frames during the vertical scanning. The basic measurement principle is to search the scanning positions for the peak of the signal intensity or fringe visibility, then sectioning the surface images in accordance with the distance with respect to the reference mirror. There are many algorithms to achieve this aim. For example, the envelope detection method usually utilises a sequence of digital filters associated with the digital signal processing (DSP) techniques based on communication theory (Larkin, 1996; Harasaki *et al.*, 2001) or other approaches to recover the baseband signal exhibiting only the envelope (Haneishi 1984). However, it is vulnerable to the error sources such as diffraction, optical aberrations, environmental vibration, etc. The vertical resolution can only achieve nanometre scale. An improved approach that demonstrates better noise immunity is to estimate the overall signal position with the centroid of the square of the derivative of the intensity signal (Ai and Novak, 1997). State-of-the-art WLI microscopes apply a reinforced analysis method that combines envelope position and the interference phase estimation algorithm featuring much higher precision to improve the accuracy (Malacara, 2007). For the reinforced analysis method, the envelope position only aims to determine the fringe order while the phase estimation algorithm

resolves the fractional part (de Groot, 2002; Sandoz *et al.*, 1997; Harasaki *et al.*, 2000). The reinforced analysing method can achieve subnanometre vertical resolution.

WLI has no height ambiguities, which commonly exist in PSI in surface measurement. Therefore, WLI can be employed for inspecting rough surfaces and structured surfaces with large discontinuities. In practice, WLI is a mature technology widely adopted in commercial instruments.

WLI instruments achieve data acquisition over time, which means that the time-related features, such as mechanical vibrations, temperature drifts and air turbulence are convolved into the measurement results. Therefore, the environmental conditions can be an important contributor to the measurement uncertainty. Environmental compensation or insulation is essential for achieving highly repeatable, high-precision measurement.

### 3.5 Dual-wavelength and multi-wavelength interferometry

It is difficult for interferometers employing monochromatic illumination to realise accurate measurement for the specimens with high-sloped or rough surfaces, as the axial measurable range is restricted by the  $2\pi$  phase ambiguity issue. Although some phase unwrapping algorithms have already been developed, when the optical path difference (OPD) between two adjacent pixels varies by more than half a wavelength, these algorithms would not be able to resolve the ambiguity because the phase variation is larger than  $2\pi$ , which significantly limits the field of applications.

A direct and simple solution to this issue is to lengthen the illumination wavelength to enlarge the measurement range because the bottleneck is the wavelength of the illuminating source. Therefore, a light beam with a much longer synthetic wavelength was constructed by combining two illumination sources with wavelengths,  $\lambda_a$  and  $\lambda_b$ , respectively. The synthetic wavelength can be

calculated as  $\lambda_{syn} = \frac{\lambda_a \lambda_b}{|\lambda_a - \lambda_b|}$ . In this way, the axial measurable range can be effectively enlarged if

the two wavelengths are prudently selected (Cheng & Wyant, 1984; Creath, 1987). The measurement is conducted by first capturing interferograms at one wavelength while altering the phase appropriately and the modulo  $2\pi$  phase is calculated. The same process is then applied to the other illumination wavelength. A modulo  $2\pi$  phase corresponding to a longer effective wavelength, which is the beat between the two illuminating wavelengths, can be synthesised by combining the results of the two modulo  $2\pi$  phase measurements. The surface topography can be

attained by analysing the envelope signal. The range of measurable heights is significantly expanded in this way. Multi-wavelength interferometry works in a similar way but the illumination scheme encompasses even more wavelengths (Kumar *et al.*, 2008). It is worth mentioning that dual- or multiple-wavelength interferometry does not completely solve the  $2\pi$  phase ambiguity problem but only enlarges the measurement range without ambiguity.

The original dual- or multiple-wavelength interferometry takes at least twice the measurement time as single-wavelength PSI when carrying out a measurement. There are some attempts to speed up the measurement process. One attempt is to capture the two- or multiple-wavelength superimposed interferograms in one frame and then analyse it with the Fourier transform method (Onodera & Ishii, 1997). Pförtner and Schwider presented an RGB interferometer adopting a multichromatic camera to capture interferograms for illumination wavelengths of three laser sources that corresponded to the RGB components of the camera in one snapshot (Pförtner and Schwider, 2003).

The shortcoming of this method mainly originates from the  $2\pi$  phase ambiguity problem when the OPD is larger than a half of the effective wavelength. Meanwhile, the resolution is inversely proportional to the effective wavelength. Therefore, there is a trade-off between the measurable range and the resolution. The application of dual- or multiple-wavelength interferometry in interference microscopy is also restricted by the depth of field (DOF) of the interference objective, which also affects the measurable height range apart from the effective wavelength.

### **3.6 Wavelength scanning interferometry**

Wavelength scanning interferometry (WSI) is widely applied in measuring absolute distances ranging from nanometres to metres via wavelength scanning rather than mechanical scanning by employing a wavelength-tunable illumination scheme (Kang *et al.*, 2001; Thiel *et al.*, 1995; Walsh, 1987). The system does not require axial mechanical scanning. Instead, interferograms featuring different illumination wavelengths are captured while tuning the light source and the fringe contrast is usually higher than WLI (Malacara, 2007). By analysing a sequence of interferograms, the height distribution of the specimen under test with respect to the reference mirror is achieved. WSI successfully gets rid of the renowned  $2\pi$  phase ambiguity problem (Kuwamura & Yamaguchi, 1997; Yamaguchi *et al.*, 1998). A typical wavelength scanning interferometer with Michelson setup is shown in Figure 3.4.

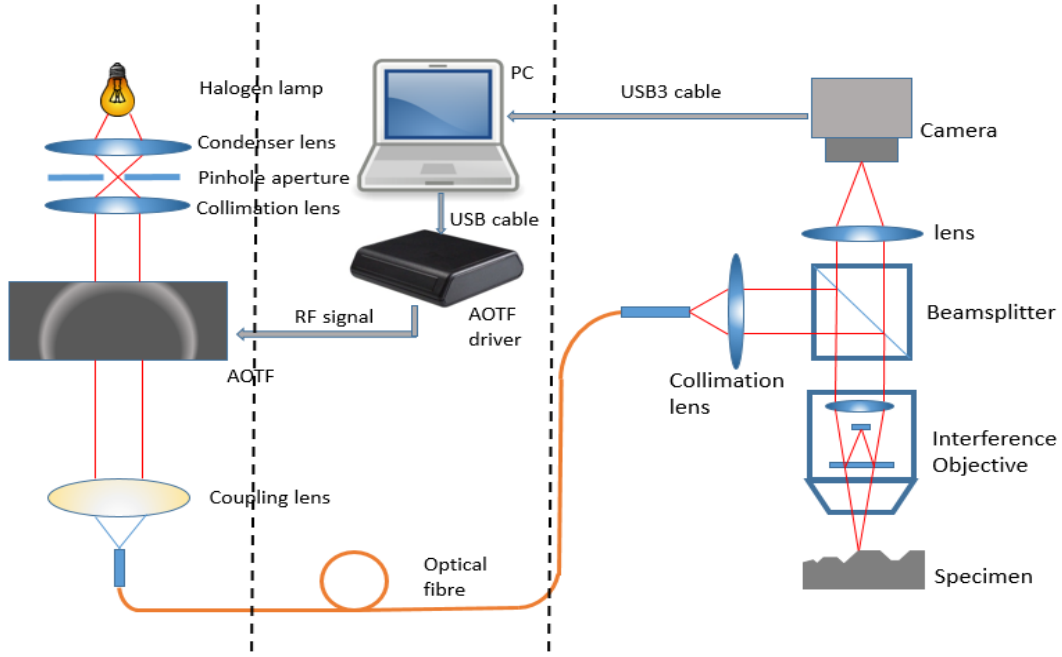


Figure 3.4 Wavelength scanning interferometer based on Michelson geometry.

The wavelength-tunable light source plays a crucial role in WSI, as the measurement resolution and axial measurable range are determined by the tuning range and tuning step of the illumination. At first, expensive and bulky dye lasers were adopted (Malacara, 2007), which brought many inconveniences. Tunable solid-state lasers were also utilised (Malacara, 2007). The means of scanning the wavelength is typically by altering the injection current. However, the laser mode hopping issue was a major problem restricting the development of WSI at the early stage. An external resonator was employed to solve this problem (Führer & Walther, 2008). More recently, full-spectrum illumination sources in combination with wavelength tunable devices, such as an acousto-optical tunable filter (AOTF), were proposed as more stable and convenient illuminating systems (Jiang *et al.*, 2010). With the continuous development of the illuminating system, both the scanning range and the scanning step have been considerably improved. The intensity at each spot can be represented by the following equation:

$$I_{xy}(\lambda_i) = a_{xy}(\lambda_i) + b_{xy}(\lambda_i) \cos\left(\frac{4\pi}{\lambda_i} h_{xy}\right). \quad (3.5)$$

where  $\lambda_i$  is the tuning wavelength,  $x$  and  $y$  are the horizontal and vertical indices of the image sensor of the camera respectively,  $a_{xy}$  signifies the DC bias of the interference signal,  $b_{xy}$  refers

to the magnitude of the interference contrast variation, and  $h_{xy}$  is the OPD between corresponding points on the reference mirror and the specimen under test (Takeda & Yamamoto, 1994). As no mechanical scanning is required,  $h_{xy}$  remains invariable during the measurement. Even if the ambient elements such as environmental vibration, thermal drift, etc. are considered, there are methods available to compensate. Jiang *et al.* presented an approach that achieved the monitoring and compensation of the environmental noise using a servo controller (Jiang *et al.*, 2010). The controller was implemented with a reference interferometer illuminated by a superluminescent light-emitting diode (SLED), whose output was fed into a PI controller to neutralise the axial mechanical vibration and stabilise the whole system (Muhamedsalih *et al.*, 2013). After getting rid of the environmental instability, the frequency of the interference pattern relies on the distance from the points on the specimen to the corresponding points on the virtual reference plane. The relative distance, namely the OPD between the specimen surface and the reference mirror, can be resolved by finding the fringe frequency, namely the phase variation rate at each point. At first, the fringe frequency was determined by counting the number of zero-crossings of the intensity signal at each pixel with which only low accuracy can be achieved. Later, a method based on the Fourier transform was proposed and implemented (Takeda and Yamamoto, 1994; Yamaguchi *et al.*, 1998), which significantly improved the accuracy. After that, Moschetti *et al.* introduced the method of achieving height estimation through phase information, which was primarily used in PSI and WLI and reported improvement in the accuracy by a factor of 10 (Moschetti *et al.*, 2016a). Although some other problems, such as ghost step, existed (Ghim & Davies, 2012), researchers are still working to overcome the issues. WSI requires tens or even hundreds of interferograms during the wavelength scanning for each measurement. Unlike WLI, the measurement time for WSI remains constant for shallow and deep surfaces because the number of frames does not change.

During the measurement process, the specimen surface can be on both sides of the reference plane. A height sign ambiguity issue exists here since the fringe analysis algorithms only resolve the amplitude of the specimen's relative distance to the reference plane without any information about the direction. Moschetti *et al.* reported an approach called quadrature wavelength scanning interferometry (QWSI) to overcome this issue, combined with several mechanical movements (Moschetti *et al.*, 2016b).

Wavelength scanning is used in a number of optical methods such as optical frequency domain reflectometry, distance measurement (Kikuta *et al.*, 1986), speckle interferometry and, more

recently, digital holography as well as for thickness measurement (or its dispersion) of a transparent object (Gao *et al.*, 2012). The largest measurable angle for WSI is dependent on the NA of the objective. For example, the NA of the objective adopted in this thesis is 0.1, then the largest measurable angle for a WSI using this objective is  $5.7^\circ$ .

### 3.7 Dispersive interferometry

Dispersive interferometry, which is also known as spectrally-resolved white light interferometry (SRWLI), is an interferometric technique that attains phase modulation via wavenumber (reciprocal of wavelength) alterations instead of mechanical scanning similar to WSI (Calatroni *et al.*, 1996). Spectrally-resolved white light interferograms find many different applications, e.g. measuring the differential index of refraction, wavelength multiplexing, distance and displacement measurements, and here for profile measurement (Hlubina, 2002; Debnath *et al.*, 2006). The primary advantage of SRWLI is its ability to achieve a profile of a specimen with discontinuities up to tens of micrometres in a single-shot, namely a single frame of spectral interferogram using a spectrometer (Debnath *et al.*, 2009). The spectrometer splits a single line of the specimen's white light fringes into spectral fringes along the chromatic axis and then captures the spectrally-resolved fringes. Figure 3.5 shows a schematic setup of SRWLI.

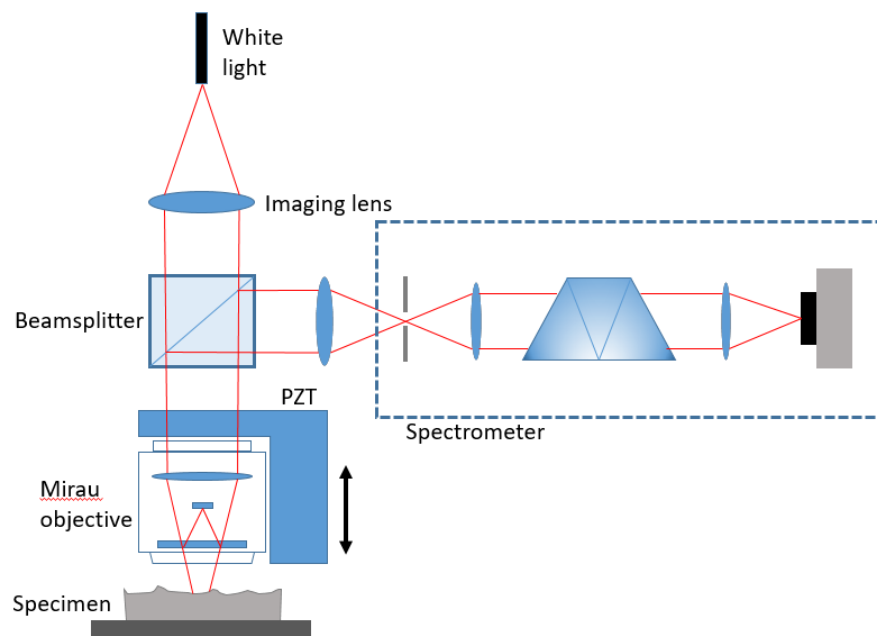


Figure 3.5 A schematic setup of spectrally-resolved white light interferometry.

The chromatic axis in SRWLI is perpendicular to the entrance slit of the spectrometer, which is parallel to one axis of the optical sensor (camera). A line of captured pixels along the chromatic axis constitutes a spectrally-resolved interference signal corresponding to a point on the measurand, from which the fringe frequency or spectral phase can be resolved for achieving the distance from the point to the corresponding point on the reference mirror. Therefore, a frame of interferogram, which is comprised of many lines, conveys a profile of the specimen under test. As a consequence, mechanical scanning of the sample stage in lateral direction is essential in order to realise areal measurement of the specimen.

The fringe analysis algorithm of SRWLI is identical to WSI. The spectral interferogram can be processed by calculating the frequency or the phase variation rate of the intensity signal with respect to the wavenumber line by line to determine the distance between the measurand and the reference plane (Schwider and Zhou, 1994). This can be realised using Fourier transform (Tang *et al.*, 2014) or a spatial phase-shifting algorithm (Sandoz *et al.*, 1996) in an identical way as WSI.

### **3.8 Summary**

This chapter has discussed the fundamentals of light interference and its coherence properties, then reviewed several representative types of interferometric techniques in detail, including phase shift interferometry (PSI), white light interferometry (WLI), wavelength scanning interferometry (WSI), etc. However, the largest measurable slope angle for optical interferometry is restricted by the NA of the objective (can be calculated as  $\frac{1}{2} \arcsin(NA)$ ), also when the NA increases, the working distance declines rapidly, which makes it difficult to inspect the structured surfaces with high-sloped facets. So this thesis proposes to build an apparatus comprising two interferometric probes to inspect V-groove structured surfaces. The next chapter will review subaperture stitching interferometry (SASI). Similar to the method proposed in this thesis, subaperture stitching interferometry is also a combination of interferometry and stitching technique.

## 4 Subaperture stitching interferometry

### 4.1 Overview

With the size of planar and convex optics getting increasingly large, the investment of money and effort in constructing inspection instruments, such as large-aperture interferometers, goes up rapidly (Murphy *et al.*, 2003). In this respect, subaperture stitching interferometry, as a combination of interferometry and stitching technique, becomes increasingly valuable. Stitching interferometry inspects large-scale components using an ordinary interferometer with a relatively small field of view (FOV), which is achieved by taking a number of overlapping subaperture measurements of the component before numerically blending these measurement results together and removing the relative piston and tip-tilt (Chen *et al.*, 2016).

### 4.2 Image stitching

Image stitching or mosaicking is a combination process involving multiple images with overlapping regions to achieve a single composite image with a larger field of view (FOV). With the development of computer science and software technology, it is increasingly important in a wide range of fields including remote sensing, medical imaging, machine vision, digital maps, satellite photos, among others (Vaghela & Naina, 2014). The image stitching process used is typically comprised of two sequential phases, namely image registration and blending.

#### 4.2.1 Image registration

Image registration adopts a pixel-based or feature-based approach to reduce the sum of absolute variances between the corresponding pixels within the overlapping regions to the lowest to complete the alignment of a collection of images (Salvi *et al.*, 2007).

##### 1) Pixel-based registration

One of the images is chosen as the reference or target, which is then kept static. The pixel-based approach achieves the alignment by warping or shifting the other images (called source images) relative to the reference image to search for the optimal alignment. Therefore, appropriate error metrics should be firstly selected to evaluate the dissimilarity (Brown, 1992). A commonly used solution based on least-square method is to search for the transformation that minimises the sum of squared differences (SSD) function as:

$$E_{SSD}(u) = \sum_i \left[ I_1(x_i + u) - I_0(x_i) \right]^2 = \sum_i e_i^2. \quad (4.1)$$

where  $u = (u, v)$  is the shift and  $e_i = I_1(x_i + u) - I_0(x_i)$  is the residual error. The error measure can be made more resistant to outliers if the place of the squared error terms is taken by a robust function  $\rho(e_i)$ :

$$E_{SRD}(u) = \sum_i \rho \left( I_1(x_i + u) - I_0(x_i) \right) = \sum_i \rho(e_i). \quad (4.2)$$

The function  $\rho(e)$  goes up less quickly than the increase of the input  $e$ . Then a suitable search scheme should be planned. For example, the simplest scheme is trying each and every available alignment exhaustively, i.e., making a full search. However, it is too time-consuming in practice. Thus, hierarchical coarse-to-fine schemes are developed to overcome the issue. Rough models of the panorama can also benefit the aligning stage by confining the search range to only the adjacent images to achieve faster and more accurate alignment.

## 2) Feature-based registration

The feature-based approach first extracts salient features from the images and then aligns the features to set up a general corresponding relationship. After that, the estimation of the geometric transformation between the images can be made.

Interest points can be detected using the lowest eigenvalue of the Hessian matrix of the images. Feature detectors that are less variant to scale (Lowe, 2004) and affine transformations (Mikolajczyk and Schmid, 2004) have been presented. The detectors are very suitable for aligning images with different scales.

The detected features (interest points) must be accurately aligned to determine the corresponding locations in the images. After the rough aligning, algorithms with higher accuracy can be employed to iteratively refine the alignment. An approach named RANSAC, i.e., RANdom SAMple Consensus, is commonly applied to estimate a robust model. RANSAC works iteratively to realise robust estimation to fit mathematical models from a series of observations probably containing outliers (Chen *et al.*, 1999; Brown & Lowe, 2007). The outcome of the algorithm is not guaranteed

to be a decent result but only with a level of probability, which increases with more iterations performed. It is a probabilistic method, which means different results might be achieved for every execution of the algorithm. The method assumes that the dataset contains inliers, namely data whose distribution adheres to some mathematical model, and outliers, which is data that does not conform to the model. Outliers are assumed to be the points resulting from parallax, noise, erroneous measurement results, moving objects, etc. To achieve homographic estimation, RANSAC attempts to fit several models with portions of the point pairs and then pick the model that matches the highest proportion of the point pairs. In this way, RANSAC succeeds in working out the model fitting problem. The lower proportion the outliers have in the dataset, the higher the possibility of yielding a decent model.

#### **4.2.2 Image blending**

After the images are registered, the blending issue should be considered, which involves the selection of the final composite surface and view, as well as optimally selecting and combining the pixels to minimise visible seams (owing to differences of exposure), blurring (caused by misregistration), or ghosting (because of moving objects) (Suen *et al.*, 2006). Image blending involves the pixel selection and adjustments, followed by the combination of the images (Mills & Dudek, 2009).

##### 1) Pixel selection and weighting

###### a) Optimal seam approach

This method searches for the curve in the overlapping area where the pixel differences between the corresponding points are minimised. Then the images are moved to different sides of the curve correspondingly. Seams caused by the curve are invisible if the differences are small. However, it is probable that such a seamless curve cannot be found when a large photometric discrepancy exists throughout the area. Furthermore, this method does not suit the circumstances with a narrow overlapping area, as the probability of finding a seamless curve is very low (Suen *et al.*, 2006).

###### b) Smooth transition approach

This approach soothes the transition between the images by replacing each overlapping pixel with weighted average of the corresponding pixel values of the images. The weighting coefficients are dependent on the distance from the pixel to the centre of the corresponding image. When the

images are well-registered, seams are generally insignificant, unless the photometric discrepancy is serious. However, blurring often arises when the images are misaligned. Despite Laplacian pyramid blending partially smoothing the transition in the frequency domain, some unwanted luminance alterations might occur within the non-overlapping areas of the blended image (Jia & Tang, 2008).

### c) Optimisation approach

The method acquires the stitched image via an optimisation procedure. The gradient-domain stitching method optimises an energy function related to pixel gradient values, with the goal of attaining a mosaic image whose pixel gradient values are approximate to those of the input images. This approach can yield seamless results even when both photometric discrepancy and misregistration exist. However, the cutting curve might be remarkable when there is non-uniform photometric discrepancy (Suen *et al.*, 2006).

## 2) Blending

After the seams are located, the combination of the images still needs to be done while eliminating the exposure differences and other misregistrations. The smooth transition approach can partially accomplish this goal. However, it is a real challenge to achieve a balance between smoothing out low-frequency luminance alterations and reserving relatively sharp (high-frequency) transitions to avoid blurring.

### a) Laplacian pyramid blending

The approach employs a transition with adaptive widths relevant to the frequency instead of a fixed width, which is achieved by setting up a band-pass (Laplacian) pyramid and making the transition widths conform to a function of the pyramid level (Xiong & Turkowski, 1998). The working process is summarised as follows:

First, each of the warped images is transformed into a band-pass (Laplacian) pyramid to form a reversible and overcomplete depiction. This is accomplished by smoothing all the levels with a binomial kernel and then subsampling the smoothed images by a factor of two, before subtracting the reconstructed images, respectively, from the original. Invalid pixels and the pixels on the edge are filled with adjacent values.

Next, each of the mask images is converted into a low-pass (Gaussian) pyramid. The blurred and subsampled masks are employed as the weights for calculating the per-level feathered blends of the source images respectively.

Finally, the blended image is acquired by incorporating all of the pyramid levels.

#### b) Gradient domain blending

The blending can be performed alternatively in the gradient domain. Instead of copying pixels, the gradients of the image fragments are employed. The pixel values for the image fragments being copied can then be calculated by solving a Poisson equation while satisfying the Dirichlet criteria at the seam curve (Levin *et al.*, 2004).

### 4.3 Stitching interferometry

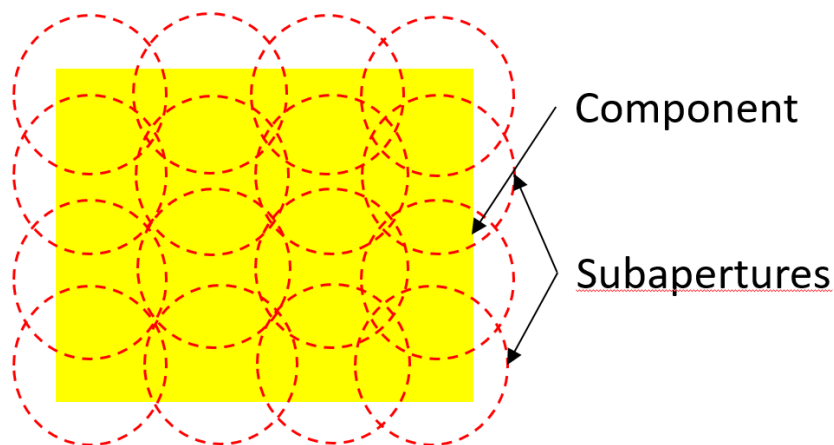


Figure 4.1 The subaperture stitching measurement.

The fundamental principle of subaperture stitching interferometry is to stitch subapertures together to measure a large component that is too large to be inspected in one step, as illustrated in Figure 4.1. The idea of this technique was first presented by Kim and Wyant in an annual meeting organised by Optical Society of America (OSA) and by Thunen and Kwon in a conference organised by SPIE individually in the early 1980s (Kin & Wyant, 1981; Thunen & Kwon, 1983). However, it takes numerous efforts to get an appropriate implementation of the technique with decent performance. For example, each subaperture measurement is inevitably affected by mechanical positioning error owing to air turbulence, thermal instability, environmental vibrations,

etc. Therefore, the post-processing is required to reduce the impact. Another challenge is to handle the risk for measurement error amplification during the stitching process (Bray, 1999).

Addressing and correcting error sources is usually challenging because there is usually nothing for reference. Some error sources can be eliminated via the hardware. For instance, mechanical vibrations can be removed through a vibration insulation mechanism. Some measurement errors can be compensated by the stitching algorithms based on the redundant information between overlapping subapertures. Therefore, sometimes the accuracy of the stitching interferometer is even higher than the normal interferometer (Bray, 2009).

In practice, a stitching interferometric system is very complicated because it must seamlessly incorporate an interferometer with alignment, algorithms, and control software. Although subaperture stitching interferometry works well in measuring large components, it cannot manage structured surfaces with sudden jumps for the normal vectors of the surface owing to a lack of overlapping measurable areas.

#### **4.4 Summary**

This chapter reviewed subaperture stitching interferometry (SASI), which combines interferometry and stitching technique together to realise large-scale measurement. It is similar to the method employed in this thesis in terms of the dataset combination. From the next chapter on, practical work will be discussed, such as the apparatus and the signal processing of the system.

## 5 Dual-probe wavelength scanning interferometry measurement system

### 5.1 Introduction

This chapter presents the design and implementation of the apparatus of the dual-probe wavelength scanning interferometry (DPWSI) system for measuring near-right-angle V-groove structured surfaces. As a result of the lack of effective means of measuring the structured surfaces, irrespective of contact or non-contact instruments, DPWSI was developed to overcome part of the challenge, namely achieving the measurement of near-right-angle V-groove structured surfaces. The reason to adopt wavelength scanning interferometry (WSI) is because WSI can achieve areal measurement with axial resolutions approaching the nanometre without the requirement for the mechanical scanning of either the sample or optics, unlike comparable techniques such as coherence scanning interferometry (CSI). This lack of mechanical scanning opens up the possibility of using a multi-probe optics system to provide simultaneous measurement with multi adjacent fields of view. For a given probe, a range of angles can be measured, restricted by the acceptance angle of the employed interference objective. It can be anticipated that this range can be expanded further by designing replaceable probe heads with varying angular separations.

### 5.2 System scheme

The requirement for the DPWSI system is to achieve areal measurement with nanometre scale vertical and micrometre level lateral resolution. The specific performance targets for the proposed measurement system are listed in Table 5.1. As a proof-of-principle demonstration, the thesis focuses on realising the measurement of the specific structured surfaces. Part of the processing is still manual and does not work automatically. Thus, the measurement speed is not considered in this thesis.

Table 5.1 Performance targets

Performance target	Value
Measurement range	$> 1 \text{ mm} \times 1 \text{ mm}$
Vertical resolution	$< 30 \text{ nm}$
Lateral resolution	Diffraction limited
Accuracy	$< 100 \text{ nm}$

The schematic configuration of the DPWSI system is illustrated in Figure 5.1. The system is comprised of three modules: light source, interferometer, and console, which are discussed in detail, respectively, in the following sections.

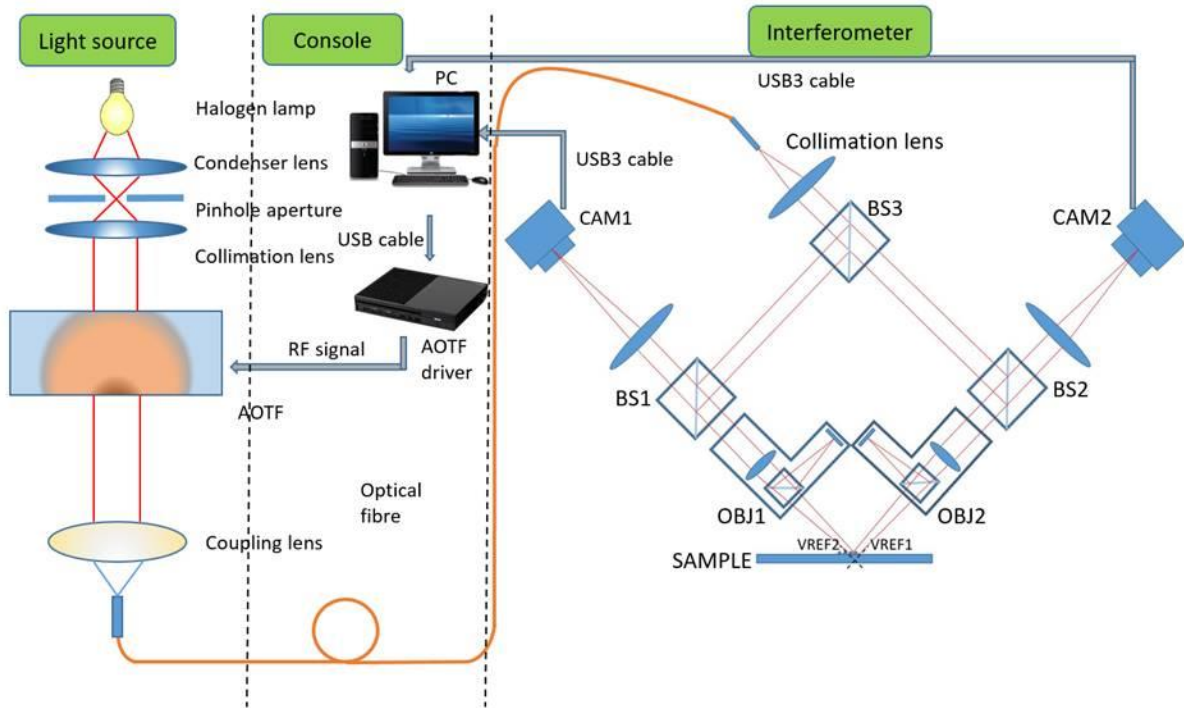


Figure 5.1 Block diagram of the DPWSI system showing from left to right: the light source, console, and dual-probe interferometer (adapted from Zhang *et al.*, in-press).

### 5.3 Light source

The illumination scheme is chosen depending on the measurement application scenario, namely the nature of the measurand. Generally speaking, monochromatic illumination is mainly employed by PSI system for smooth optical surfaces, whereas spectrally broadband illumination can be adopted for measuring objects with larger discontinuities (Malacara, 2007). For WSI, a monochromatic or quasi-monochromatic illumination scheme with varying wavelengths realised by applying tunable laser or acousto-optic devices is required to achieve wavelength scanning.

The light source plays an important role by providing tunable, parallel and monochromatic illumination to the measurement system. For this reason, a specific light source was produced to perform the wavelength scanning based on the previous design (Muhamedsalih, 2013). Because there is no vibration compensation mechanism, the optics for achieving that, such as the SLED (superluminescent light emitting diode) and the dichroic filter was removed. The light source

comprised a filament tungsten-halogen bulb (including the electrical circuits for lighting the bulb, such as a transformer, fuse, etc.), collimation lens, an acousto optical tunable filter (AOTF), a coupling lens, and so forth. The AOTF filtered a narrow band from a broadband source, namely the tungsten-halogen lamp. The filtered quasi-monochromatic light beam was coupled into a multimode fibre by the coupling lens before subsequently illuminating the interferometer module. The central wavelength of the output light beam was controlled by the RF signal generated by the AOTF driver. The AOTF driver was connected to a PC that controlled the amplitude and the frequency of the output RF signal, which will be described in detail in the next section. All of the components were fixed in an aluminium box, the high thermal expansion coefficient seems to have very little impact. Invar which features low thermal expansion coefficient was also tested before, but the difference was negligible. The mechanical design is illustrated in Figure 5.2 and more details can be found in Appendix B.

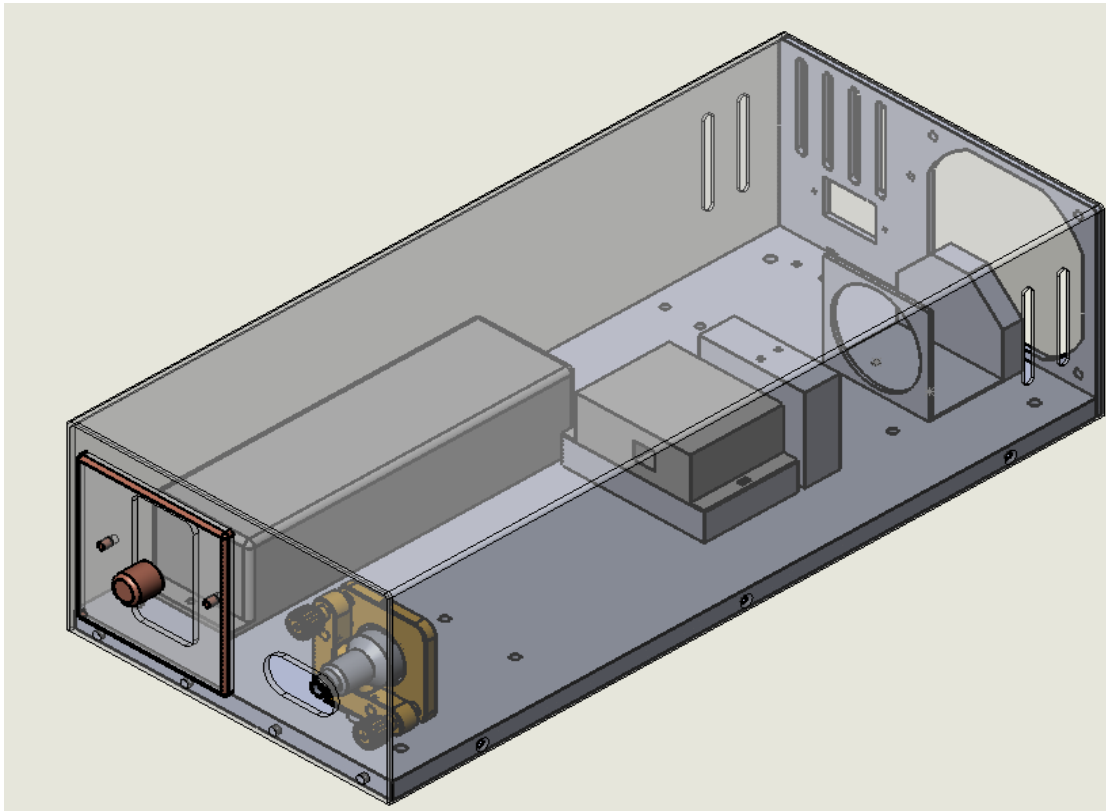


Figure 5.2 The mechanical design of the light source.

Regarding the wavelength scanning, the light source has to satisfy the following requirements:

- 1) a wide wavelength scanning range (approximately 100 nm).
- 2) linear scanning behaviour (wavenumber is scanned linearly).

3) the coherence length is long enough (longer than the depth of field of the interferometric system, which is about 55  $\mu\text{m}$ ).

The light source was designed to satisfy these requirements. The AOTF was able to select the wavenumber, namely the reciprocal of wavelength linearly during the scanning process. The linewidth of the filtered light was primarily determined by the acceptance angle of the AOTF crystal (Ward *et al.*, 2006).

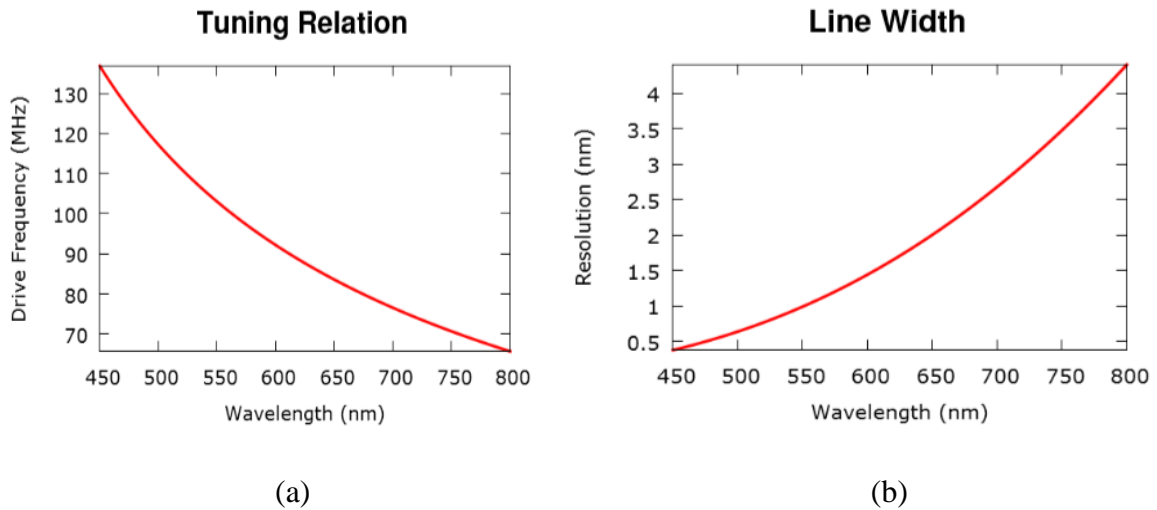


Figure 5.3 Spectral characteristics of AOTF (adapted from Gooch and Housego): (a). Tuning relation, namely the relationship between the output wavelength and the driving frequency; (b). The variation of the line width related to the selected output wavelength.

The AOTF was adopted to rapidly and dynamically select a specific wavelength from a broadband illumination source with high monochromaticity (linewidth about 2 nm within the scanning range). The physical principle of AOTF is the refractive index of acousto-optic material, such as tellurium dioxide ( $\text{TeO}_2$ ), varies when a RF driving signal is applied, creating a diffraction grating whose passband changes correspondingly. When a coherent light beam transmits through the crystal, only a narrow band of wavelengths that satisfy the phase-matching criterion will interfere constructively and be transmitted efficiently to exit the crystal at an angle that differs from the remainder of the beam (Bucher & Carnahan, 1999). As illustrated in Figure 5.3, the selective diffraction of light with respect to the wavelength allows the crystal to act as a tunable bandpass filter (Xu & Stroud, 1992). As the frequency of the RF driving signal varies, the central wavelength of the diffracted passband changes. The linewidth of the diffracted light beam is small, typically about 2 nm within the scanning range. The primary advantage of an AOTF over other wavelength selection devices is speed. One wavelength tuning operation can be accomplished in tens of microseconds. The

central wavelength of the illumination light diffracted through the AOTF can be determined by the equation:

$$\lambda = \alpha \Delta n \frac{v_a}{f_a}. \quad (5.1)$$

where  $\alpha$  is a constant that depends on the incident angle of entrance light beam,  $\Delta n$  is the birefringence crystal refractive index, and  $v_a$  and  $f_a$  are the propagation velocity and the frequency of the applied acoustic wave respectively. As the wavelength scanning range is limited, the parameters  $\alpha$ ,  $\Delta n$  and  $v_a$  can be seen as constant, which means the wavenumber

$k = \frac{1}{\lambda} = \frac{f_a}{\alpha \Delta n v_a}$  changes linearly during the wavelength scanning process as  $f_a$  varies linearly.

Figure 5.3 also shows the variation of the linewidth of the diffracted light beam through the AOTF. It can be seen that the linewidth becomes narrower with the selected wavelength getting shorter. Therefore, the power of the diffracted light also gets lower, which would cause the intensity variation of the captured signal by the camera even if no interference exists. Muhamedsalih, in his thesis, characterised the luminance variation during the wavelength scanning (Muhamedsalih, 2013). Therefore, the luminance variation should be considered when analysing the interference fringes to avoid the confusion.

## 5.4 Console

The console acts as the controller and interface that connects and controls all the modules in the system. For each measurement, the wavelength scanning of the illumination light is controlled and synchronised by software running on the PC through the AOTF controller. The same as the system used in Muhamedsalih's thesis (see Appendix C), 256 frames of interferograms are captured by the corresponding cameras and then analysed to acquire the measurement volume information of each probe respectively with a fringe analysis algorithm, such as the phase slope method or fringe order determination algorithm (Muhamedsalih, 2013), which will be discussed in Chapter 6 in detail.

### 5.4.1 AOTF controller

The core component of an AOTF is the acousto-optic material whose refractive index can be varied to form a diffraction grating whose passband changes correspondingly when a RF driving signal

is applied. The central wavelength and power of the transmitted light beam are controlled by the frequency and amplitude of the RF driving signal, which is produced by the AOTF controller. The AOTF controller is a small electronic box that generates the RF signal for driving the AOTF.

An AOTF controller is typically comprised of a RF oscillator, modulating circuits, as well as an adjustable power amplifier. The transducer inside the AOTF precisely converts the RF signal to an acousto-optic wave in an interactive optical material at a fixed or variable frequency based on the piezoelectric effect. The frequency and power of the output RF signal, which determines the wavelength and intensity of the diffracted light beam, can be controlled by programming. The controller offers high stability and linearity with short switching time and high resolution.

#### **5.4.2 Software console**

The wavelength scanning and data capturing process was controlled and synchronised by software running on a PC. The software was designed and implemented to achieve wavelength scanning by controlling and synchronising the AOTF configuration, as well as capturing images with the two USB 3.0 cameras, as illustrated in Figure 5.1. The images of the two cameras could be previewed on two screens, respectively, which would simplify the alignment work by enabling the simultaneous monitoring of the status of the two interferometers. A screenshot of a window is shown in Figure 5.4. There are two drop-down boxes to select the two cameras corresponding to the two interferometers, which enables the real-time monitoring of the sample under test. Just by clicking the “PREVIEW” button, the status of the two cameras can be monitored. The cameras were manufactured by Pixelink Co. Ltd. The software development was accomplished based on Pixelink’s software development kit (SDK).

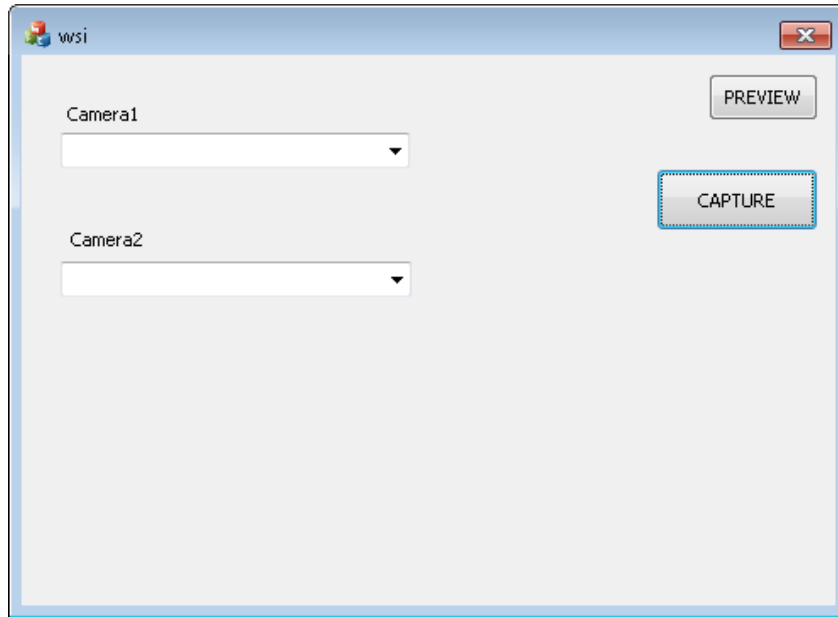


Figure 5.4 A screenshot of the software.

As the wavelength of the illumination light could be controlled by the software via the AOTF controller, the wavelength scanning could be combined with the data-capturing process by merging the code controlling the AOTF into the software of the cameras. The scanning and capturing process is as shown in Figure 5.5. With this program, the interferogram capturing operation was achieved by simply clicking the “CAPTURE” button, then two sets of interferograms would be captured, respectively, each for the corresponding interferometer.

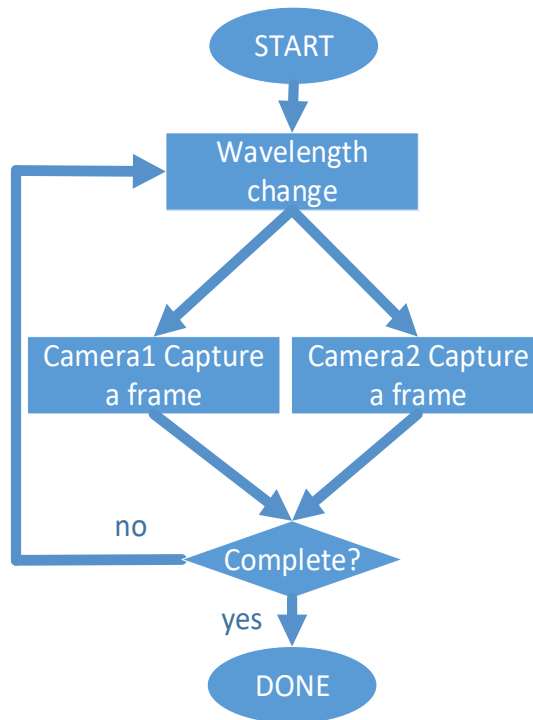


Figure 5.5 The wavelength scanning and data-capturing process.

## 5.5 Interferometer module

The interferometer module, namely a dual-probe WSI (DPWSI) apparatus, is the actual module achieving surface measurement. As illustrated in Figure 5.1, the module comprises two sets of cameras and interference objectives, with each set forming an interferometric measurement probe. The two identical interference objectives are orthogonally placed for micro and nanoscale areal surface measurement. Each of the probes in DPWSI measures a sidewall of a V-groove structured surface. After that, the two measurement datasets are fused together to form the whole surface topography of the V-groove structured surface based on the calibration result of the relative location of the two probes.

### 5.5.1 Interferometric objectives

Modern interference microscopes have advanced hardware platforms with the implementation of digital data grabbing and vibration insulation, associated with replaceable interference objectives that substitute the traditional imaging microscopic objectives. The interference objective as a basic module enables flexible and convenient use of variable magnifying power and interferometric design based on the types of application. Four types of interferometric configurations, namely Michelson, Mirau, Linnik, and Fizeau, are widely adopted in interference objectives (Malacara,

2007). All these types of interferometers are based on two-beam interference and each type has its own field of application. For instance, the Fizeau setup is widely employed in single-wavelength or dispersive interferometry as a result of the unbalanced optical paths that require a relatively long coherence length (Kimbrough *et al.*, 2008). Therefore, it is not suitable for white light interferometry (WLI). In contrast, Michelson, Mirau, and Linnik interferometers have balanced optical paths between the measurement and reference arms, leading to relatively high fringe contrast (Chang *et al.*, 1999; Niehues *et al.*, 2012; Muhamedsalih, 2013). When the OPD is adjusted to zero, the highest fringe contrast is achieved in these three types of configurations.

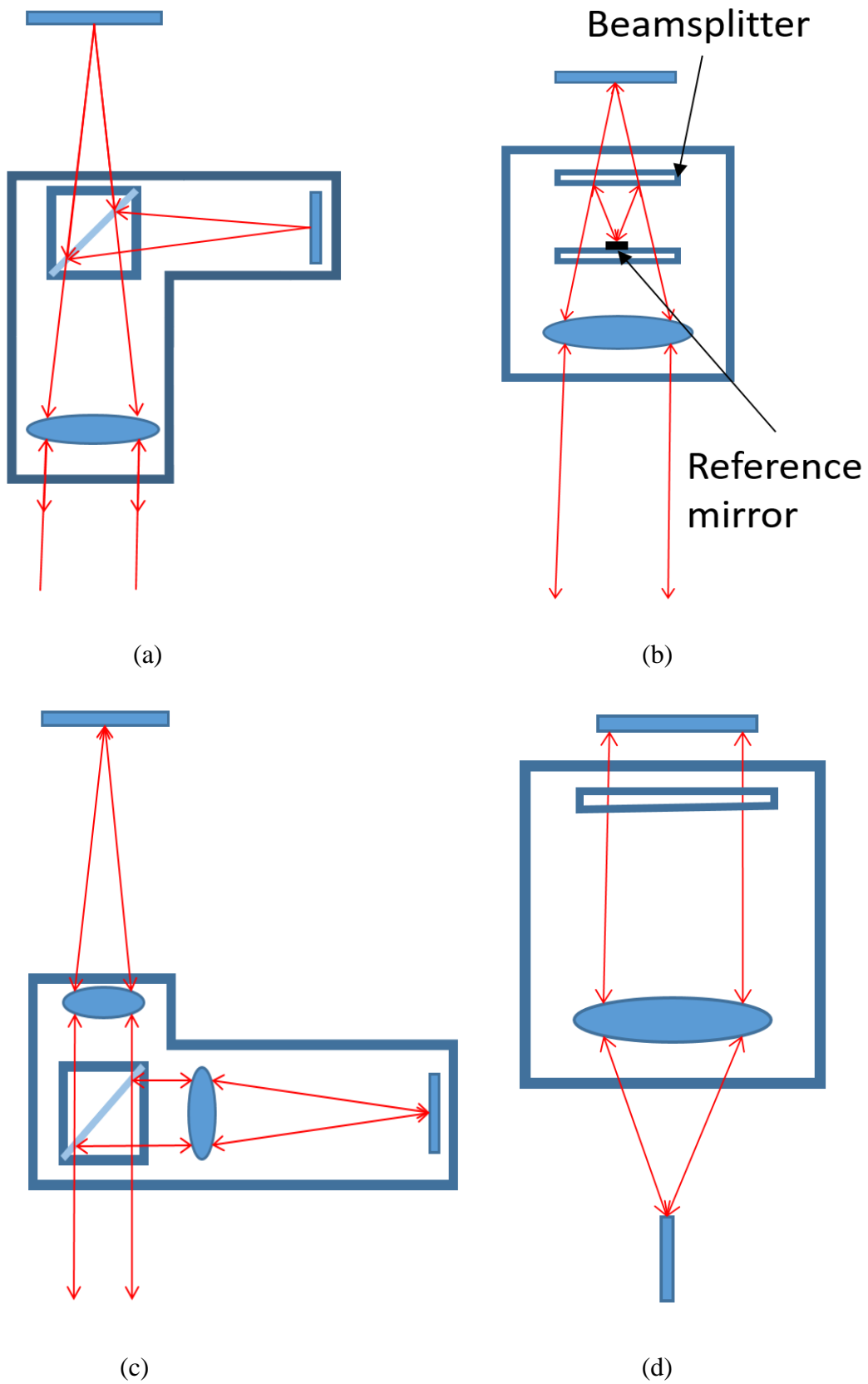


Figure 5.6 Different types of interference objectives: (a). Michelson; (b). Mirau; (c). Linnik; and (d). Fizeau.

The working distance, which is defined as the distance from the objective front lens to the specimen surface, is an important technical parameter for the design of the interference objective. The working distance is determined by a multitude of factors, such as interferometric geometry, lens design, etc. A long working distance is usually preferred and can be a decisive element in the selection of interference objective.

As shown in Figure 5.6(a), the Michelson setup splits the incident light beam into two beams with a cube beam splitter, then the two beams are recombined and interfere with each other after propagating through different routes. The cube beam splitter is positioned between the imaging lens and the inspected specimen, as well as the reference mirror. The apparatus balances the aberration caused by the imaging lens. However, the weakness is also apparent, i.e., the magnifying power and working distance are restricted by the imaging lens. For magnifications higher than 20X, there is insufficient space to provide accommodations for a large beam splitter between the imaging lens and the specimen. Therefore, the Michelson setup is not appropriate for applications requiring high magnifying power. The first interferometer utilised the Michelson setup, which endows it with great historical importance (Michelson & Morley, 1887).

The Mirau setup employs a parallel plate beam splitter to separate the incident light beam into two beams. It usually works at a medium magnifying power between 10X and 50X. When the magnification of the objective is higher than 50X, the working distance of the imaging lens is probably too short for inserting a glass plate in between the imaging lens and the inspected and reference surfaces, as shown in Figure 5.6(b). The Mirau is, by far, the most widely adopted geometry in interference objectives.

The Linnik objective is often applied in circumstances when high magnification is required. The Linnik objective solves the short working distance issue by inserting two microscopic objectives after the beam splitter, focusing the light beams to the test surface and reference mirror, respectively, as illustrated in Figure 5.6(c). For very high magnifications of 100X or above, there is no space to accommodate even a thin beam splitter plate. The Linnik objective holds respective imaging optics in both the measurement and reference arms to circumvent this issue. However, there are also some drawbacks to the Linnik objective. Firstly, it is more sensitive to environmental noise as there is another separate reference path with a microscopic objective. Moreover, the two microscopic objectives need to be well-matched to reduce the wavefront aberration in order to improve the quality of the captured interferograms.

To summarise, the Fizeau geometry is primarily adopted together with relatively high coherence illumination sources owing to the unbalanced optical paths, the Michelson is the preferred geometry for low magnifications (below 10X) while the Mirau setup is widely used for medium magnifications between 20X to 100X. The Linnik objective is utilised for very high magnifications of 100X or above (Malacara, 2007).

### 5.5.2 Objective selection

In this thesis, commercial interference objectives are employed to simplify the alignment work and make the system more compact, as the measurement is conducted simultaneously with the two interferometers, which should not disturb each other mechanically. Therefore, the working distance of the two objectives should be long enough in case that the two objectives clash into each other (see Figure 5.1 and imagine that the working distance of the objectives decreases) and also to enable the measurement of large-volume specimens. The FOV of the two interferometers should be large enough, which would be beneficial for the system calibration because more features could be covered to help improve the calibration accuracy. As a consequence, the magnifying power of the objectives should be lower than 20X.

Table 5.2 lists the specifications for different objectives manufactured by Polytec. The parameters for the objectives by other manufacturers are similar. After considering the magnification and the working distance, the Michelson interference objective A-IOB-004X with 30 mm working distance was selected.

Table 5.2 Specifications for different objectives

	Magnification	Working distance	Objective type
A-IOB-02X5	2.5x	10.3 mm	Michelson type
A-IOB-004X	4x	30 mm	Michelson type
A-IOB-005X	5x	9.3 mm	Michelson type
A-IOB-010X	10x	7.4 mm	Mirau type
A-IOB-020X	20x	4.7 mm	Mirau type
A-IOB-050X	50x	3.7 mm	Mirau type
A-IOB-100X	100x	2 mm	Mirau type

### 5.5.3 Alignment strategy

Traditionally, a combination of CCD camera and frame grabber was used for capturing the interferograms. However, in this thesis, USB 3.0 CMOS cameras manufactured by Pixelink Co. Ltd. were selected. This was an attempt to simplify the system and reduce the cost, although the transfer speed might be lower than CCD camera.

The first step of building up the apparatus is to choose a reflective specimen with near-right-angle V-shaped structured surface. The reflectivity of the specimen should be high and the reflective area should be smooth and relatively large in order to reduce the difficulty in achieving high-visibility interference fringes. For example, a right-angle prism made of glass is not a good option as it is transparent and of low reflectivity. In contrast, a metallised prism with high reflectivity is more preferable.

Aligning two interferometers simultaneously and having the FOV of the two instruments adjoining on one specimen is challenging owing to the tight coupling between the two interferometers and the relatively small FOV (about 1 mm \* 1 mm). In addition, the interference fringes should be of high quality in order to maintain high accuracy (better than 100 nm) for the measurement, in other words, the orientation of both sides of the specimen should be finely adjusted in order that the normals of the two faces are parallel to the optical axes of the two interferometers, which results in the challenge, as the specimen is moved as a whole.

After many attempts, the apparatus was successfully built up and high-visibility and wide fringes were simultaneously achieved with both interferometers. The important tips are summarised below.

First, position the specimen properly, using the optical bench as a reference. Do not align the interferometers before positioning the specimen. Otherwise, as the position and orientation of the specimen are not traced, after aligning the first interferometer, it is very difficult to align the second interferometer without affecting the first one. Even if fringes can be achieved, the fringe quality is not guaranteed and is probably not suitable for accurate measurement. In addition, it is difficult to improve the fringe quality on the two interferometers because the adjustment of the specimen to improve the fringe quality of one interferometer would affect the fringe quality of the other interferometer.

The relative locations of the specimen and the two interference objectives are decisive, especially the orientations of the three components. When the orientations of the three components are well-adjusted, even if the OPD is too large for obtaining interference fringes, the fringes could be achieved merely by translating the components, with no need to adjust the tip-tilt, which simplifies the work significantly.

An assembled stage, which comprises two tip-tilt mounts and a rotation stage, was adopted to hold the specimen. As shown in Figure 5.7, the specimen is placed on the rotation stage, which helps to adjust the orientation of the ridge. Each of the two mounts is in charge of the tip-tilt of one face around the ridge respectively and loosens the couple in adjusting the orientations of the two faces. The assembled stage is connected to a translation stage with three degrees of freedom and a 25-mm motion range in each direction.

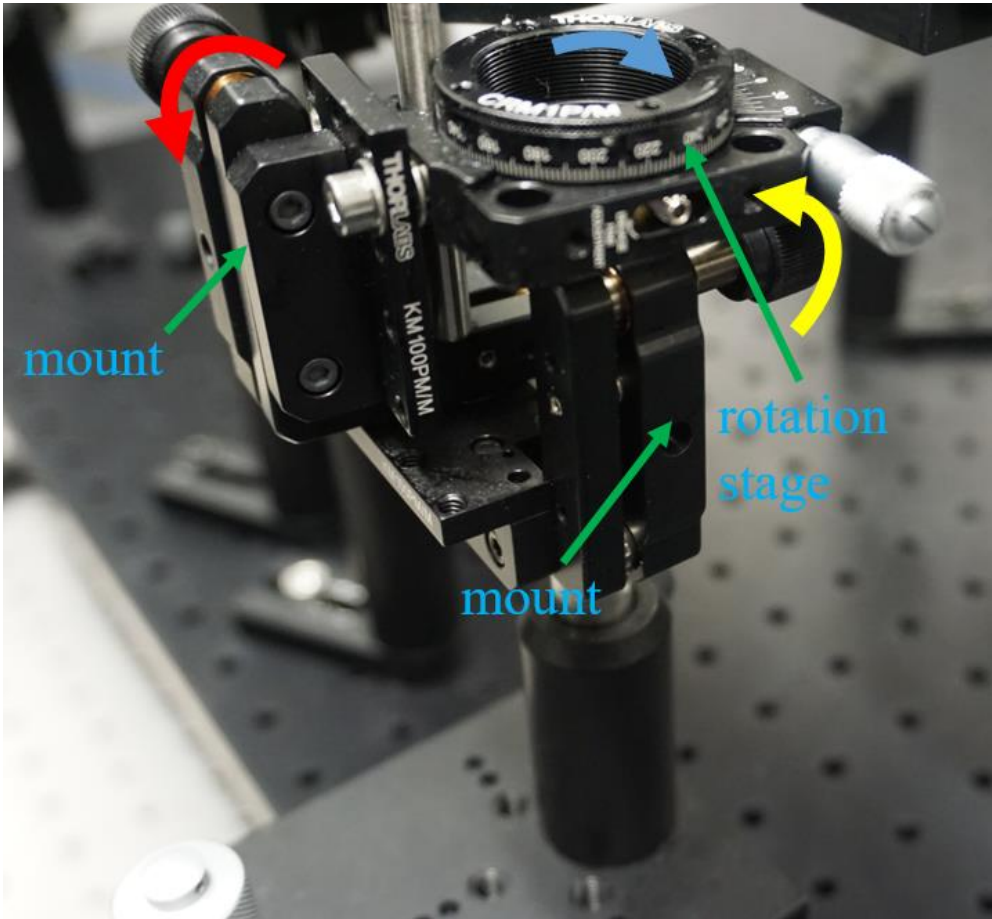


Figure 5.7 The assembled stage for holding the specimen.

A collimated laser diode module, Thorlabs CPS532-C2, is utilised for assisting the alignment, as shown in Figure 5.8. It is a laser safety class-II module that is safe and easy to use. The narrow

beam is very helpful in adjusting the orientation of the specimen. Using the optical bench as a reference object, the normals of the two faces can be made parallel to the optical bench by making the incident and reflected beams parallel to the bench, which can be ensured if the light beam is on the same height above the benchtop during the propagation. The laser diode also benefits the tip-tilt adjustment of the two interference objectives owing to the long coherence length. When nice and wide fringes are achieved with the laser source, the orientations of the specimen and the objectives are well-adjusted. The light spots of the two interference objectives need to be ensured to focus on the same height adjacent to each other so the measurable areas are adjoining. After switching to the white light source, nice and wide fringes can be achieved by mere translation to minimise the OPD because the coherence length is much shorter, with no need to adjust the tip-tilt. The laser diode can be kept on the apparatus to assist the alignment before measuring new specimens.

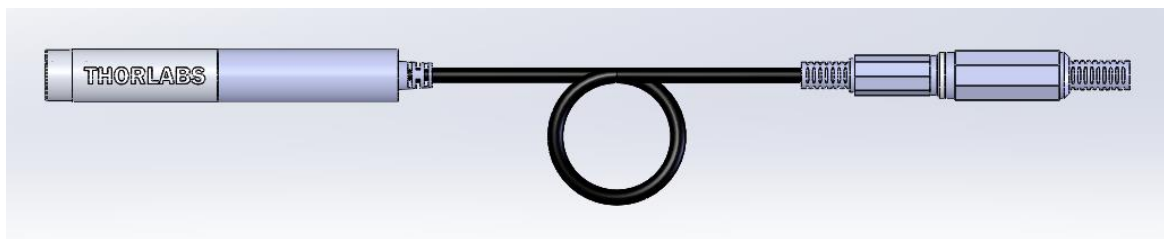


Figure 5.8 Thorlabs CPS532-C2.

The practical apparatus of the DPWSI system is as illustrated in Figure 5.9. Figure 5.10 shows the captured interferograms by the two interferometers of the DPWSI system. As the illumination light is split for the two interferometers, the intensity of the fringes is relatively low. However, the experiment shows the fringes can still be analysed to obtain the height information accurately.

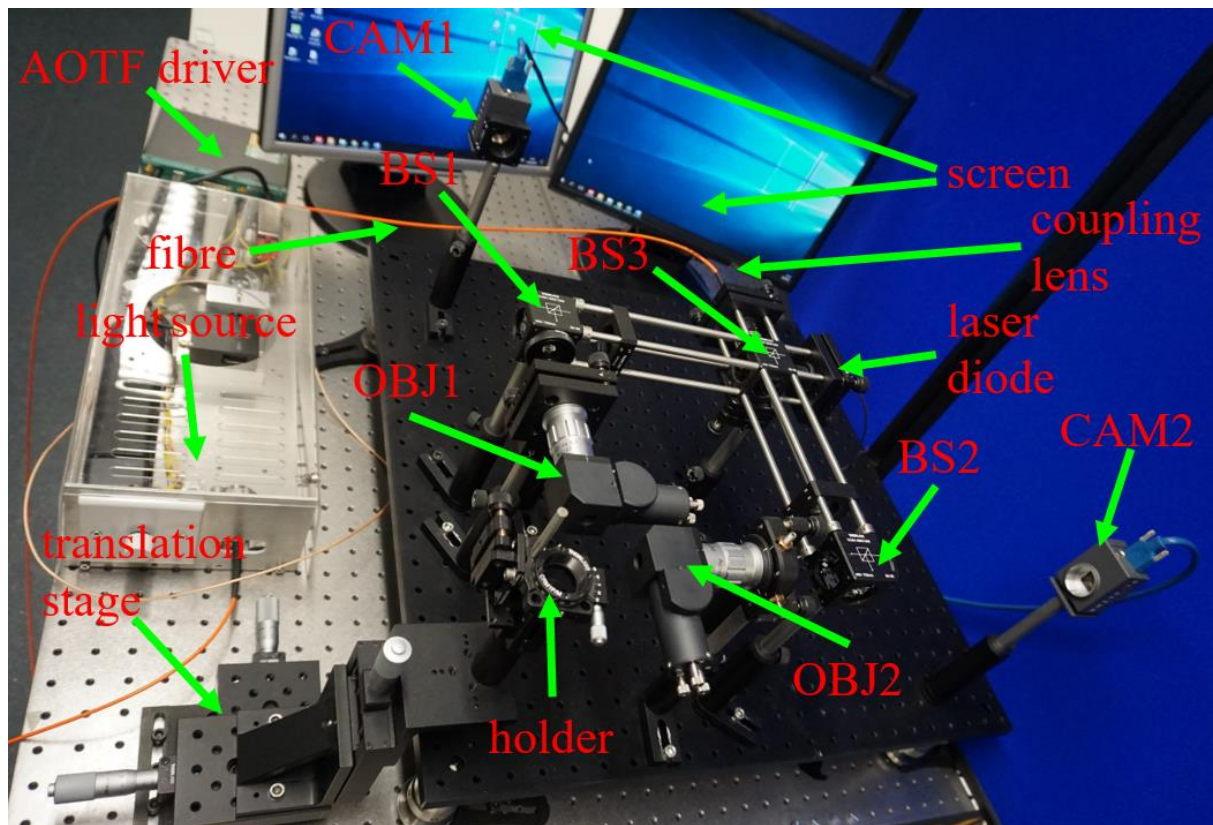


Figure 5.9 The practical apparatus of the DPWSI system.

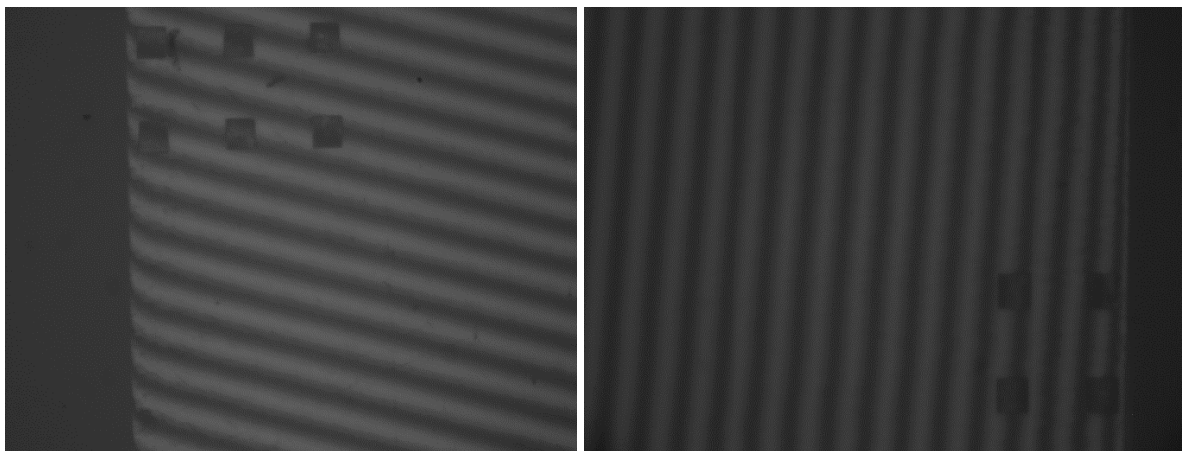


Figure 5.10 The interferograms captured by the two probes of the system.

According to the Rayleigh criterion, the lateral resolution of an optical system is  $r = 0.61 \frac{\lambda}{NA}$  which is diffraction limited, where  $\lambda$  represents the wavelength of the illumination light. In this study, the wavelength of the illumination source varies during the measurement process from 683.42 nm to 590.98 nm. Thus, the lowest lateral resolution is 4.1  $\mu\text{m}$  when  $\lambda$  is the largest (the NA of the interference objectives is 0.1).

## **5.6 Summary**

This chapter discussed the apparatus of the DPWSI system for inspecting near-right-angle V-groove structured surfaces, which was primarily comprised of a light source, console, and the interferometer module. All of the modules and the alignment strategy were discussed in detail. The fringe analysis algorithm, which is used for achieving the height information, will be described in the next chapter.

## 6 Fringe analysis

### 6.1 Introduction

The captured interferograms were analysed by using a fringe analysis algorithm to acquire the height information. The phase slope method which estimates height through the frequency of fringe pattern, and the algorithm which estimates height through fringe phase are the fringe analysis algorithms finding widespread applications in interferometry (Kato & Yamaguchi, 2000; Lehmann *et al.*, 2016). However, the performance of the fringe analysis algorithm is low when the captured signal has low quality. Figure 6.8(b) gives an example. Therefore, research into optimising fringe analysis algorithms is performed in this chapter, especially when the quality of the captured signal is low. The fundamental principle is discussed thoroughly, the filter design in these algorithms is especially focused on. Efforts to optimise the performance by using the optimal parameters for the filter design obtained through simulation are discussed. Experimental validation is also provided.

### 6.2 Interferogram processing principle

After the spectral interferograms are captured, algorithms are utilised to obtain the topography information in WSI. As shown in Figure 6.1(a), typically the interferograms frames are analysed pixel by pixel.

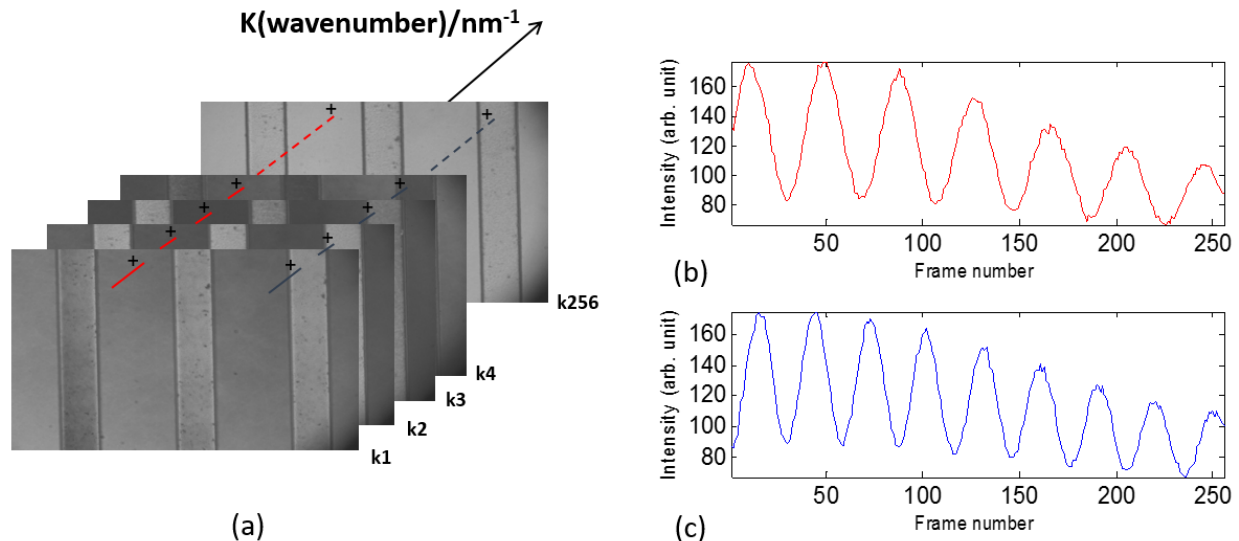


Figure 6.1 (a). The captured interferograms. (b) (c) the intensity signals captured by two pixels.

The overall fringe analysis process is illustrated schematically in Figure 6.2. The captured intensity signal is Fourier transformed and filtered, and then inverse Fourier transform is applied before extracting the phase information. Finally, the extracted phase information was analysed to acquire the height information (Muhamedsalih *et al.*, 2012). This chapter studies the impact of the filter design, on the fringe analysis algorithm for WSI, and improvements of the performance of the WSI by optimising the filter design.

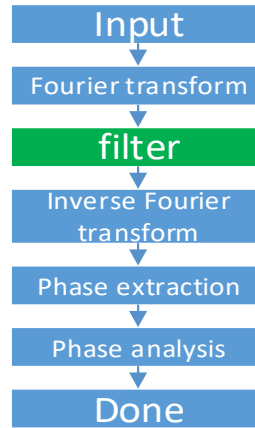


Figure 6.2 Schematic of the traditional fringe analysis process.

For each pixel across the series of the acquired frames for one measurement, an intensity signal similar to the periodic sinusoidal distribution is obtained for the corresponding point on the inspected specimen surface. Figure 6.1(b) and (c) are two examples. Eq. (6.1) provides the mathematical representation of the intensity signal,

$$I_{xy}(\lambda) = a_{xy}(\lambda) + b_{xy}(\lambda) \cos\left(\frac{4\pi h_{xy}}{\lambda} + \varphi_{0,xy}\right). \quad (6.1)$$

where  $a_{xy}(\lambda)$ ,  $b_{xy}(\lambda)$  represent the background intensity and fringe visibility respectively. Typically the variation rates of the components  $a_{xy}(\lambda)$ ,  $b_{xy}(\lambda)$  and  $\varphi_{0,xy}$  are much lower compared to the variation rate of  $\frac{4\pi h_{xy}}{\lambda}$ , where  $\lambda$  signifies the scanned wavelength,  $x$  and  $y$  refer to the row and column indices for the pixel of the areal CMOS sensor of the camera respectively. The central wavelength of the illuminating light transmitted through the AOTF can be calculated following Eq. (6.2).

$$\lambda = \alpha \Delta n \frac{v_a}{f_a}. \quad (6.2)$$

where  $\alpha$  is a constant which is dependent on the incident angle of the entrance light beam,  $\Delta n$  is the refractive index of the birefringence crystal,  $f_a$  and  $v_a$  are the frequency of the applied acoustic wave and the propagation velocity respectively. The wavenumber  $k$  is the reciprocal of the wavelength (Xu & Stroud, 1992). Since the range of the wavelength scanning is limited, the parameters  $\alpha$ ,  $\Delta n$  and  $v_a$  can be regarded as constant, which means, the variation of wavenumber  $k$  is linear during the wavelength scanning process since  $f_a$  changes linearly. The intensity signal can be characterised by Eq. (6.3)-Eq. (6.6) in both time and frequency domain.

$$\begin{aligned} I_{xy}(k) &= a_{xy}(k) + b_{xy}(k) \cos(4\pi k h_{xy} + \varphi_{0,xy}) \\ &= a_{xy}(k) + \frac{b_{xy}(k)}{2} e^{j\varphi_{0,xy}} e^{j4\pi h_{xy}k} + \frac{b_{xy}(k)}{2} e^{-j\varphi_{0,xy}} e^{-j4\pi h_{xy}k}. \end{aligned} \quad (6.3)$$

$$I_{xy}(k) = a_{xy}(k) + c_{xy}(k) e^{j4\pi h_{xy}k} + c_{xy}^*(k) e^{-j4\pi h_{xy}k}. \quad (6.4)$$

$$c_{xy}(k) = \frac{b_{xy}(k)}{2} e^{j\varphi_{0,xy}}. \quad (6.5)$$

$$\begin{aligned} FT(I_{xy}(k)) &= A(f) + C(f - 2h_{xy}) + C^*(f + 2h_{xy}) \\ &= A(f) + C(f - OPD) + C^*(f + OPD) \end{aligned} \quad (6.6)$$

where FT refers to Fourier transform and OPD signifies the optical path difference between the measurement arm and the reference arm. It can be seen from Eq. (6.6) that there are only a limited number of pulses in the Fourier domain of the intensity signal. In this circumstance,  $I_{xy}(k)$  is in the spatial frequency domain as a function of the wavenumber. Fourier transform of the function results in a function in the spatial domain. As a consequence, the coordinate  $f$  in Eq. (6.6) is a spatial coordinate (Bracewell & Bracewell, 1986). This is the reason why the shift between the frequency components is a length (OPD). The extraction of the effective signal  $C(f - OPD)$  or  $C^*(f + OPD)$  component from the low-frequency component  $A(f)$  can be achieved by applying a band-pass filter when OPD is large enough. This also gives an explanation why the OPD should be relatively large when carrying out the measurement, because otherwise the three components would overlap, making it impossible to extract the effective signal. After the extraction of the

effective component  $C(f - OPD)$  or  $C^*(f + OPD)$ , inverse Fourier transform (IFT) is conducted. Take  $C(f - OPD)$  as an example ( $C^*(f + OPD)$  is similar), then

$$\begin{aligned} IFT(C(f - OPD)) &= c_{xy}(k) e^{j4\pi h_{xy}k} \\ &= \frac{1}{2} b_{xy}(k) e^{j(4\pi h_{xy}k + \varphi_{0,xy})} \end{aligned} \quad (6.7)$$

Then the natural logarithm is applied and the phase information  $\varphi(k)$  is attained by taking the imaginary part:

$$\ln\left(c_{xy}(k) e^{j4\pi h_{xy}k}\right) = \ln\left(\frac{1}{2} b_{xy}(k)\right) + j(4\pi h_{xy}k + \varphi_{0,xy}). \quad (6.8)$$

$$\begin{aligned} \varphi(k) &= \text{imag}\left(\ln\left(\frac{1}{2} b_{xy}(k)\right) + j(4\pi h_{xy}k + \varphi_{0,xy})\right) \\ &= 4\pi h_{xy}k + \varphi_{0,xy} \end{aligned} \quad (6.9)$$

After that, the unwrapping of the phase information is done and the ratio between the phase variation ( $\Delta\varphi$ ) and the wavenumber change ( $\Delta k$ ) contains the height information because the variation rate of  $\varphi_{0,xy}$  is much lower:

$$h_{xy} = \frac{1}{4\pi} \frac{\Delta\varphi}{\Delta k}. \quad (6.10)$$

The above describes the steps by which the phase slope method can be used to analyse the fringes (Takeda & Yamamoto, 1994). Height estimation through phase algorithm works in a similar way but it analyses the phase and considers the dispersion and reflection effect as well (Moschetti *et al.*, 2016). The phase information is disassembled as below:

$$\varphi = 4\pi k h_{xy} + \tau(k - k_0) + \gamma_0. \quad (6.11)$$

where  $\tau$  refers to the dispersion difference between the reference arm and the measurement arm,  $\gamma_0$  signifies the phase bias on reflection. Consequently, the fringe pattern phase for the initial wavenumber can be calculated with  $2\pi$  phase ambiguity as (Moschetti *et al.*, 2016):

$$\varphi(k_0) = 4\pi k_0 h_{amb}. \quad (6.12)$$

The unambiguous height is (Moschetti *et al.*, 2016):

$$h = \frac{1}{4\pi} \frac{\varphi(k_0)}{k_0} + \frac{m}{2k_0}. \quad (6.13)$$

$$m = \text{round} \left[ \frac{1}{4\pi} \left( \frac{\Delta\varphi}{\Delta k} - \tau - \frac{\varphi(k_0) - \gamma_0}{k_0} \right) 2k_0 \right]. \quad (6.14)$$

Height estimation through the phase determination algorithm is not independent since the phase slope is also required for resolving the fringe order as shown in Eq. (6.14). Height estimation through phase algorithm has been shown to be able to achieve the improvement of the resolution by nearly a factor of ten (Moschetti *et al.*, 2016).

It can be inferred from Eq. (6.3) that the intensity signal  $I_{xy}(k)$  is a narrow-band sinusoidal signal, which means, in the frequency domain it appears as a narrow pulse. However, since the sequence of the real signal is limited, there exists some spectral leakage, although the spectral band is still narrow. The period of the  $I \sim k$  sinusoid is calculated following Eq. (6.15).

$$K = \frac{k_e - k_s}{N_c} = \frac{1}{f}. \quad (6.15)$$

where  $K$  signifies the period in the curve,  $k_s$  and  $k_e$  refer to the minimum and maximum wavenumber respectively during the scanning process.  $N_c$  denotes the number of cycles, while  $f$  represents the frequency in the curve. The sample frequency is:

$$f_s = \frac{N_{frm}}{k_e - k_s}. \quad (6.16)$$

where  $N_{frm}$  denotes the captured frame number during the process, while  $k_s$  and  $k_e$  signify the minimum and maximum wavenumber respectively in the scanning process. Therefore,

$$\frac{f}{f_s} = \frac{N_c}{N_{frm}}. \quad (6.17)$$

In this way the central frequency of the effective signal can be determined, namely the  $N_c$ th frequency bin in the FFT result (assuming the bins are counted from zero). For example, Figure 6.3(a) shows the intensity signal from a single pixel acquired during wavelength scanning. There are approximately 6 cycles evident in the time domain signal, so the signal lies in the 6th frequency bin in the Fourier domain, as shown in Figure 6.3(b). In this application, the ideal bandpass filter is employed since for other types of filters, the edge of the pass-band is not steep enough to effectively reject the noise. Since the frequency band of the signal is narrow, the filter should also have a narrow pass-band in order to maximally eliminate the noise, however this must be traded against filter ringing. The optimal results are attained by a compromise between the admitted noise and the effects of filter ringing. The passband of the filter should be relatively narrow when the signal quality is low. Conversely, the filter should feature a relatively wide passband when the signal has high quality in order to reduce the impact of filter ringing. This chapter focuses on deriving the conditions for balancing the noise and filter ringing in order to yield optimal results.

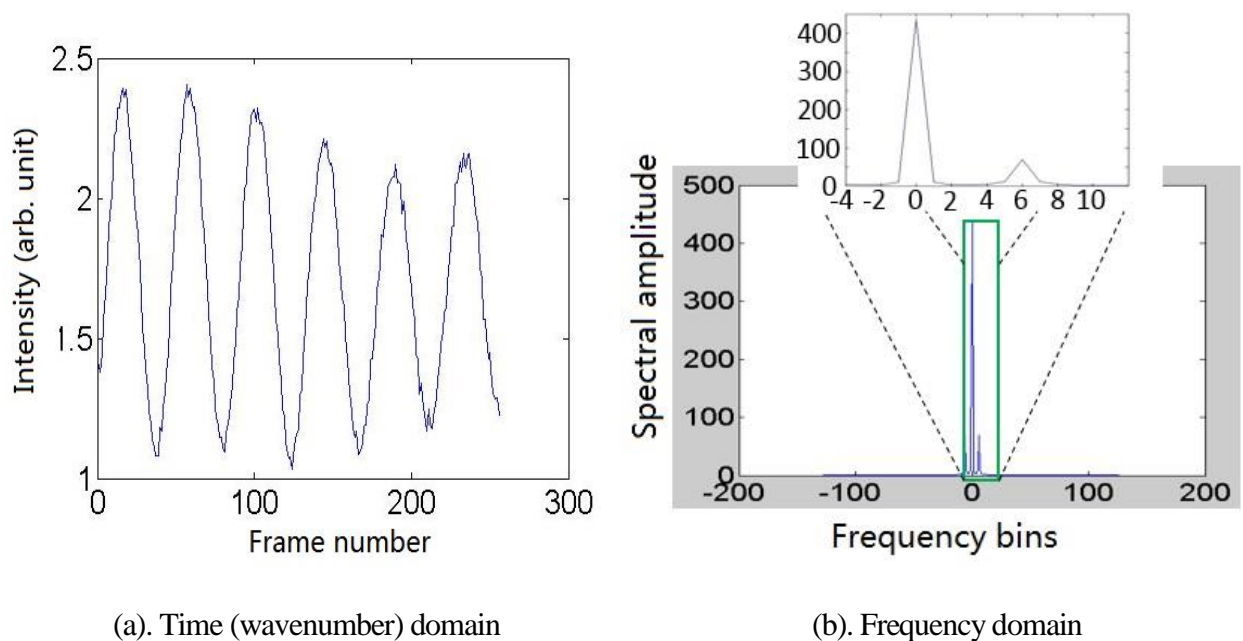


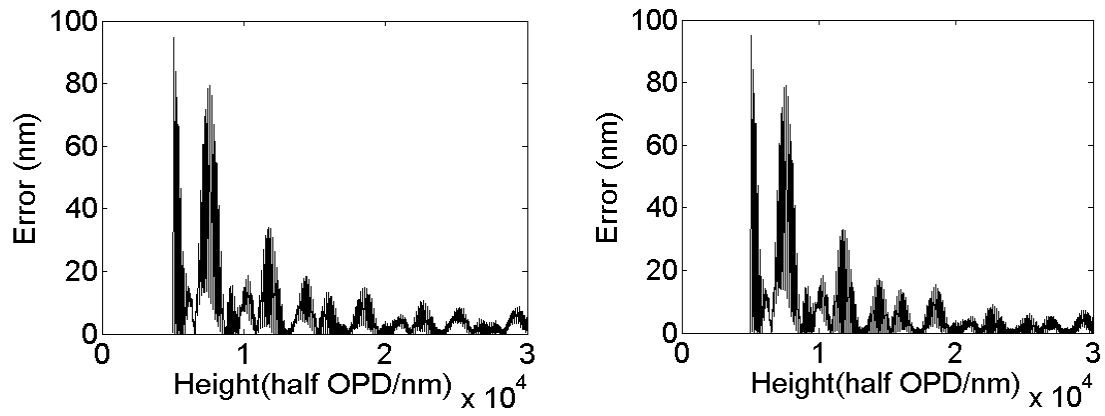
Figure 6.3 The signal in time domain and in frequency domain (adapted from Zhang *et al.*, 2018).

## 6.3 Simulation and experimental results

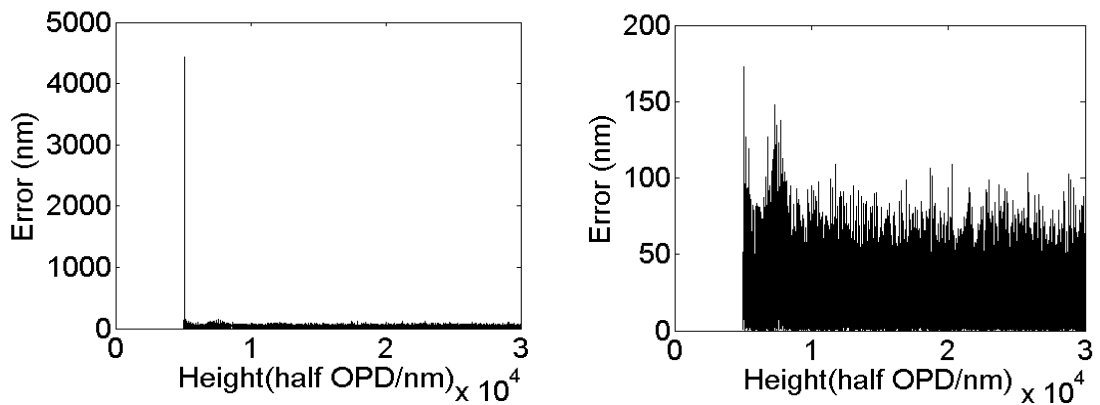
### 6.3.1 Simulation results

The fringe analysis algorithms were simulated numerically using Matlab where input signals were generated with specific SNRs (Jackson, 2013). Here SNR is an important input parameter for controlling the quality

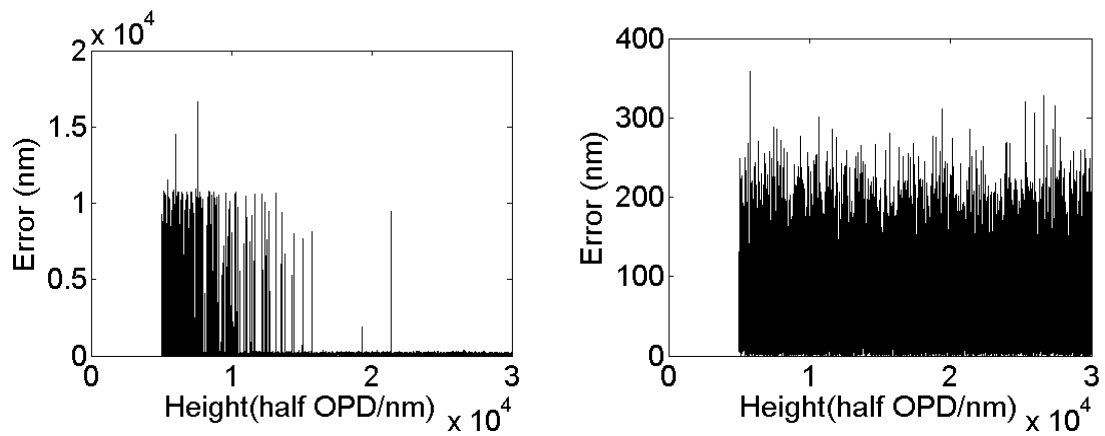
of the produced signal, by applying additive white Gaussian noise. Simulation was carried out to determine the optimal filter parameters for the signal featuring different levels of SNR exhaustively. A lookup table (LUT) was created to record the algorithm with higher performance and the optimised parameters corresponding to signal with different SNRs. The assessment is on the basis of the overall error and the robustness, which was evaluated from the difference between the maximum value and the mean value of the error. After that, the algorithm and the parameters are chosen in accordance with the LUT based on the estimation of the SNR of the captured intensity signal adaptively when performing fringe analysis. Only a rectangular window is utilised in the time domain although other types of windows such as Gaussian, Hann and Hamming windows are helpful in eliminating the ripple resulting from spectral leakage, since the simulation shows that other types of windows have negative impact on the robustness of the algorithm (Moschetti *et al.*, 2015). Since the filter is an ideal bandpass filter, it is characterised by the pass-band window in the frequency domain. The representation window (a:b) implies that the pass-band ranges from frequency bin a to frequency bin b. The DC component of the fringe pattern is removed by subtraction of the mean value. The amplitude of the error ringing declines with the growth of the OPD. When the OPD is small, the deviation is large even if the signal has very high quality due to the filter ringing. For this reason, when carrying out the measurement, the OPD should be relatively large but without exceeding the depth of field (DOF), otherwise the contrast of the fringe would be too low. As a result, the small OPD should be avoided when performing the measurement and is omitted in the analysis. Only those height values (equal to half of the OPD) above 5  $\mu\text{m}$  are considered in this chapter.



(a). 50dB SNR

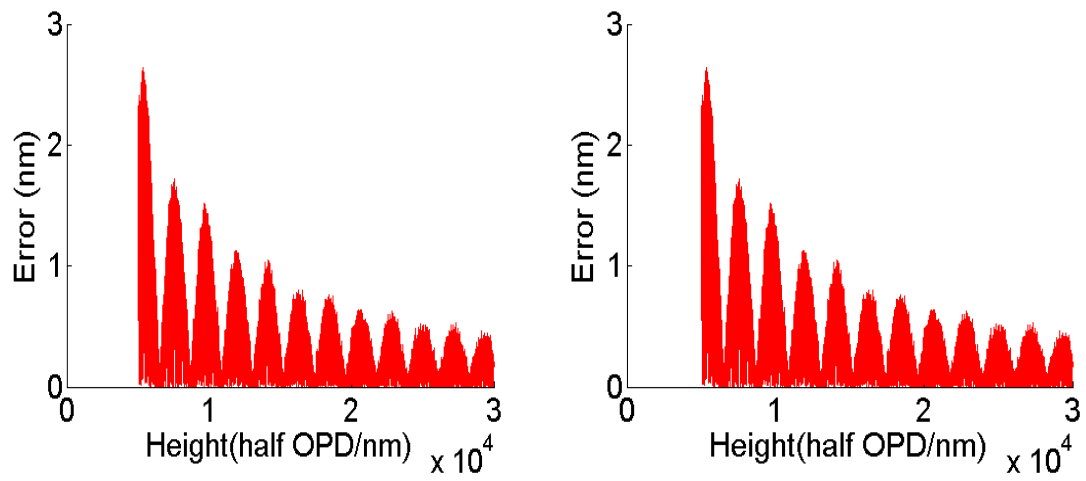


(b). 15dB SNR

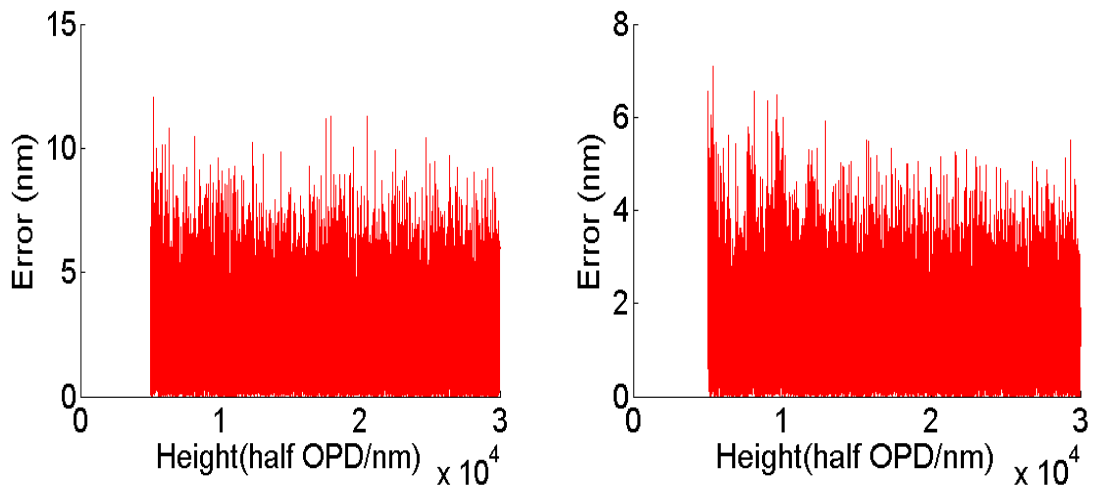


(c). 5dB SNR

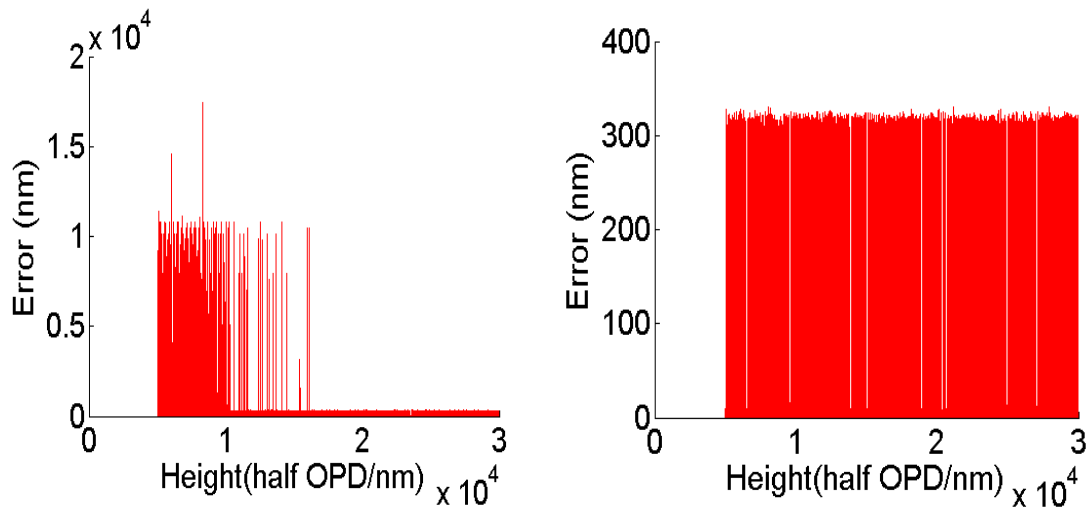
Figure 6.4 The simulation results of the signal with different SNR processed by phase slope method with different windows, with the window (2:25) on the left and optimised window on the right (adapted from Zhang *et al.*, 2018).



(a). 50dB SNR



(b). 15dB SNR



(c). 5dB SNR

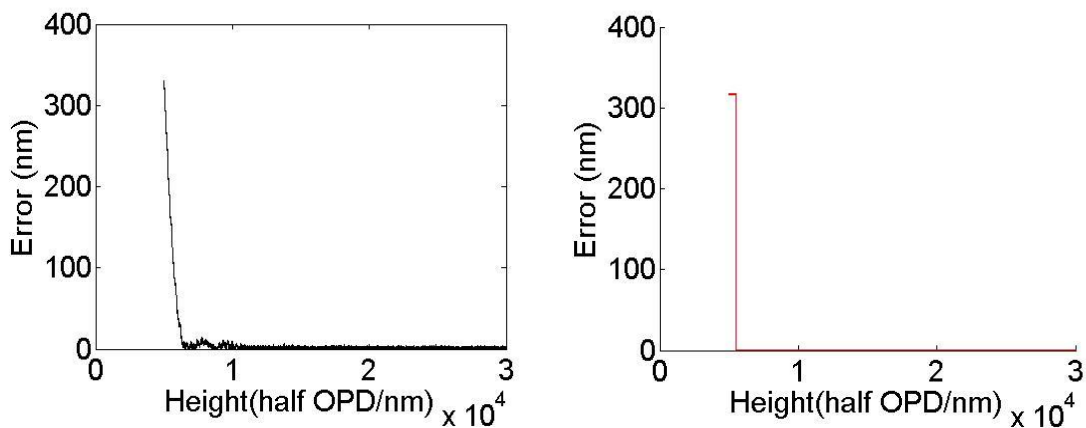
Figure 6.5 The simulation results of the signal with different SNR processed by height estimation through phase algorithm with different windows, with the window (2:25) on the left and optimised window on the right (adapted from Zhang *et al.*, 2018).

A constant window (2:25) was adopted in (Muhamedsalih *et al.*, 2012), therefore it is used for comparison in this chapter. Figure 6.4 and Figure 6.5 compare the simulation results processed with the window (2:25) and the optimised windows by applying the phase slope method and height estimation through phase algorithm respectively. The vertical axes (Error) characterise the difference between the resolved height and the actual height. Figure 6.4(a) and Figure 6.5(a) show the simulation results of low noise signal with 50dB SNR. The simulation indicates that the window (2:25) provides nearly optimal performance since the error predominantly originates from the ringing of the filter and when the width of the window increases, the ringing declines. Consequently, when the signal quality is high, a filter with relatively wide passband should be applied to reduce the ringing. It can also be seen that height estimation through phase algorithm has much higher performance than the phase slope method. In Figure 6.4(a) errors up to 95 nm can be observed, while in Figure 6.5(a) the errors are always lower than three nanometres. Figure 6.4(b) and Figure 6.5(b) present the simulation results of relatively low-quality signal with 15dB SNR. The simulation shows that the noise has large impact on the performance, which results in the narrower of the optimal window width in order that the noise is better eliminated. Specifically, for the phase slope method, the elimination of the noise is too weak when the passband of the filter is wide, leading to large error of up to several micrometres. In contrast, the noise is effectively filtered when the filter passband is narrow, thus the error is still not too large (below 200 nm). The height estimation through phase algorithm still provides much higher

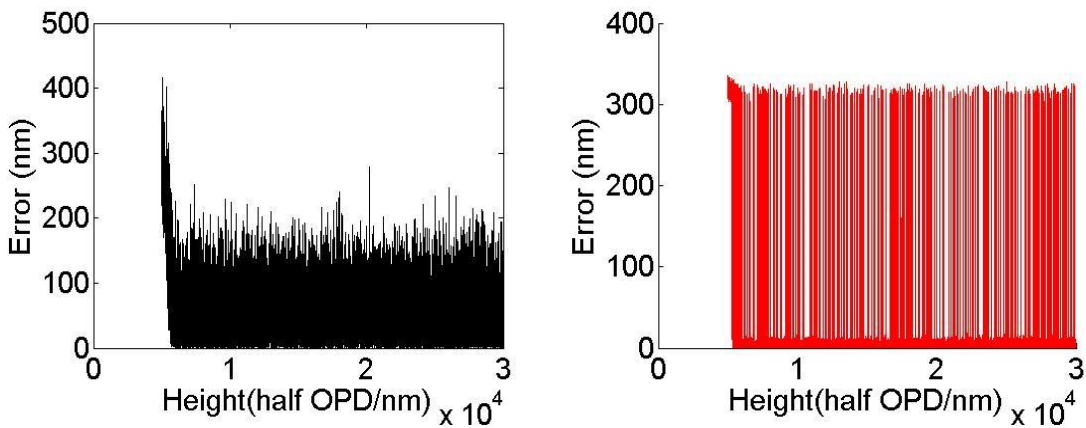
performance than the phase slope method. The performance improvement achieved via the filter design is also noticeable. The optimised window eliminates more noise and leads to higher accuracy in both Figure 6.4(b) and Figure 6.5(b). Figure 6.4(c) and Figure 6.5(c) provide the simulation results of very low-quality signal with only 5dB SNR. The results show that the noise has much larger impact than the filter ringing. When applying a filter with wide passband, the noise is too severe, resulting in deviation up to tens of micrometres for both the two algorithms. Meanwhile, when a filter with optimised passband is employed, the noise is significantly eliminated and the error is largely reduced. The measurement system is still able to achieve sub-micrometre accuracy for both algorithms. In both Figure 6.4(c) and Figure 6.5(c) the optimised window contributes by reducing the errors from up to 18  $\mu\text{m}$  to below 400 nm. The errors of height estimation through phase algorithm is in the same order of half a wavelength primarily caused by the erroneous determination of the fringe order. The performance of the phase slope method is in the same level as, sometimes even higher than height estimation through phase algorithm. Since the algorithm presented previously (Muhamedsalih *et al.*, 2012) employs a filter with constant, relatively wide passband, the measurement system has high performance when the signal quality is high (>20dB). When the SNR of the signal declines to 20dB, the measurement system generally works very well, but has very low possibility of getting micrometre scale deviation for some special cases. When the signal quality further deteriorates to a level with 10dB SNR, the algorithm almost cannot work properly because the deviation is too large. In contrast, the simulation indicates that the proposed algorithm is still able to achieve sub-micrometre level accuracy even when the SNR drops down to 5dB, which means, the proposed approach noticeably increases the resistance to the noise as well as the stability.

Based on this, the spectral leakage issue due to a limited signal sequence is revisited. Typically, this issue is resolved by multiplying a window function such as Hamming to the intensity signal in the time domain, namely acquiring their Hadamard product before the analysis using the optimised parameters. As an example, the simulation results adopting a Hamming window is shown in Figure 6.6. As can be seen, when the signal has high quality (SNR above 50 dB), the window function significantly improves the performance except when the OPD is small, there is possibility of encountering deviations of hundreds of nanometres, irrespective of the phase slope method or height estimation through phase algorithm. Apart from that, the performance is high, the errors of phase slope method are negligible, normally only several nanometres, while the errors of height estimation through phase algorithm is even better, achieving sub-nanometre level. However, since there is no *a priori* knowledge of the OPD before the measurement, the existence of the

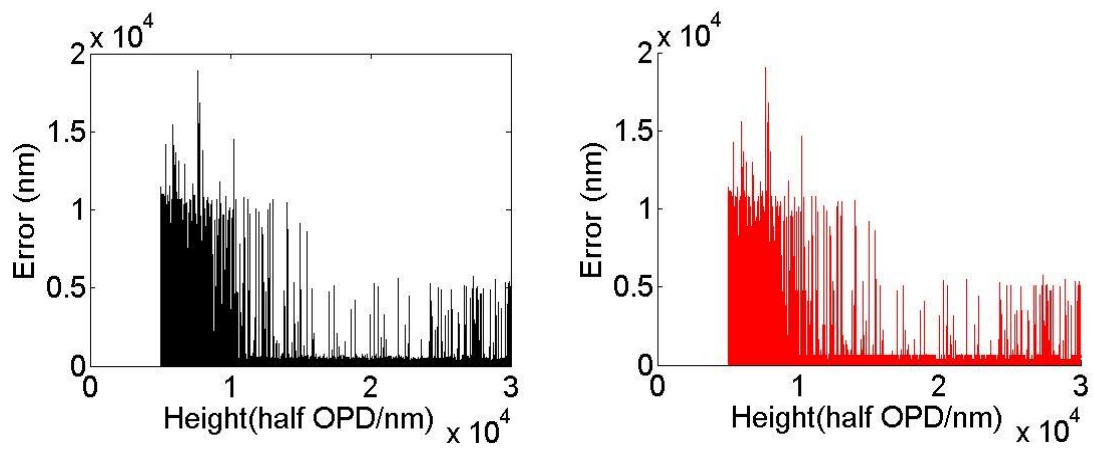
possibility of encountering large deviations is a threat to the robustness. Also it is nearly impossible to have a signal of such high quality with the instrument (The SNR for the actual signal cannot be accurately measured. However, the highest performance of the instrument is equivalent to the simulation result of the signal with 30 dB SNR. Therefore, the signal SNR is typically below 30 dB). When the signal quality declines, the performance lowers rapidly. The simulation results of 15dB and 5dB are apparently worse than the performance without applying the window. It is also worth mentioning that other types of FIR filters with lower ringing have also been simulated (Sedra & Brackett, 1978), but since the edge of the filter pass-band is not steep enough, the elimination to noise is too low. Therefore, the FIR filters have lower performance than the ideal filter.



(a). 50dB SNR

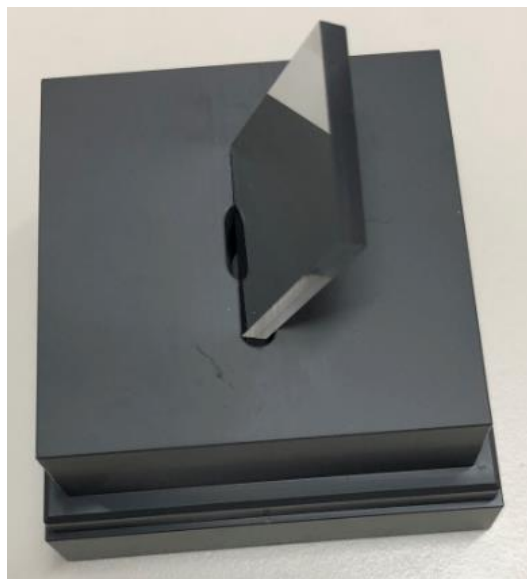


(b). 15dB SNR

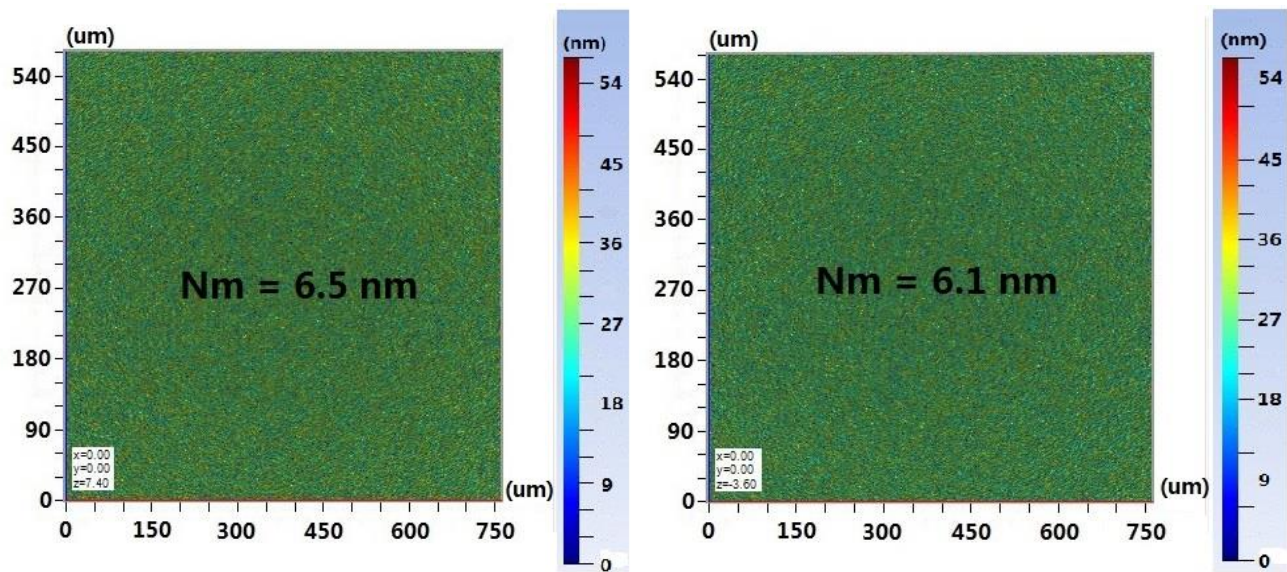


(c). 5dB SNR

Figure 6.6 The simulation results of the signal with different SNR multiplying a Hamming window (Hadamard product) processed by phase slope method and height estimation through phase algorithm with optimised windows, with phase slope method on the left and height estimation through phase algorithm on the right.

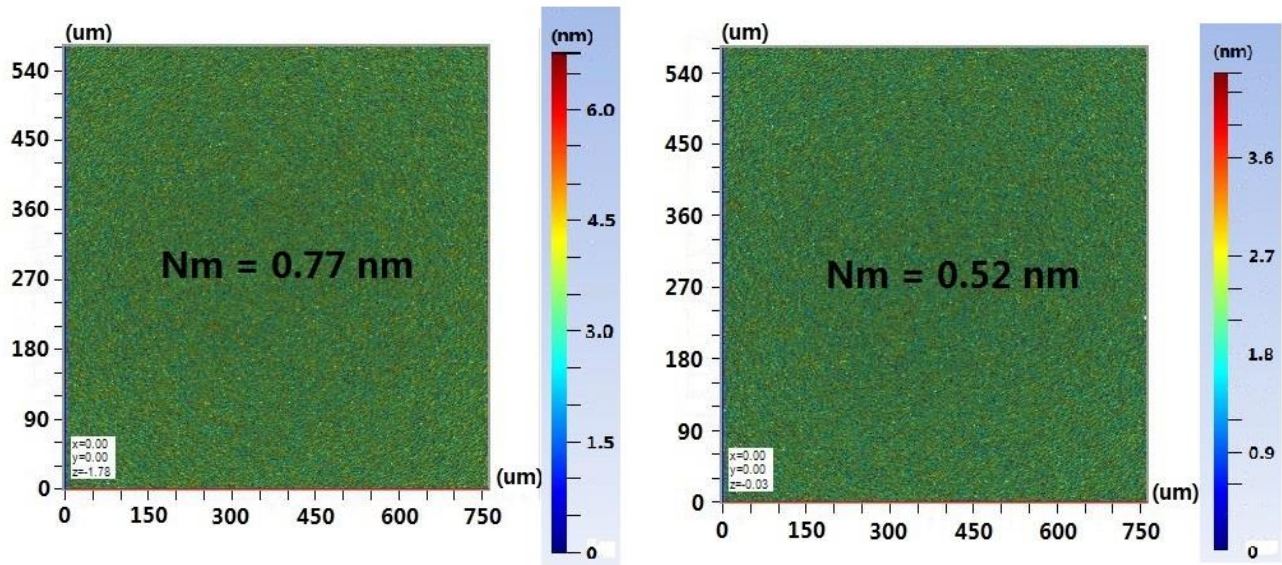


(a)



(b)

(c)



(d)

(e)

Figure 6.7 The measurement noise of a standard flat shown in (a), (b) (c) processed by phase slope method with the window (2:25) and optimised window respectively; (d) (e) processed by height estimation through phase algorithm with the window (2:25) and optimised window respectively (adapted from Zhang *et al.*, 2018).

### 6.3.2 Filter validation

Some experiments have been conducted for the validation of the simulation results. A step-height standard specimen manufactured by VLSI Standards, Inc., as illustrated in Figure 6.7(a), was inspected to evaluate

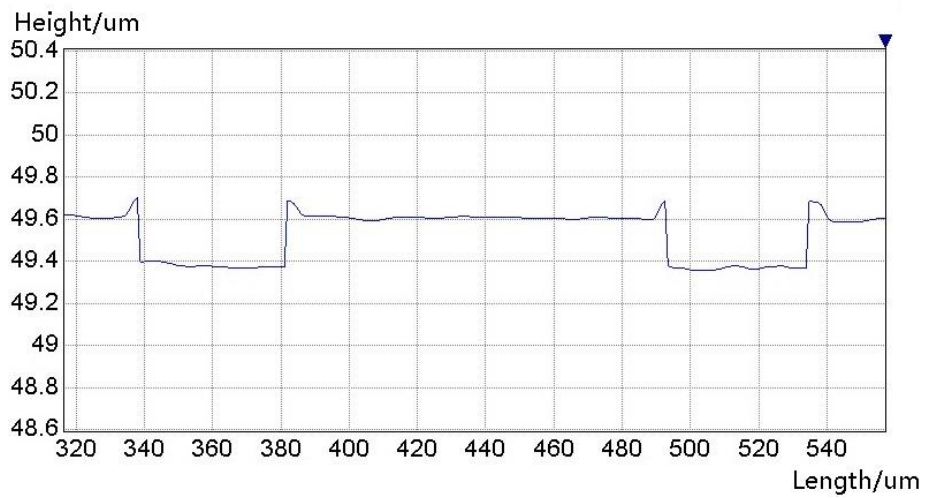
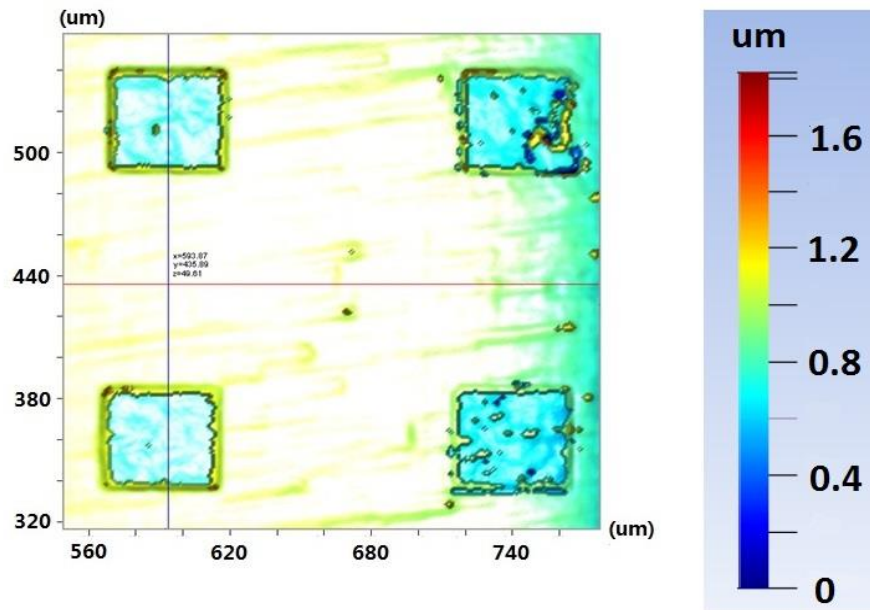
the measurement noise of the system processed by different algorithms. The planar top surface without step-height features is applied to act as a standard flat. The specimen utilised an ultra-smooth quartz photomask blank to assure a very flat and smooth working surface as well as parallelism of the top and bottom surface within a few seconds of arc (VLSI Standards). The estimation of the measurement noise (denoted as  $N_m$ ) is realised with the root mean squared value of the subtraction of two repeated measurements divided by square root of two. The results are illustrated in Figure 6.7. The results indicate that the filter with optimised passband only leads to slight improvement to the performance when the signal quality is high. Also the height estimation through phase algorithm has much lower noise compared to the phase slope method. The results agree with the simulation results very well, the difference is negligible. This chapter focuses on improving the accuracy and stability when the signal quality is not high. Another step-height specimen containing an array of carved squares manufactured by focused ion beam (FIB) in the lab which will be adopted for system calibration in Chapter 7 has been measured with Taylor Hobson CCI 3000 and WSI processed with different algorithms. The results are illustrated in Figure 6.8. As a reference, the CCI result reveals that the depth of the squares is between 200 nm and 400 nm. For example, according to ISO 5436-1, the depth of the top-left square is 248 nm inspected using Taylor Hobson CCI 3000 which features subnanometre accuracy (see Appendix F). The WSI result processed by the phase slope method using the window (2:25) indicates that the depth of the same square is 6.554  $\mu\text{m}$ , which is clearly incorrect but accurately reproduces the large errors forecasted by simulation for the low-quality signal (Figure 6.4(c)). The WSI result processed by the phase slope method with the optimised parameters is 255 nm, which is in close agreement with the CCI result with deviation being within the vertical resolution limit of the WSI. The results processed with height estimation through phase algorithm are omitted here since the results are sunk into the ghost steps because of the low-quality signal, which also accurately agrees with the simulation results (Zhang *et al.*, 2018).

In a practical application, the centre of the effective signal in the Fourier domain is typically the maximum frequency bin excluding the DC component. As a result, an adaptive algorithm which is able to increase the resistance of WSI to noise can be realised based on the pre-acquired LUT mentioned previously once accurate estimation of the SNR of the captured signal can be achieved. As illustrated in Figure 6.9, the signal quality (SNR) is first estimated, and then the selection of phase analysis algorithm and filter parameters is performed in accordance with a lookup table generated by simulation (see Table 6.1).

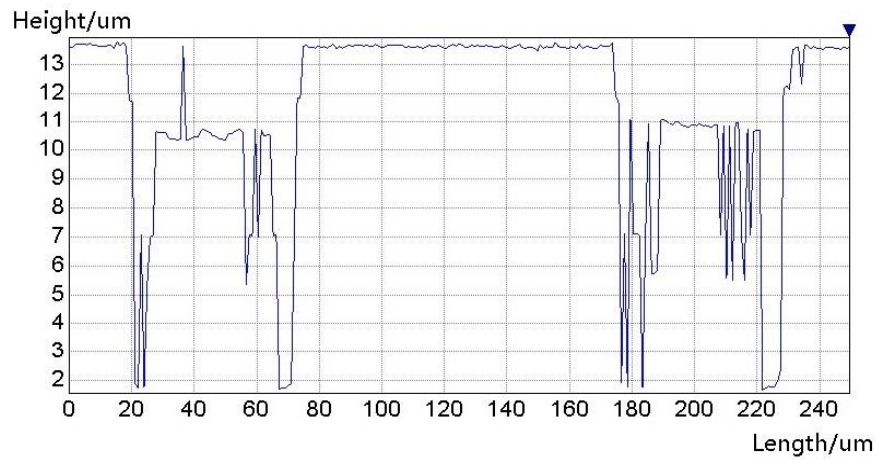
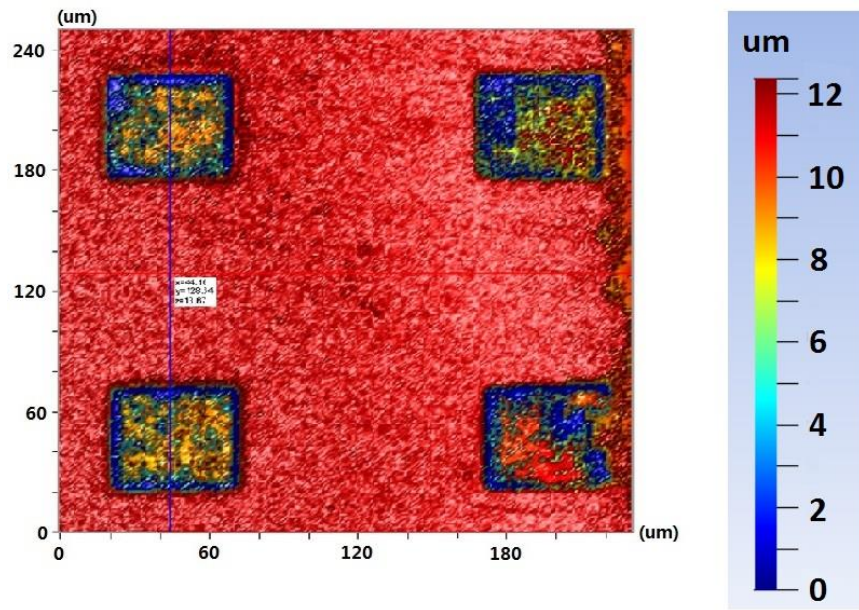
Table 6.1 An example lookup table acquired by the simulation (adapted from Zhang *et al.*, 2018).

SNR of the captured signal	Preferred algorithm*	Half window width
$\text{SNR} \geq 50$	2	13
$50 > \text{SNR} \geq 35$	2	10
$35 > \text{SNR} \geq 25$	2	6
$25 > \text{SNR} \geq 14$	2	3
$14 > \text{SNR} \geq 3$	1	2
$\text{SNR} < 3$	1	1

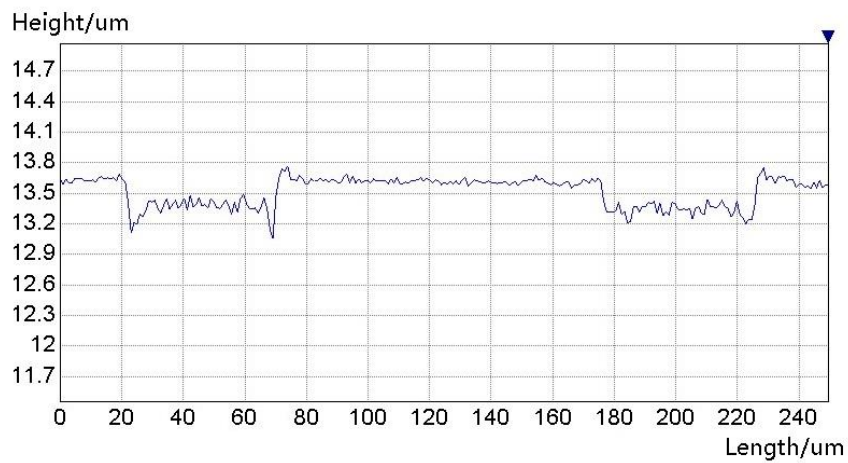
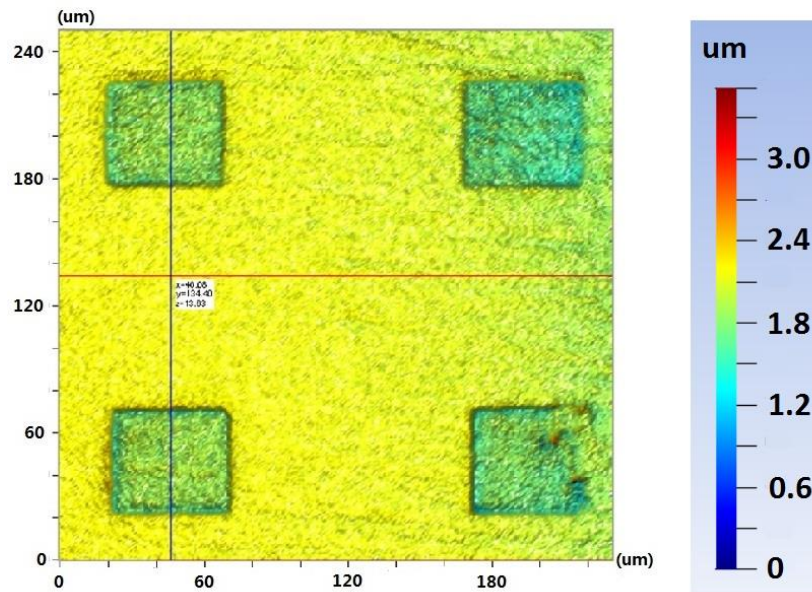
\*Algorithm: 1 denotes phase slope method and 2 means height estimation through phase algorithm.



(a)



(b)



(c)

Figure 6.8 The measurement result of a specimen with different methods (adapted from Zhang *et al.*, 2018).

(a) The result measured with Taylor Hobson CCI 3000.

(b) The result measured with WSI and processed by phase slope method with the window (2:25).

(c) The result measured with WSI and processed by phase slope method with the optimised parameters.

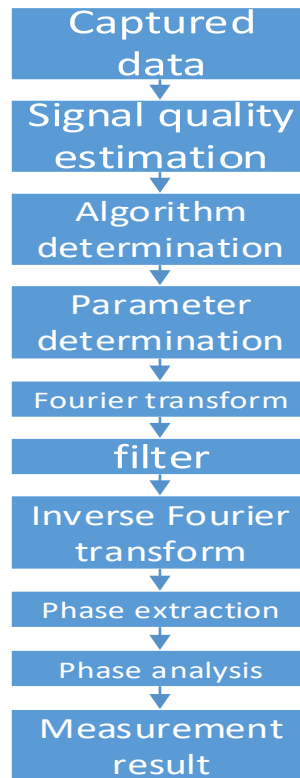


Figure 6.9 An adaptive phase analysis algorithm for wavelength scanning interferometry (adapted from Zhang *et al.*, 2018).

#### 6.4 Vertical calibration for the probes

Both the two probes of the DPWSI have been calibrated using a series of step-height standard specimens. The results show both the two probes have achieved submicrometre scale vertical accuracy. As an example, Figure 6.10 provides the measurement result of a 178 nm step-height specimen manufactured by VLSI standards measured by one of the probes, with only several nanometres deviation. The specimen was measured ten times, the repeatability was 75 nm. It is anticipated that this could be improved to nanometre scale by incorporating the vibration compensation mechanism and increasing the data capturing speed (see Appendix C, the data capturing accounts for ~90% of the deviation, based on that, the vibration compensation mechanism can still improve the repeatability by nearly another 50%). The result of the other probe is similar.

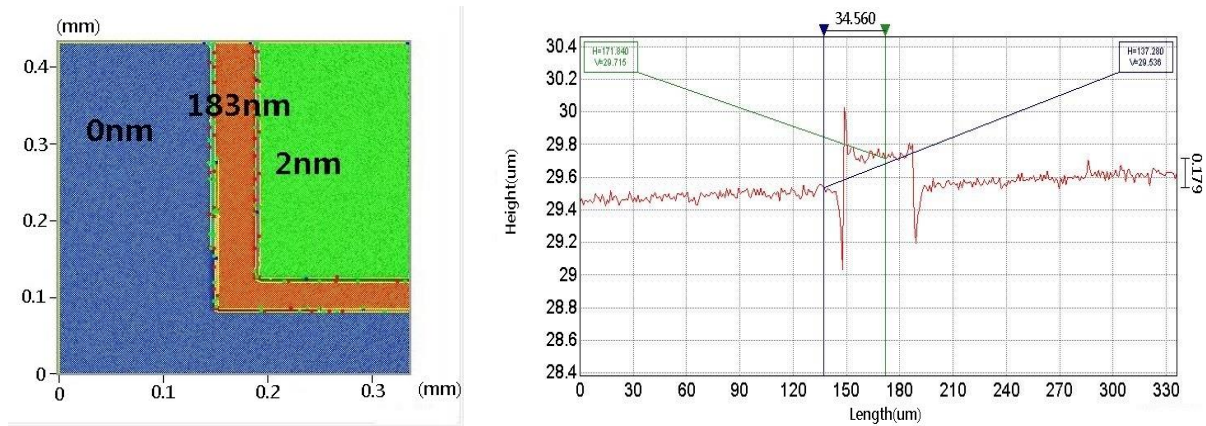


Figure 6.10 The measurement result of a 178 nm standard step-height sample by one of the probes (adapted from Zhang *et al.*, 2017).

## 6.5 Summary

This chapter focused on the fringe analysis algorithms for WSI, optimising the parameters for the filter in order to attain the optimal result. The characteristics of the signal were analysed in both time (wavenumber) and frequency domain. The signal was found to be narrow-band (near single frequency) and the central frequency was calculated theoretically. Consequently, the centre of the passband of the filter was determined. The width of the passband of the filter was optimised with the simulation by compromising between eliminating the noise and the filter ringing. The experimental results were in good agreement with the simulation results, which means, the proposed approach is potentially able to enable WSI to work in a much noisier environment, but this is still not quantified. Finally, the vertical calibration of the probes was accomplished.

To sum up, when the signal has high quality, both the phase slope method and height estimation through phase algorithm have high performance in analysing the fringes and the proposed approach in this chapter only achieves slight improvement. Compared to the phase slope method, height estimation through phase algorithm features much higher performance. However, when the signal quality drops down to a certain level, height estimation through phase algorithm faces serious problems such as ghost steps (Lehmann *et al.*, 2014). But the phase slope method with the optimised parameters is still able to work properly and yield reasonable results with large improvement. The proposed approach reveals the potential of increasing the performance via integrating the two algorithms together according to the signal quality to achieve the optimal results once accurate estimation of the signal SNR can be realised and will be further investigated. The method can also be applied in spectrally resolved white light interferometry (SRWLI) because

the fringe analysis algorithm for SRWLI is similar to WSI (Debnath & Kothiyal, 2006; Zhu & Wang, 2012).

The fringe analysis algorithm achieves the height information for each probe of the DPWSI system. The next chapter discusses the calibration scheme so as to establish the relationship between the two probes to obtain the whole topography of the structured surfaces.

## **7 DPWSI system calibration**

### **7.1 Introduction**

As discussed in Chapter 5, each of the probes of the DPWSI system measures a sidewall of the V-groove structured surfaces, respectively. Then the whole surface topography can be blended on the condition that the relative location of the two interferometers is obtained. The positional relationship between the two probes is built through the spatial coordinate calibration. As there is no overlapping measurable area between the two orthogonally-placed probes, the traditional calibration methods are not applicable. Therefore, some new approach should be devised and adopted. The details are discussed in the following sections in this chapter.

### **7.2 System calibration principle**

As illustrated in Figure 7.1, for each objective, interference is generated between the light reflected from a reference mirror (REF1, REF2) and the light reflected from the measurand. In WSI, a virtual reference plane exists in the measurement path at the point at which the interferometer is balanced. Results obtained from each interferometer yield the distances from the measurand surface to the virtual reference planes (VREF1, VREF2). Because there is no mechanical movement during the measurement process, all the optics are stationary and, thus, the virtual reference planes, VREF1 and VREF2, are nominally static. Therefore, if the relative location of the VREF1 and VREF2 can be established through calibration, then the topography of the sample as measured by the combination of both interferometers can be recovered.

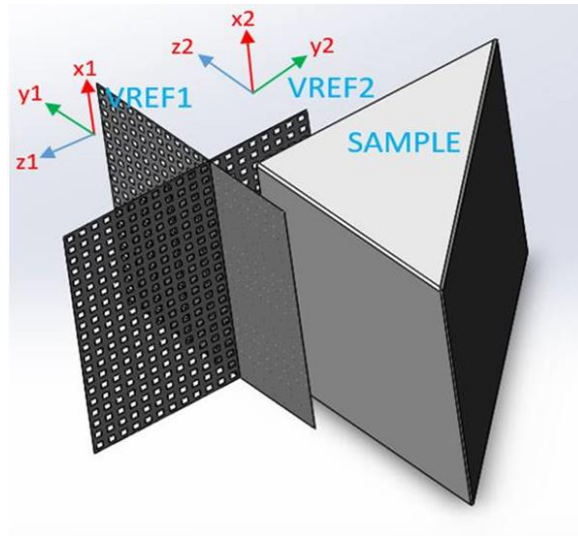


Figure 7.1 The coordinate systems of the probes (adapted from Zhang *et al.*, in-press).

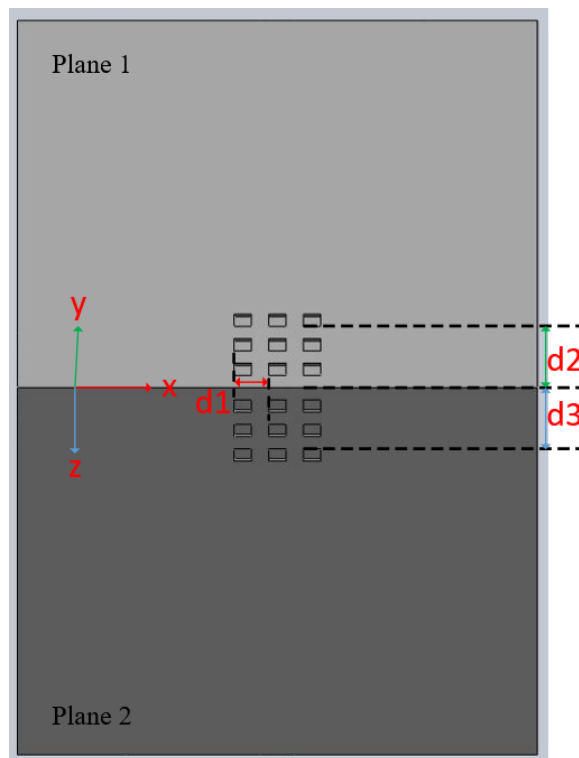


Figure 7.2 A schematic diagram of the calibration artefact with features on two adjoining faces (adapted from Zhang *et al.*, in-press).

The positional relationship between the two probes is built through the spatial coordinate calibration. Because there is no overlapping measurement area between the two orthogonally-placed probes, traditional calibration methods are not applicable. Thus, a custom calibration artefact needs to be designed and manufactured to assist the calibration. Figure 7.2 shows the

design of the calibration artefact, which comprises a precision cube with two adjoining faces (labelled plane 1/2) certified to be perpendicular (see Appendix A, the deviation of the dihedral angle is within 2 arcsec). The features in the measurement results can be extracted with the feature extraction algorithms. If  $P_n$  and  $P'_n$  represent the quaternions of the feature points, such as centres or corners of the features in the reference topography, and  $Q_n$ ,  $Q'_n$  refer to the quaternions of the corresponding feature points in the measurement datasets with the two probes, respectively, the following equations must be satisfied:

$$\begin{pmatrix} R_1 & t_1 \\ 0 & 1 \end{pmatrix} Q'_n = P'_n. \quad (7.1)$$

$$\begin{pmatrix} R_2 & t_2 \\ 0 & 1 \end{pmatrix} Q_n = P_n. \quad (7.2)$$

$$R_n = \begin{pmatrix} 1 & 0 & 0 & 0 \\ 0 & \cos \alpha_n & \sin \alpha_n & 0 \\ 0 & -\sin \alpha_n & \cos \alpha_n & 0 \\ 0 & 0 & 0 & 1 \end{pmatrix} * \begin{pmatrix} \cos \beta_n & 0 & -\sin \beta_n & 0 \\ 0 & 1 & 0 & 0 \\ \sin \beta_n & 0 & \cos \beta_n & 0 \\ 0 & 0 & 0 & 1 \end{pmatrix} * \begin{pmatrix} \cos \gamma_n & \sin \gamma_n & 0 & 0 \\ -\sin \gamma_n & \cos \gamma_n & 0 & 0 \\ 0 & 0 & 1 & 0 \\ 0 & 0 & 0 & 1 \end{pmatrix}. \quad (7.3)$$

$$t_n = (t_{nx} \quad t_{ny} \quad t_{nz}). \quad (7.4)$$

where  $R_1$ ,  $R_2$ ,  $t_1$ ,  $t_2$  represent the rotation matrices and translation matrices from the coordinate systems of the two probes to the reference topography, respectively. These matrices are functions of  $\alpha_n$ ,  $\beta_n$ ,  $\gamma_n$ , which are the respective rotation angles and  $t_{nx}$ ,  $t_{ny}$ ,  $t_{nz}$ , which are the respective translation components along the x, y, and z axes. As such, there are 12 unknown independent variables in total. Theoretically, if there are a sufficient number of feature point pairs, it is possible to precisely determine the matrices. Then the datasets obtained by the two probes can be blended together to acquire the whole topography of the structured surface. The details are discussed in the remainder of this chapter.

### 7.3 Artefact manufacturing

As a result of the dimensions of the manufactured features (micrometre scale), high-precision manufacturing techniques are needed for the fabrication, such as focused ion beam (FIB), micro-milling, and so forth. In this work, a focused ion beam was utilised to achieve the goal.

### 7.3.1 Focused ion beam

Focused ion beam (FIB) is a technology that has widespread applications in material science, microelectronic industry, and finds increasingly wide application in biological research and material ablation for site-specific analysis (Giannuzzi, 2004). FIB apparatus works in a similar fashion to a scanning electron microscope (SEM) with the difference lying in the particle beam. SEM applies a focused beam of electrons for imaging while the FIB instrument makes use of an energetic beam of ions that is operated at low currents for observation or high currents for micromachining. A dual-beam FIB, which incorporates an SEM column to the FIB column, was also developed to enable the investigation of the same object with either of the beams (Uchic *et al.*, 2006).

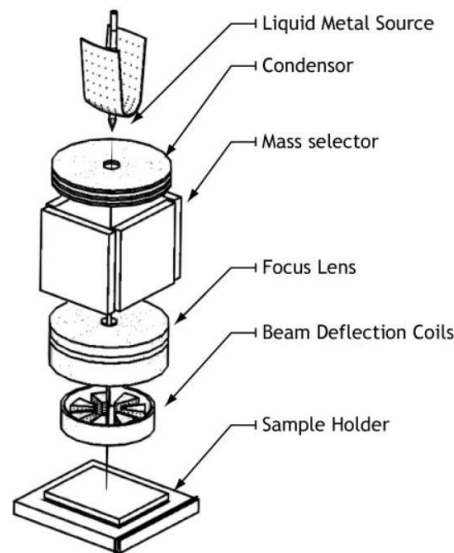


Figure 7.3 A schematic diagram of focused ion beam (adapted from Fibics Inc.).

The main stream of FIB systems employs liquid metal ion sources (LMIS), such as gallium ion sources. The liquid metal is positioned in touch with a tungsten needle and the molten metal wets the needle and flows to the needle tip, where the electrical field and opposing forces of the surface strain drive the atoms of the metal and lead to a cusp-shaped tip, which is termed a Taylor cone. The powerful electrical field (stronger than  $1 \times 10^8$  volts per centimetre) at the small cone tip (the radius is approximately 2 nm) results in ionisation and field emission of the metal atoms (Volkert & Minor, 2007). The generated ions are then focused onto the specimen with electrostatic lenses after being sped up to high energy up to 50 keV (kiloelectronvolts).

As Figure 7.3 shows, the primary ion beam strikes on the specimen surface and sputters some material, which deflects in the form of either atoms or secondary ions, as well as secondary electrons. When the incident ion beam rasters on the specimen surface, the signal carried by the secondary ions or electrons is captured for imaging. When the primary beam current is low, little material is removed and the FIB system can achieve nanometre scale imaging resolution. When applying high primary beam current, numerous materials can be sputtered, enabling ultra-precision milling of the specimen down to sub-micrometre or even nanometre scale (Pellerin *et al.*, 1990). With regard to non-conductive specimens, a flood gun, which is able to steadily produce a flow of low-energy electrons, can be employed for charge neutralisation. In this way, even highly insulating materials can be imaged or milled without a conductive coating by analysing the signal carried by the positive secondary ions (Munroe, 2009).

Commercial FIB products emerged about twenty years ago and found application mainly in large microelectronic manufacturers for device analysis. The applications, such as circuit modification, failure analysis, transmission electron microscope (TEM) cross-sectional sample preparation, and so forth, have become commonplace.

### **7.3.2 Machining of the artefact**

An auxiliary calibration standard artefact with special features is required for the system calibration. At least two adjoining faces should have a very smooth surface finish and high flatness. In addition, the edge between the two faces should be very sharp. The CAD model is as shown in Figure 7.4(a). Very hard material (high-speed steel) was milled into a cube, which was then polished by a slip gauge manufacturer called Opus Metrology. The calibration certificate (Appendix A) shows the artefact is a cube with two adjoining faces perpendicular to each other within two seconds of arc (the actual deviation measured by autocollimator is 1.2 arcseconds). The two faces of the cube have flatness better than 50 nm and roughness ( $S_a$ ) lower than 30 nm. Figure 7.5 is an interferogram of one of the polished faces of the artefact from which the roughness and flatness can be qualitatively judged. Upon each face, an array of 50  $\mu\text{m}$  square wells, having a depth of approximately 200 nm, are then etched using a FIB by MIAMI (abbreviation for Microscopes and Ion Accelerators for Materials Investigation), University of Huddersfield. Both square and circle features have been tested. The result for circles was not as good as squares. As shown in Figure 7.2, restrictions for the 3 axes xyz should be acquired. It is easier to measure a

length parallel to x axis with square features than circle ones because the edges for squares can be used.

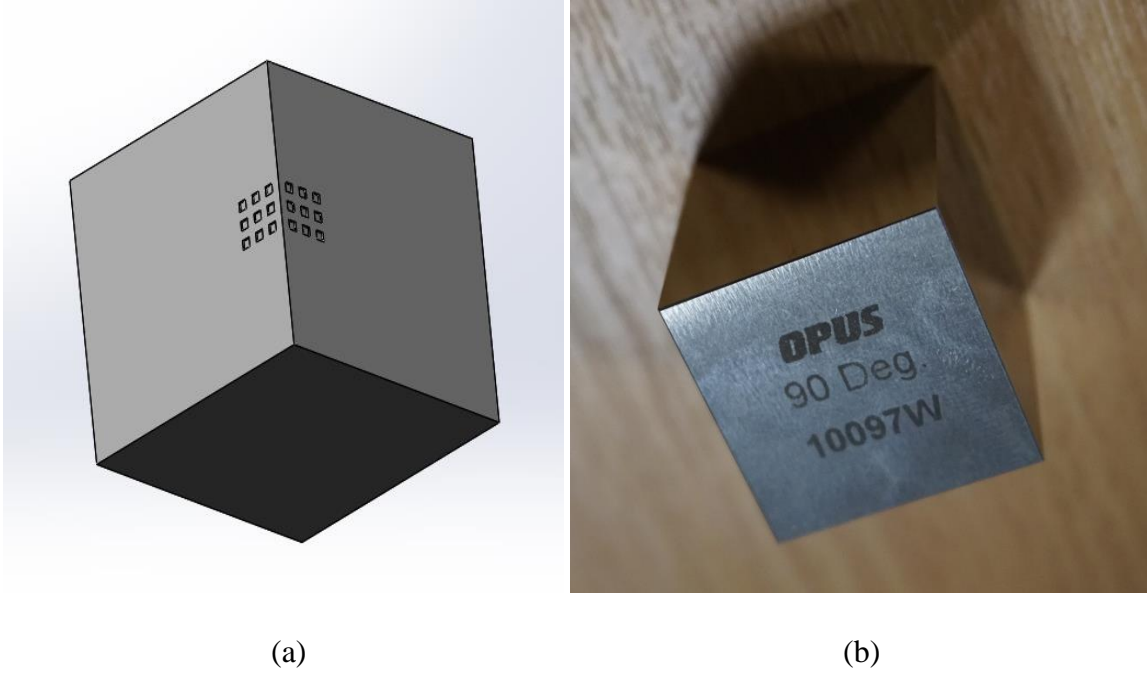


Figure 7.4 The calibration artefact (a). the CAD model and (b). the manufactured item.

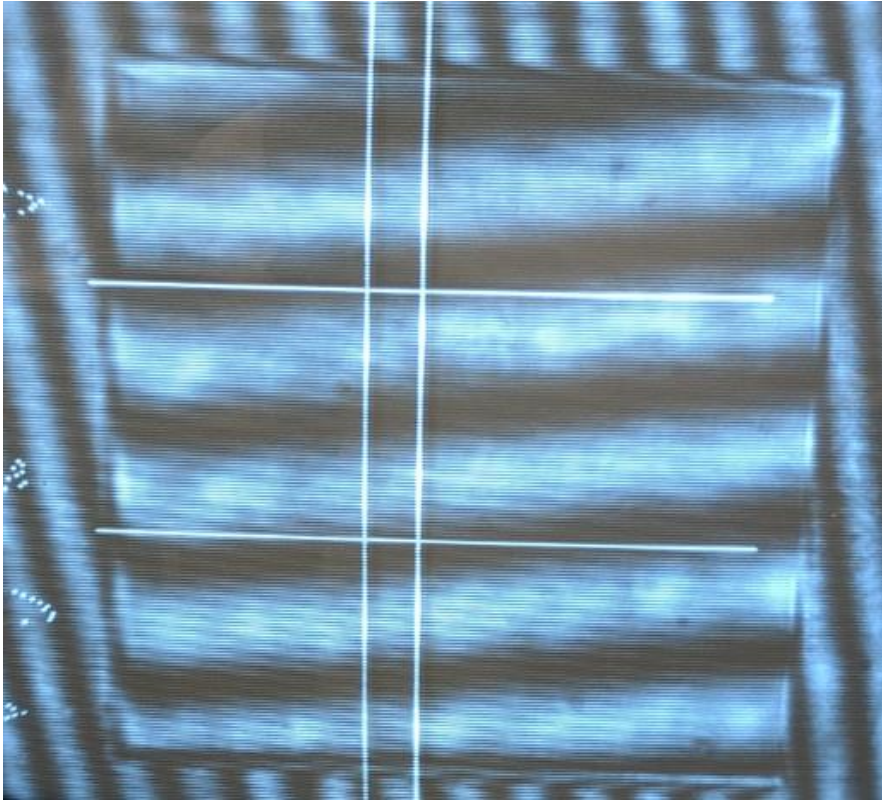


Figure 7.5 An interferogram of one polished face of the machined artefact.

## 7.4 Acquisition of the reference topography

Numerous efforts have been put into acquiring the reference topography of the calibration artefact. To our knowledge, from both the literature and experiment, none of the existing instruments such as Alicona InfiniteFocus, based on focus variation microscopy, or the Keyence 3D laser scanning confocal microscope VK-X250 are able to obtain the topography of the V-shaped structured surface of the artefact with sufficient resolution to detect the features.

The reference topography has finally been achieved by combining the measurement results of a SEM and a coherence scanning interferometer (CSI, Taylor Hobson CCI 3000) together. CSI acquires the topography of the two faces while SEM provides the relative location of the two faces for fusing the datasets.

### 7.4.1 Scanning electron microscopy

A scanning electron microscope (SEM) works by scanning the solid specimen surface with a focused particle beam of electrons to render 3D high-resolution images. The physical principle was proposed by De Broglie early in 1925 (De Broglie, 1925). As illustrated in Figure 7.6, an electron gun at the top of the SEM apparatus generates an energetic electron beam, which is then accelerated and heads down through a vertical path under the vacuum. Electromagnetic lenses control the route of the electron beam while condenser lens adjusts the beam size. Finally, objective lens focuses the electron beam onto the test specimen. Deflection coils are applied for raster scanning the beam onto the specimen (Postek, 1993). When the electron beam comes in contact with the solid specimen surface, it penetrates to a depth of a few micrometres, relying on the acceleration voltage and the specimen density. Most specimens require some preparations before being placed in the vacuum chamber. The most widely adopted preparation processes are sputter coating for non-conductive specimens and dehydration of many biological specimens. The interaction between the electron beam and the atoms in the specimen produces a range of signals, such as backscattered electrons, secondary electrons, and characteristic X-rays containing topographical, morphological, and compositional information about the specimen (Goldstein *et al.*, 2017).

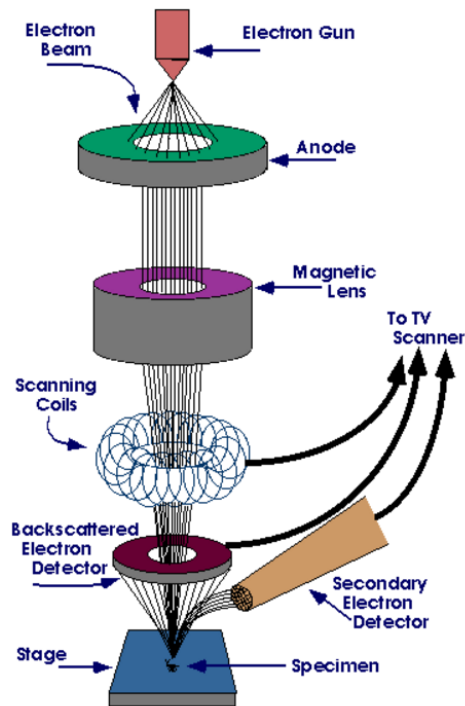


Figure 7.6 A schematic diagram of a scanning electron microscope (adapted from Areef Billah, 2016).

The signals resulting from the electron-specimen interaction are sensed by different types of detectors, such as the secondary electron detector (SED), backscatter electron detector (BSE), diffracted backscatter detector (EBSD), and X-ray detector (EDS) etc. to produce images that are then presented on the computer screen. SEMs have at least one detector and many have additional ones. The capabilities of a specific SEM instrument are highly reliant on what detectors it possesses. The most widely used detector is for sensing secondary electrons emitted by atoms excited by the electron beam. SEM can achieve up to subnanometre resolution. The achievable resolution of an SEM is affected by multiple elements, such as the spot size of the beam and the interaction volume between the electron beam and the specimen.

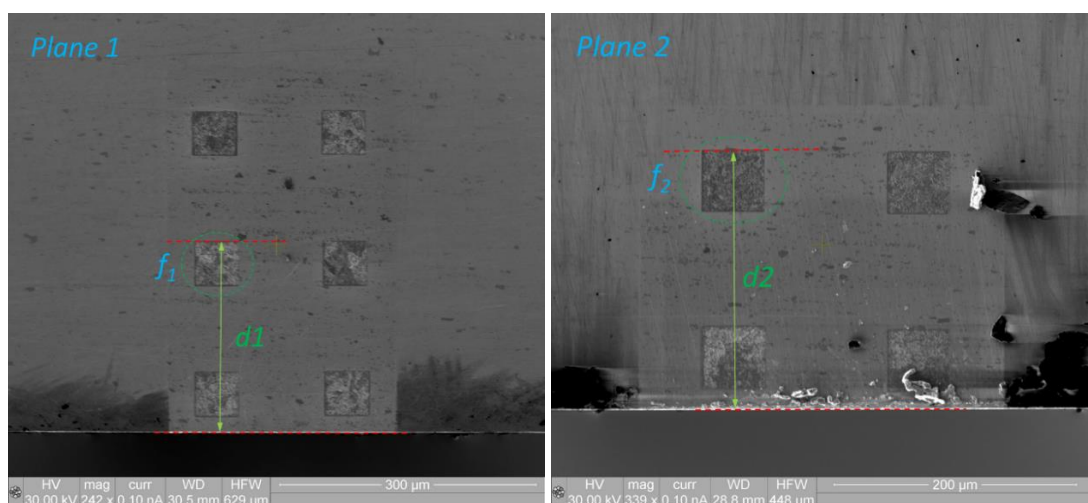
Compared to traditional light microscopes, the SEM has many advantages. Firstly, the SEM has a large depth of field (DOF), which enables more of a specimen to be in focus at a time. In addition, the SEM can have much higher lateral resolution owing to the lower diffraction limit (normally below nanometre). Apart from that, as the SEM adopts electromagnets instead of optical lenses, there is more control over the magnifying power via the raster coils. The weaknesses mainly lie in the necessity for dry and conductive solid specimens owing to the vacuum conditions.

The SEM has a wide variety of applications in many scientific and industrial sectors, especially where the characterisation of solid materials is required. For example, the SEM is widely adopted in determining the crystalline structure, crystal orientations, and chemical compositions. SEMs also find widespread applications in forensic investigations, biological sciences, medical sciences, among others (Buhr *et al.*, 2009; Zhou & Wang, 2007; Smith & Oatley, 1955). Specifically, in metrology, the SEM has built up a standard for critical dimensional metrology (Postek & Joy, 1987). SEMs also find many applications in measuring and verifying structured surfaces.

#### 7.4.2 SEM dataset processing

The SEM has the merits of high lateral resolution and large depth of field, which is very important in the measurement of structured surfaces. The features can be extracted with a 2D image segmentation algorithm from the acquired SEM images and then fitted to determine the distances to aid the fusion of the datasets, as shown in Figure 7.7.

Regarding the feature extraction in SEM images, it is not necessary to utilise every feature as some features might have vague edges in SEM images as a result of the fabrication. Thus, only the ones with clear edges are chosen so the resolution can be guaranteed. As the SEM has a high lateral resolution, this enables the measurement to achieve submicron resolution (Postek, 1993). The edges of the SEM images are extracted with an edge-detection algorithm and are then fitted, combined with the removal of the outliers exceeding three standard deviations. Based on the extracted features, the distances from the features to the edge, and the distance from a feature to another feature can be calculated based on the pixilation. The distances are essential for the latter fusion by providing the relative location of the two faces.



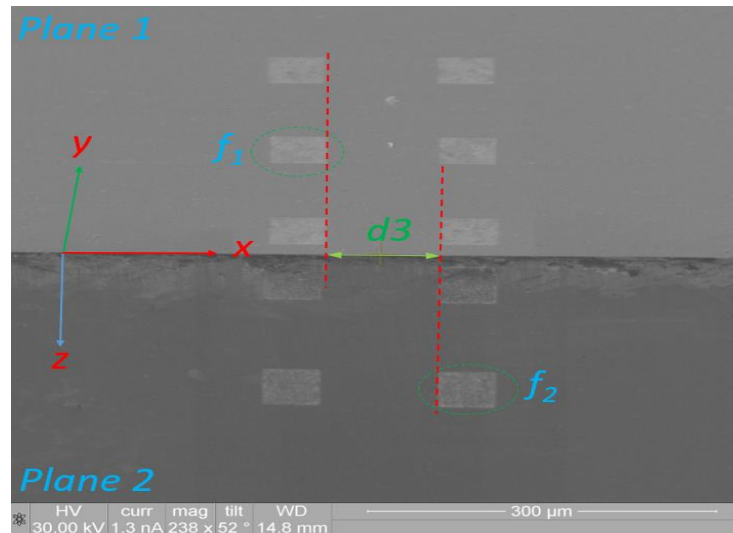


Figure 7.7 The SEM images and the dimensions of the machined artefact (adapted from Zhang *et al.*, in-press).

The edge detection of SEM images can be achieved with a combination of image processing algorithms, such as 2D median filtering, adjustment of image intensity values, morphological opening, etc.

The median filter is a type of nonlinear digital filter that finds wide application in digital image processing (DIP). It is effective at removing noise, especially impulse noise (salt and pepper noise), while preserving edges. Median filters work by going through all the pixels in the image and altering each pixel value into the median value of its adjacent pixels. The pattern of the adjacent pixels is termed as the “window”, which scans each and every pixel within the image (Ismail *et al.*, 2010). For each scan, all the pixel values inside the window are numerically sorted first and then the middle value of the pixel values inside the window is applied for the pixel.

After removing the noise, image intensity values are adjusted to increase the contrast. The adjustment saturates the top and bottom part of all pixel values. In other words, it expands the distribution range of the pixel values using the Otsu method (Liu & Yu, 2009). Then the grayscale image is converted into binary image based on a global threshold.

Morphological opening is the dilation of the erosion of a set A by a structuring element B, as shown in Eq. (7.5).

$$A \circ B = (A \ominus B) \oplus B \quad (7.5)$$

where  $!$  and  $\oplus$  represent erosion and dilation, respectively. Morphological opening is a functional unit of morphological noise elimination. It removes small objects from the foreground of an image and put them in the background (Vincent, 1994).

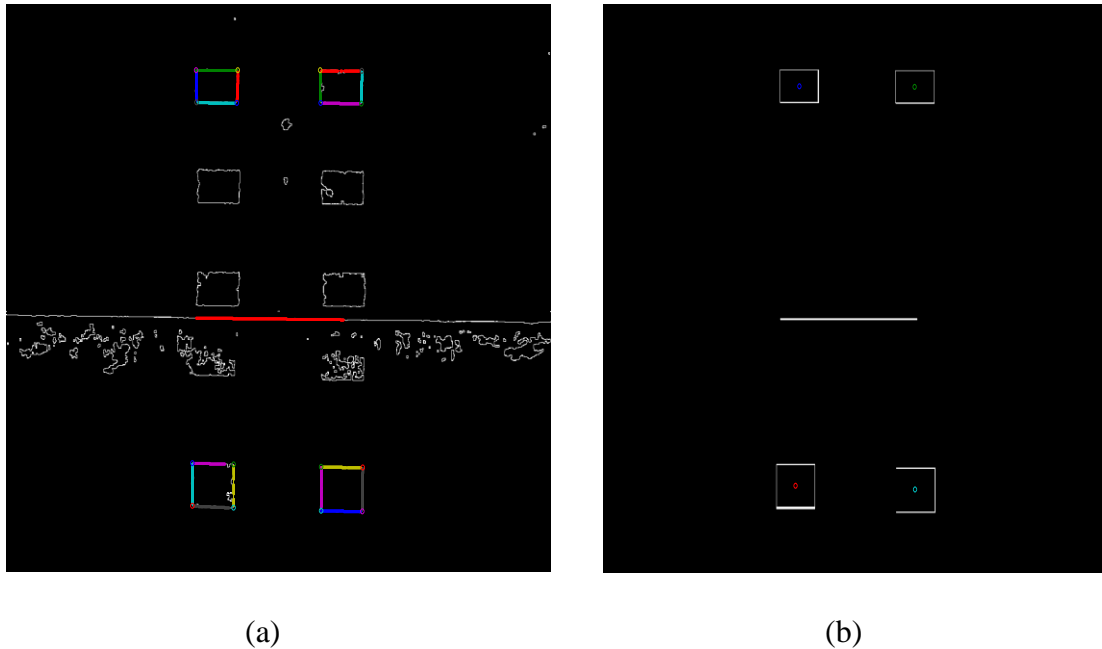


Figure 7.8 (a). the extracted edges of the selected features; (b). the fitted edges of the features after outlier removal.

The extracted features are fitted and the points exceeding three standard deviations are considered to be outliers and would be discarded, as illustrated in Figure 7.8. The distances from the features to the edge and the distance from a feature to another feature are determined based on the fitted results. As a result of the acceptable angle issue limited by the NA of the interference objective, CSI cannot acquire the topography data near the ridge of the calibration artefact, which makes accurately determining the distances from the features to the edge essential in stitching the reference topography.

### 7.4.3 Topography dataset processing

The topography of the two faces was measured using a traditional instrument, namely CSI (Taylor Hobson CCI 3000), which features very high resolution (sub-nanometre vertical resolution, micrometre level lateral resolution). The edges of the features (the ones selected for SEM images) were extracted correspondingly for determining the relative location during the fusion.

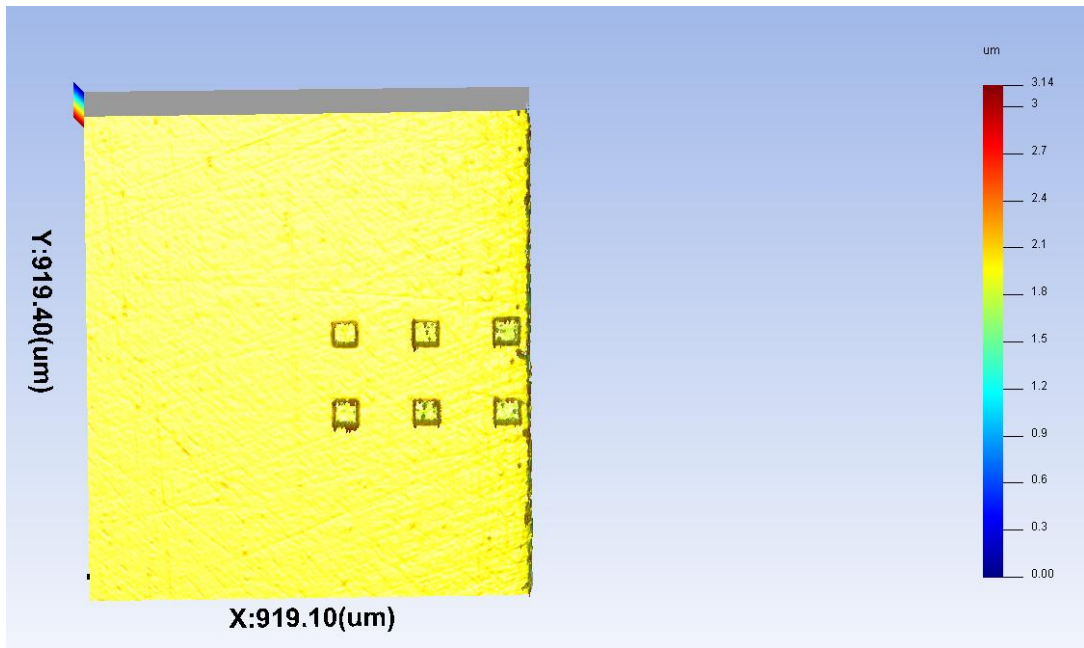
The 3D edge detection algorithm is implemented with the Sobel operator associated with watershed transformation with fine adjustment of the parameters. The Sobel operator, also known as Sobel filter or Sobel-Feldman operator (Sobel & Feldman, 1968), is widely adopted in image processing fields such as machine vision, autonomous navigation, etc., specifically for the applications involving edge-detection algorithms where it generates a new image highlighting the edges. The operator is named in remembrance of Irwin Sobel and Gary Feldman, who worked together in the Stanford Artificial Intelligence Laboratory (SAIL). They proposed the approach at a talk in SAIL in 1968. The operator employs two  $3 \times 3$  kernels, which convolves with the image under processing to approximate the partial derivatives—one for the horizontal variation rate and the other for the vertical. The operations are as shown in Eq. (7.6):

$$G_x = \begin{pmatrix} 1 & 0 & -1 \\ 2 & 0 & -2 \\ 1 & 0 & -1 \end{pmatrix} * A \quad \text{and} \quad G_y = \begin{pmatrix} 1 & 2 & 1 \\ 0 & 0 & 0 \\ -1 & -2 & -1 \end{pmatrix} * A \quad (7.6)$$

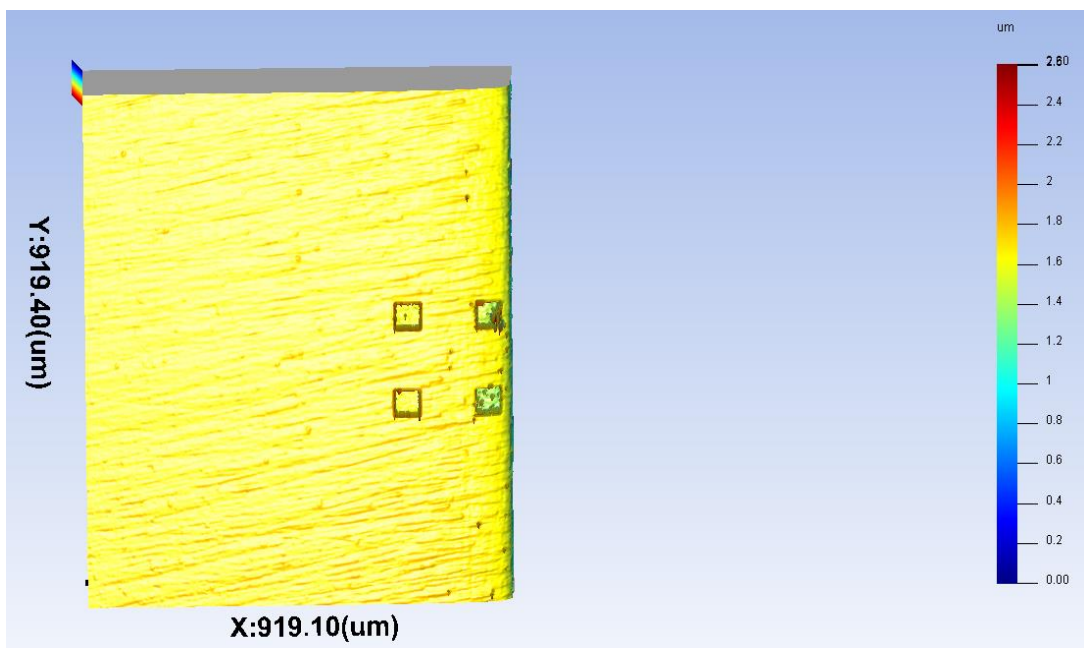
where  $A$  denotes the source image,  $G_x$ ,  $G_y$  refer to the images that contain the horizontal and vertical derivative or gradient approximations at each point, respectively, and  $*$  represents the 2D convolution operation. Then the image gradient magnitude, which highlights the edges, is calculated.

Watershed is a transformation for grayscale images, which represents a metaphor for a geological item, namely a divide that separates two neighbouring catchment basins. It processes the image in a similar way to topography, with the grayscale value of each pixel representing the height and searches for the lines going along the peaks of ridges (Beucher & Meyer, 1992). Therefore, it is suitable for processing the topographic data acquired by CSI.

Watershed transformation is typically used in image processing for segmentation. It is applied to the image gradient and extracts the watershed lines dividing the homogeneous areas, yielding the required segmentation result.

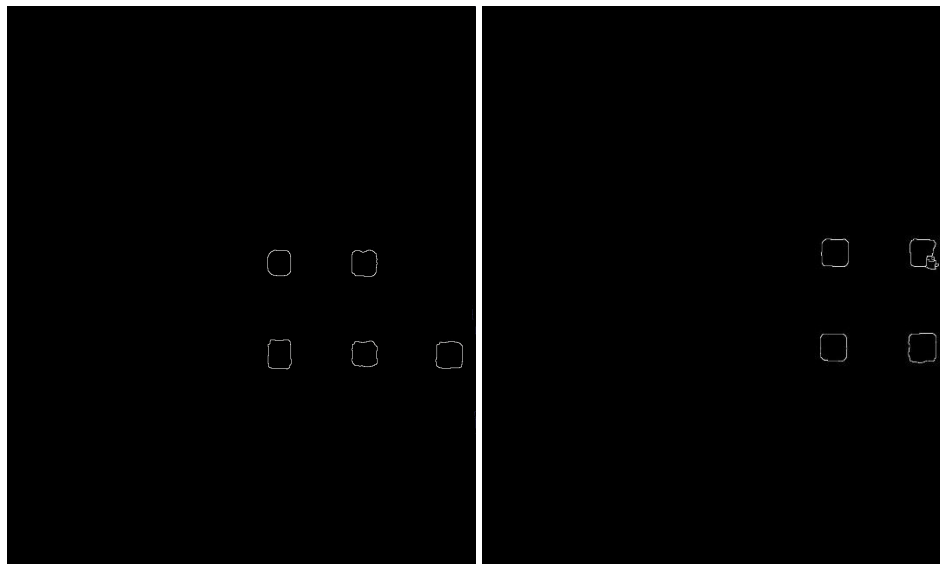


(a). Plane 1



(b). Plane 2

Figure 7.9 The measurement result of the two faces using Taylor Hobson CCI 3000.



(a). Plane 1

(b). Plane 2

Figure 7.10 The extracted edges of the distinctive features.

The extracted edges of the features are then fitted using the same fitting method as the SEM images. Figure 7.9 shows the obtained topography with CSI and Figure 7.10 is the extracted edges of the distinctive features with the indistinctive features discarded. The spike error, such as batwing near the edges, is quite serious in the measured results and is a threat for accurately extracting the edges. Therefore, the outlier filtering algorithm is applied before extracting the edges, as discussed in Section 7.4.4.

#### 7.4.4 Outlier filtration

Spike errors such as batwing are commonplace in interferometry, irrespective of PSI, CSI, WSI, or other types (Le Goïc *et al.*, 2012). A wide variety of filters can be applied to remove these outliers.

##### 1) Gaussian filter

A Gaussian filter is a type of linear filter that is widely applied in surface metrology for eliminating high-frequency noise. It convolves the measurement result with a Gaussian function whose shape is defined by the parameter of the cut-off wavelength. During the process, a weighted average of the neighbouring data points is calculated based on the Gaussian kernel, which features a bell shape. In other words, it takes larger weights for the central part and lower weights for the two ends. When there are outliers in the measurement dataset, the linear Gaussian filter cannot discern

the outliers from the inliers. Therefore, the filtration outcome is distorted by the outliers, especially for the areas where outliers take high proportion. As a consequence, a robust Gaussian filter was presented to be able to improve the resistance to outliers. Robust statistical estimates, such as the Tukey estimate, are integrated into the filtration process, functioning as a vertical weighted average and an extension to the lateral weighting (Seewig, 2005).

A linear Gaussian filter features high performance in processing stochastic surfaces while the robust Gaussian filter does well in the suppression of outliers. However, Gaussian filters are not good at handling structured surfaces, which encompass functional features incorporated with steep geometrical edges. When Gaussian filters are applied to the edges of geometrical features, the edges of geometrical features would become blurred owing to the averaging characteristics (Seewig, 2005).

## 2) Median filter

As mentioned in Section 7.4.2, median filters do well in removing salt-and-pepper noises or speckle outliers from images. However, they are likely to fail when applied to datasets with lumped outliers because these outliers can lead to biased medians. Ismail *et al.* reported an optimised median filter for which the outliers are detected in accordance with the difference between the medium value of the adjacent data within a well-defined window and the measurement data (Ismail *et al.*, 2010). The initial side length of the detection window is determined by the size of the largest outlier cluster in the measurement dataset and can be increased iteratively by a step of two if necessary. The median filter performs well in eliminating impulse noise, with the advantage of edge-preserving, especially for applications with small speckle patterns (Ruiz & Kaufmann, 1998). However, the median filter is weak in terms of processing non-impulse noise and it has been reported that it does not suit surfaces comprising adjoining outlier clusters (Wang *et al.*, 2018).

## 3) Morphological filters

A morphological filter is a type of nonlinear filter that is employed for eliminating outliers in the measurement dataset. In mathematical morphology, closing is applied in eliminating small holes while opening is employed to suppress small objects such as spikes, both via scanning a spherical or planar structuring element through the measurement dataset (Lou *et al.*, 2013a). Podulka *et al.* showed an example of applying a morphological closing filter that employs two 2D structuring

elements with different sizes to search for the spikes on a profile of a cylinder liner (Podulka *et al.*, 2014).

As the outcome of morphological filtration is dependent on the local geometry of the measured surface and the shape of the structuring element, morphological filters have advantages over the linear Gaussian filter in preserving critical surface features. However, when applying morphological filters on structured surfaces, the size of the structuring element, e.g. the radius of a spherical structuring element, is affected by the geometry of the small features on the surface. Therefore, the outliers are suppressed while preserving the edges of surface features in the meantime. Another issue with morphological filters is they are more computation-intensive compared to Gaussian filters. Therefore, morphological filters can be too slow for large measurement datasets (Lou *et al.*, 2013b).

#### 4) Clustering filter

##### 4.1 Basic principle

The clustering filter first presented by Wong (Wong, 1993; Wong, 1995) is typically employed for noise elimination and suppression of outliers for optically attained surface topography. The clustering filter is a technique for separating an obtained dataset into a number of smaller groups. The clustering is dependent on the scaling. At the coarsest scale, the whole dataset can be treated as a single cluster; at the finest scale, each sample in the dataset is taken as a cluster. The clustering filtration between the coarsest scale and the finest scale is essentially a decomposition in the scale space and is in agreement with the physically melting process.

The centre of a dataset is determined by maximising the data entropy complying with a linear cost restriction. Provided there is a 2D dataset  $\{(x_i, z_i) : i = 1, \dots, n\}$ , where  $z_i$  refers to the height value of the profile at the lateral position  $x_i$ . Suppose  $\{x, z\}$  is the centre of the cluster, the cost functions of each  $x_i$  and  $z_i$  are  $e_x(x_i) = \|x - x_i\|^2$  and  $e_z(z_i) = \|z - z_i\|^2$ , respectively, where  $\|\cdot\|^2$  represents the square of Euclidean distance. Let  $P_i$  denote the distribution of  $(x_i, z_i)$  surrounding

the cluster centre  $\{x, z\}$ , maximising the entropy  $S = -\sum_i P_i \log P_i$  while abiding by the two linear constraints  $\sum_i P_i e_x(x_i) = C_x$  and  $\sum_i P_i e_z(z_i) = C_z$  results in the following equation (Wong, 1993):

$$y = \frac{\sum_i y_i \omega_i e^{-\beta(z_i - z)^2}}{\sum_i \omega_i e^{-\beta(z_i - z)^2}}. \quad (7.7)$$

where  $\omega_i = e^{-\alpha \|x_i - x\|^2}$ .

Eq. (7.7) yields the cluster centre in height in the form of the weighted average. Eq. (7.7) is similar to scale-space filtration. The clustering filter performs this operation for each and every sample in the dataset.

#### 4.2 Algorithm for clustering filtration

The algorithm for clustering filtration is schematically illustrated in Figure 7.11. The algorithm starts by inputting the initial value of parameter  $\alpha$  such that the samples within the region of interest that contribute to the location of the cluster centre can be targeted. The initial estimate of the cluster centre  $z_i$  is produced according to Eq. (7.7). The parameter  $\beta$  applied in the equation

is initially set to  $\beta = \frac{1}{2\sigma_z^2}$ , where  $\sigma_z$  is a measure of local variance given by  $\sigma_z^2 = \frac{\sum_i (z_i - \bar{z})^2 \omega_i}{\sum_i \omega_i}$ ,

and  $\bar{z}$  is a measure of local average defined as  $\bar{z} = \frac{\sum_i z_i \omega_i}{\sum_i \omega_i}$ . Then, iterations of Eq. (7.7) lead to

Eq. (7.8), which always converges. In each iteration, the cluster centre  $z$  is updated, and  $\beta$  is also refreshed in accordance. In practice, a small tolerance with sufficient precision is set for the termination of the iteration process.

$$z^{(t+1)} = \frac{\sum_i z_i \omega_i e^{-\beta^{(t)}(z^{(t)} - z_i)^2}}{\sum_i \omega_i e^{-\beta^{(t)}(z^{(t)} - z_i)^2}}. \quad (7.8)$$

The same procedure is exhaustively applied to each and every sample of the attained dataset. The outcomes, namely the cluster centres  $(x, z)$ , are then adopted as the dataset after filtration.

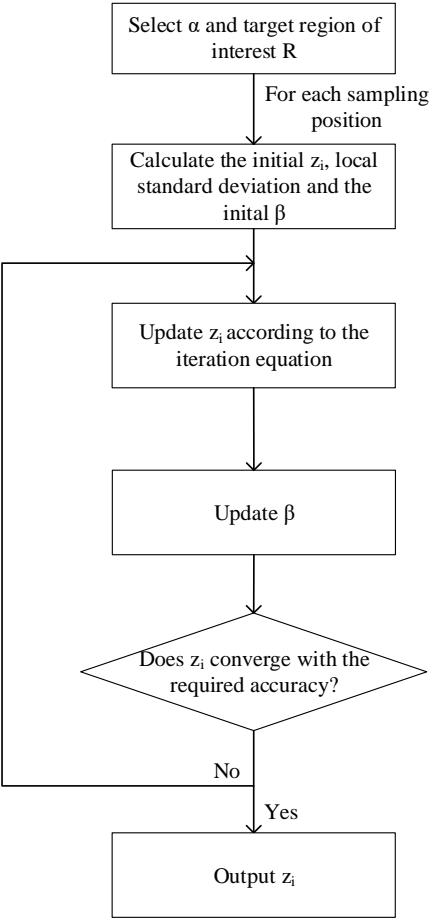


Figure 7.11 The flow chart of the procedure for clustering filtering.

**7.4.5 Surface fitting**

The measurement results of the two adjoining faces were fitted into planes to calculate the dihedral angle between the two faces. Each plane could be represented by the normal vector and a point in the plane. The normal vectors of the two planes were applied for calculating the dihedral angle between the two faces when fusing the two faces.

The surface fitting can be achieved by calculating the normal vector and a point on the plane. The point can be acquired by taking the centroid while the normal vector can be achieved by using singular value decomposition (SVD) to calculate the singular vector corresponding to the lowest singular value. This can be numerically implemented by calculating the smallest eigenvector of the covariance matrix of the measurement results. By comparing the fitted plane and the original

measurement result, the deviation of the measurement result compared to the fitted plane is found to be very low, which agrees with the result of the flatness measurement (better than 50 nm).

#### 7.4.6 Reference topography blending

After filtering the spike errors with a clustering filter, the reference topography was obtained through fusing the datasets acquired with CSI (Taylor Hobson CCI 3000) and an SEM (FEI Quanta 200 3D SEM-FIB), using the approach illustrated in Figure 7.2. The topographies of the areas containing the features on the two adjoining faces (illustrated by the two rectangles in Figure 7.2) measured by CSI are blended with the guidance of the relative location between the two faces (the distances  $d_1$ ,  $d_2$  and  $d_3$  in three different directions, as shown in Figure 7.7) measured by SEM. Then the two adjoining faces are fitted and the surface normal vectors are obtained for calculating the dihedral angle between the two faces. Since the dihedral angle between the two planes is already known, the topography can be reconstructed by blending the data together based on the coordinate system shown in Figure 7.7 with the following restrictions:

$$\begin{cases} distance(f_1, p_2) = d_1 \\ distance(f_2, p_1) = d_2 \\ distance(f_1, f_2) = d_3 \end{cases} \quad (7.9)$$

where  $P_n$  represents the fitted plane of face  $n=1$  or  $2$ ,  $f_m$  refers to the selected feature,  $m=1$  or  $2$ . The fusion can be accomplished by keeping the data of one face still, and rotating and translating the other face until these restrictions are satisfied using only rigid transformations. Figure 7.12 illustrates the blended result plotted with CloudCompare.

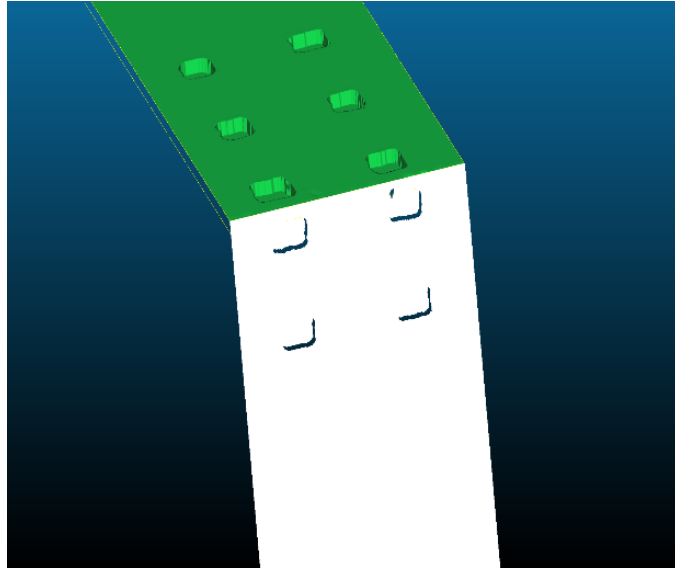
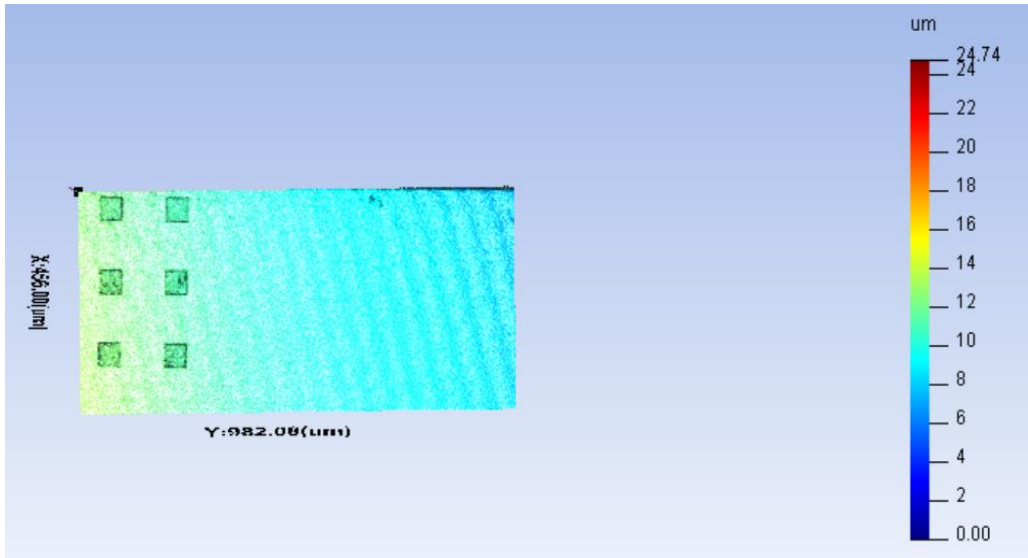


Figure 7.12 The reconstructed surface topography of the calibration artefact plotted with CloudCompare (adapted from Zhang *et al.*, in-press).

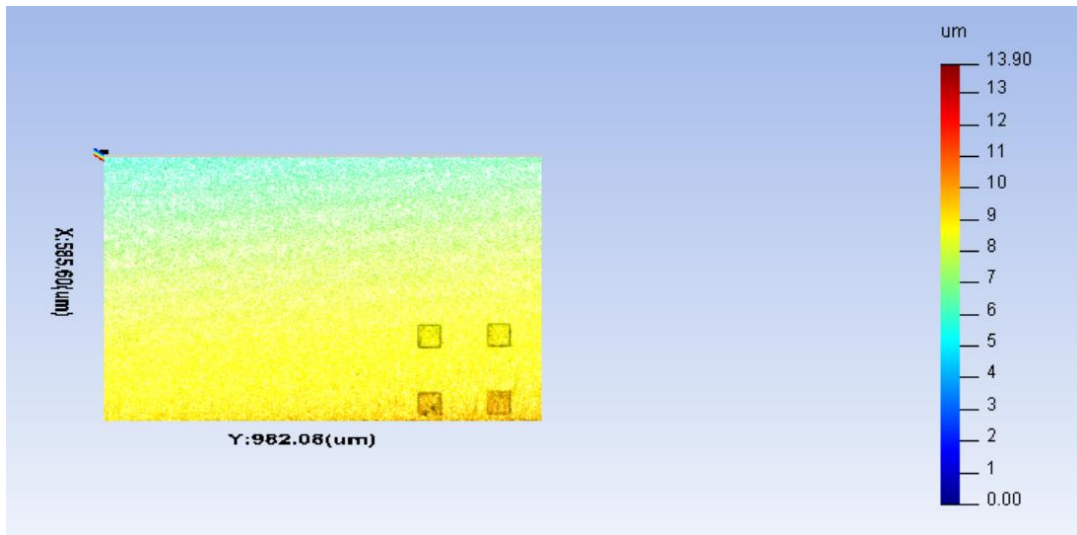
### 7.5 Measurement results with DPWSI probes

After obtaining the reference topography, the calibration artefact was measured by the DPWSI system. The measurement results were then registered to the reference topography to achieve the relative location between the two probes of the DPWSI system.

The calibration artefact was measured using DPWSI. The result is shown in Figure 7.13. The distinctive features were extracted correspondingly for the stitching, as illustrated in Figure 7.14. As can be seen in Figure 7.13, DPWSI has even more serious spike errors than the CSI results. Therefore, the outlier filtration method, namely a clustering filter discussed in Section 7.4.4 was also applied for the DPWSI results before extracting the distinctive edges. The edge extraction algorithm was the same as the one used for extracting the edges for the topography measured by CSI.

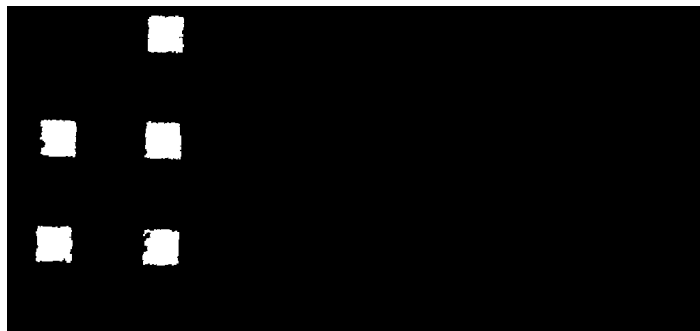


(a). Plane 1 by probe 1

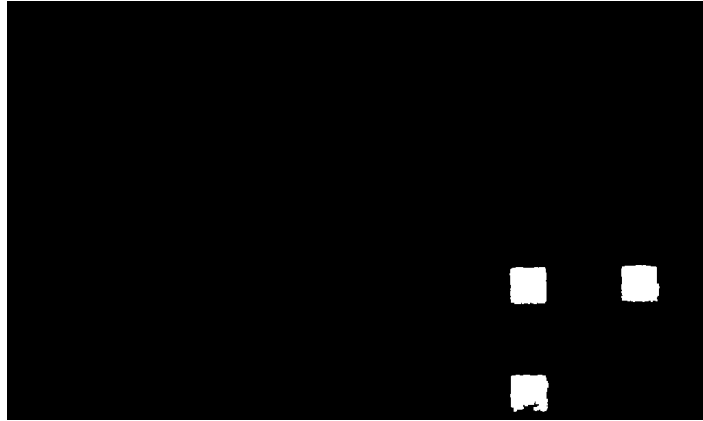


(b). Plane 2 by probe 2

Figure 7.13 The measurement result of the two faces using DPWSI.



(a). Plane 1



(b). Plane 2

Figure 7.14 The extracted edges of the distinctive features.

## 7.6 3D registration

The DPWSI system calibration employs a 3D registration algorithm, specifically an iterative closest points (ICP) algorithm, to acquire the relative location of the two probes. This section reviews the algorithms and then discusses the system calibration.

### 7.6.1 Overview

Image registration is a process that overlays different datasets into one coordinate system. 3D registration deals with 3D datasets that can be from different viewpoints, times, sensors etc. It finds wide application in medical imaging, robotics, augmented reality, military automatic target recognition, computer vision, aerospace, etc. (Goshtasby, 2005). Generally speaking, the applications can be classified into four types based on the means of data acquisition (Zitova & Flusser, 2003):

- Multiple viewpoints. Datasets of the same scene are captured from several viewpoints to gain a larger representation of the scene.
- Different acquisition times. Datasets of the same scene are captured at different times, typically on a regular basis and probably under different circumstances, aiming to find and evaluate variations between two consecutive frames of the scene.
- Multiple sensors or multimodal analysis. Datasets acquisitions of the same scene are performed by different sensors with the purpose of merging the acquired information to get a more thorough understanding.

- Reality to model comparison. Registration between datasets of a scene and model of the scene are performed. The model is a numerical representation of the scene, such as maps, another similar scene, etc. The goal is for locating the obtained image in the model and to compare them.

3D registration is essential for comparing or merging the datasets acquired with different measurements. One dataset is called the reference and others are referred to as the target or sensed datasets. 3D registration performs spatial transformations to the sensed datasets to match the reference dataset, which is kept stationary.

3D registration algorithms can be categorised into rigid and non-rigid registration with respect to the transformation models adopted to match the sensed datasets to the reference dataset. Only linear transformations, including rotation, scaling, translation, and other affine transforms are applied in rigid registration and the transformations are global. Therefore, rigid registration is not able to model local alterations. Non-rigid registration allows for elastic transformations that are able to locally alter the sensed datasets to align with the reference dataset. Elastic transformations, such as large deformation models, radial basis functions, etc. can be performed. For example, medical image registration often requires elastic registration to deal with deformation of the organs as a result of structural variations, breathing, and so forth (Goshtasby, 2005).

According to the means of data acquisition, 3D registration algorithms can be grouped into single-modal and multi-modal methods. Single-modal algorithms register datasets acquired by the same type of sensors while multi-modal registration methods deal with datasets achieved by different sensor types. Multi-modal algorithms are often applied in medical imaging because data of a scene is frequently captured by different sensors (Zitova & Flusser, 2003) —for example, the registration of PET/CT datasets of a whole body for localising tumours and registering ultrasonic and CT data for locating prostates in radiotherapy.

Registration algorithms can also be classified in accordance with the automation level into manual, interactive, and automatic methods. Manual approaches provide a means of aligning the datasets manually. Interactive algorithms cut off some user interventions by carrying out part of the operations automatically but are still reliant on the user to monitor and control the registration process. Automatic methods require no user intervention and perform the whole process automatically (Goshtasby, 2005).

There are four important components for the registration algorithms:

1. Feature set, which is the extracted information in the datasets applied for alignment.
2. Transformation space, which is the type of transformation that can match the datasets;
3. Search scheme, which selects the next transformation in the iterations searching for the optimised transformation;
4. Similarity measure, which determines the relative quality for each iteration.

Although many constituent elements are diverse, the main stream of the registration algorithms can be decomposed into the steps described below (Zitova & Flusser, 2003):

1. Feature recognition. Distinctive features, such as enclosed regions, boundaries, corners, etc. are identified. The features are then denoted by the point representatives, e.g., gravity centres, endpoints of line sections, etc., which are also known as control points (CPs).
2. Feature aligning. The corresponding relationship between the features in the target datasets and the ones identified in the reference dataset is built up. A number of feature descriptors and similarity metrics associated with relative locations between the features are applied to achieve the goal.
3. Estimation of transformation model. The estimation of the types of the mapping functions, together with the related parameters required for matching the sensed datasets to the reference dataset, are performed. The required parameters for the mapping functions are determined based on the built-up corresponding relationship between the features.
4. Dataset resampling and transformation. Transformations based on the mapping functions are applied to the sensed datasets for registering the datasets.

Some commonly used 3D registration algorithms include principal component analysis (PCA), singular value decomposition (SVD), iterative closest point (ICP) and its variants, and so forth (Bellekens *et al.*, 2014). In this study, only rigid 3D registration is required. Therefore, this chapter mainly focuses on iterative closest point algorithm, which is widely adopted in this area.

### **7.6.2 Iterative closest points (ICP) algorithm**

Iterative closest points, also known as iterative corresponding points algorithm, which is a registration algorithm used to minimise the difference between two sets of points, finds wide application in the reconstruction of 2D or 3D surfaces from multiple scans. During the matching process, the reference dataset is kept stationary, while the source dataset is transformed to achieve

the best alignment with the reference. ICP repeatedly reforms the transformation, namely a blend of rotation and translation desired to reduce the error metric, typically the distance between the sensed point sets and the reference point set, e.g. the sum of the square of the deviations between the coordinates of the point pairs successfully matched. Initial estimation of the transformation between the datasets is essential before using ICP for aligning the 3D models.

Besl and McKay introduced the ICP algorithm to improve the estimation of the transformation parameters (Besl & McKay, 1992). As illustrated in Figure 7.15, the input to the ICP algorithm comprises a reference point set and a sensed point set. Corresponding relationships between the point sets are built up with a specific scheme, such as the nearest neighbour method. Singular value decomposition (SVD) is applied to estimate the transformation matrix, which matches the two point sets. The whole procedure is iterated by eliminating outliers and rebuilding the corresponding relationships.

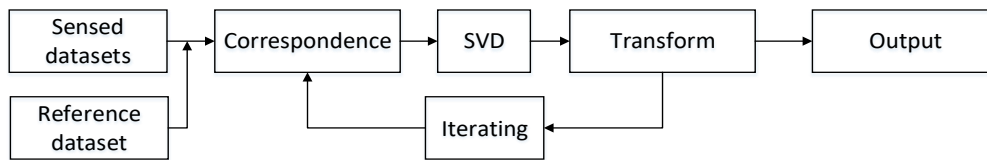


Figure 7.15 The flow chart of the ICP process.

There are many algorithms derived from ICP, among which point-to-point and point-to-surface are most widely used (Bellekens *et al.*, 2014).

ICP point-to-point finds point counterparts in the reference point set, via the search for the nearest point  $q_i$  of a point  $p_j$ , which is in the sensed point set. The search for the nearest point is performed based on the measure of Euclidean distance as shown in Eq. (7.10).

$$\hat{i} = \arg \min_i \|q_i - p_j\|^2. \quad (7.10)$$

where  $i \in [0, 1, \dots, N]$ , and  $N$  refers to the number of points in the reference dataset.

The transformation, i.e., the rotation  $R$  and translation  $t$  parameters are calculated via minimising the squared Euclidean distance between the corresponding pairs:

$$R, \hat{t} = \arg \min_{R, t} \sum_{i=1}^N \left\| (Rp_i + t) - q_{pi} \right\|. \quad (7.11)$$

where  $p_i$  refers to a point in the sensed point set,  $q_{pi}$  represents its corresponding point in the reference dataset. The algorithm then repeats this process to improve the estimation.

ICP point-to-point algorithm is vulnerable to outliers. To overcome this shortcoming, the ICP point-to-surface algorithm is proposed. By taking a local neighbourhood of a corresponding point into consideration, the algorithm's resistance to noise is increased. The ICP point-to-surface algorithm presumes that the point sets are locally linear. Thus, the nearest neighbours of a point are co-planar. The local surface is then represented by the normal vector  $\vec{n}$ , which is acquired by calculating the least eigenvector of the covariance matrix of the neighbours around the corresponding candidate. Therefore, the scalar projection of the distance between a point to the planar surface represented by the normal vector  $\vec{n}$  instead of the Euclidean distance between the corresponding points are minimised:

$$R, \hat{t} = \arg \min_{R, t} \left( \sum_{i=1}^N \left\| ((Rp_i + t) - q_{pi}) \vec{n}_i \right\| \right). \quad (7.12)$$

where  $p_i$  denotes a point in the sensed point set,  $q_{pi}$  refers to its corresponding point in the reference dataset and  $\vec{n}_i$  signifies the normal vector of the local surface around  $q_{pi}$ . The algorithm then iterates to optimise the estimation.

### 7.6.3 Improvement of the lateral calibration

3D registration is inherently a great means of assessing the topography measurement results as it compares the difference between the measurement results and the reference dataset, which is especially useful for areal measurement.

The lateral calibration is typically done using a target with rulings to calculate the size corresponding to each pixel. The accuracy is limited by various types of aberrations of the imaging system. As a consequence, scaling errors typically exist. A 3D registration algorithm is useful for improving the lateral calibration by correcting the scaling errors compared to the commercial instruments with high accuracy.

#### 7.6.4 System calibration

The system calibration aims to obtain the relative location of the two probes via the calculation based on the registration results from the DPWSI measurement results to the reference topography. Thus, the registration between the DPWSI measurement results and the reference topography is critical. To achieve the registration, an open-source software called CloudCompare was used to achieve the initial estimation. By selecting the corresponding feature points from the reference and measurement point sets, the rough transformation between the two datasets was calculated. Then ICP algorithm was applied to realise the accurate alignment, namely calculating the transformation matrices  $R_1, R_2, t_1, t_2$ .

#### 7.7 Measurement data fusion

After the system calibration, the topography acquired with the DPWSI probes, can be blended together to achieve the whole topography of the inspected specimen as:

$$\left( \begin{array}{c} \left( \begin{array}{cc} R_1 & t_1 \end{array} \right) X \\ \left( \begin{array}{cc} 0 & 1 \end{array} \right) \end{array} \right) \rightarrow \left( \begin{array}{c} \left( \begin{array}{cc} R_1 & t_1 \end{array} \right)^{-1} \left( \begin{array}{cc} R_1 & t_1 \end{array} \right) X \\ \left( \begin{array}{cc} R_1 & t_1 \end{array} \right)^{-1} \left( \begin{array}{cc} R_2 & t_2 \end{array} \right) Y \\ \left( \begin{array}{cc} 0 & 1 \end{array} \right) \end{array} \right) = \left( \begin{array}{c} X \\ \left( \begin{array}{cc} R_1 & t_1 \end{array} \right)^{-1} \left( \begin{array}{cc} R_2 & t_2 \end{array} \right) Y \\ \left( \begin{array}{cc} 0 & 1 \end{array} \right) \end{array} \right). \quad (7.13)$$

where  $X$  represents the dataset acquired with probe 1, while  $Y$  refers to the result obtained with probe 2. To minimise the computation, the datasets can be transformed with rotations and translations in the same coordinate system as shown in Eq. (7.13) without causing any change to the result. However, sometimes there are some invalid data, especially at the area near the edges. The image segmentation algorithm is applied to remove the invalid data before the stitching.

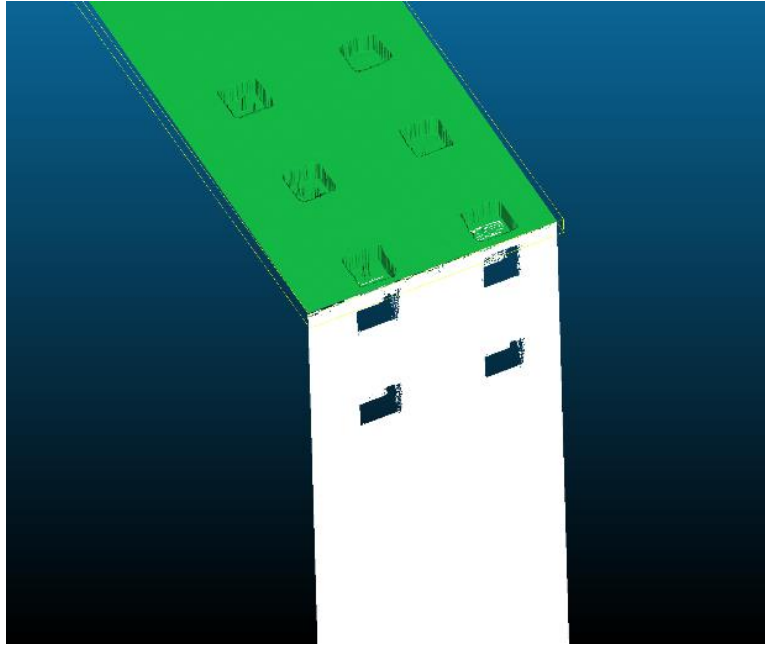
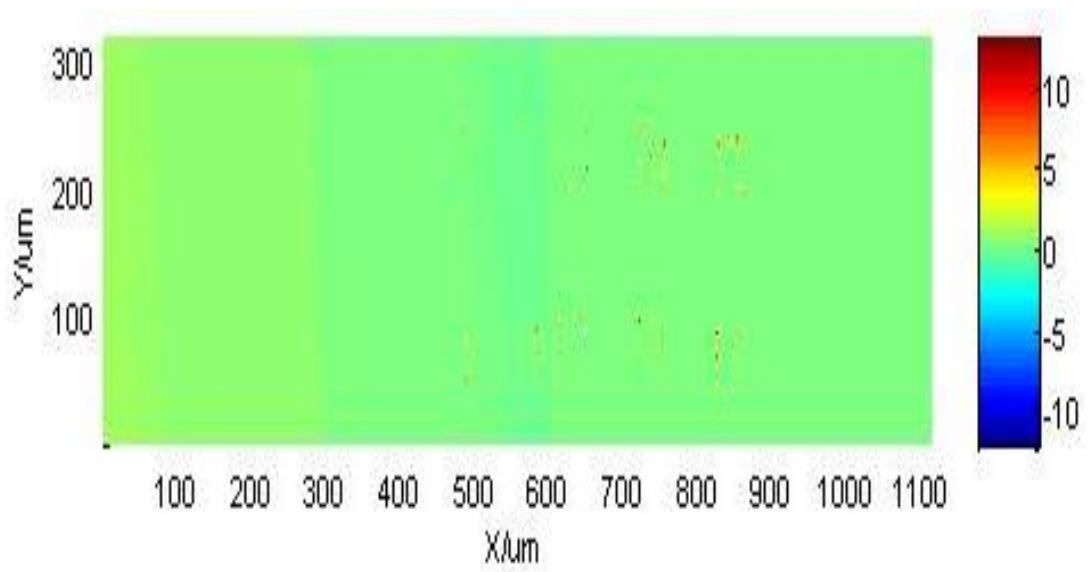
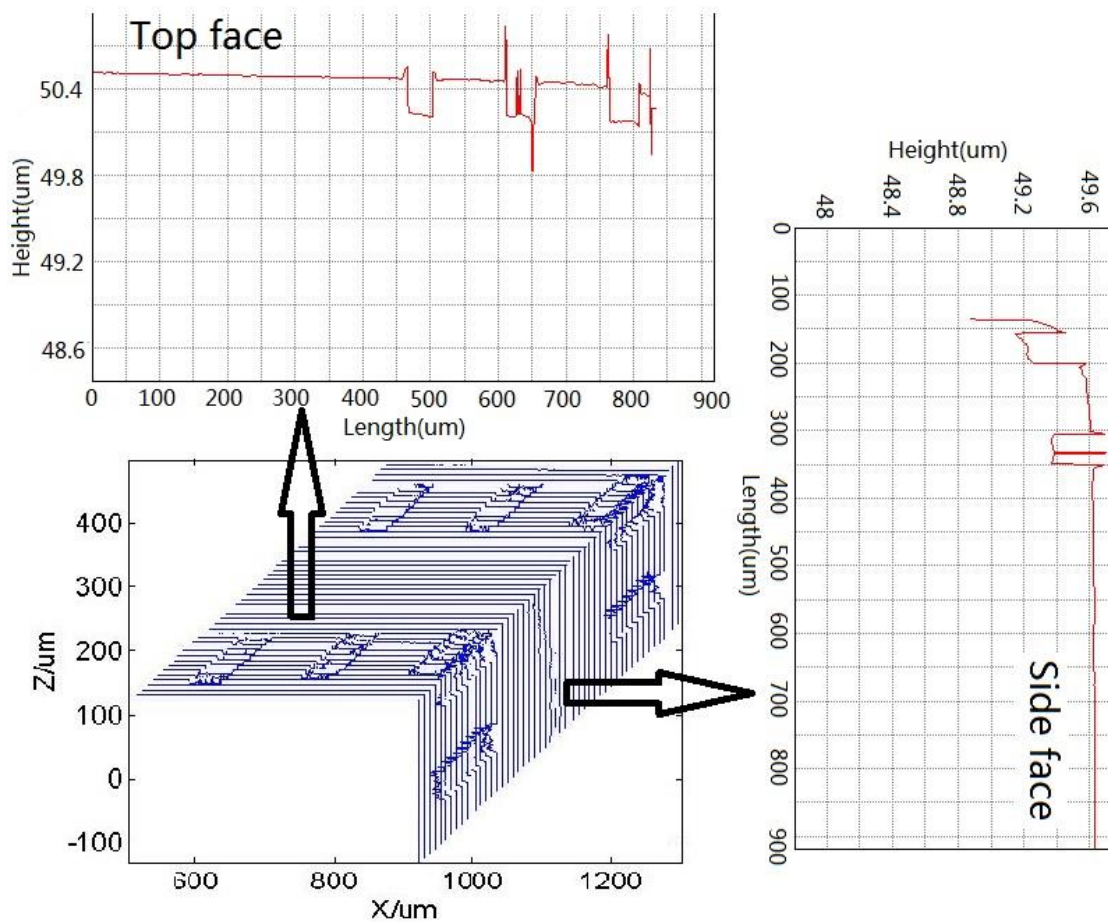


Figure 7.16 The measurement result of the calibration artefact by the DPWSI system plotted with CloudCompare (adapted from Zhang *et al.*, in-press).



(a)



(b)

Figure 7.17 (a) The residual error of the topography compared to the reference topography measured with Taylor Hobson CCI 3000 and FEI Quanta 200 3D FIB-SEM; (b) The extended 2D plots of the DPWSI topography (adapted from Zhang *et al.*, 2017).

Figure 7.16 shows the measurement result of the calibration artefact by the DPWSI system. Compared to the reference topography shown in Figure 7.12, the residual error of the overwhelming majority of the points (99.96%) is below  $4\ \mu\text{m}$ , which is about the lateral resolution of the interferometers. Only a small proportion of the points (0.04%) at the edge of the features the residual error is larger than  $4\ \mu\text{m}$  due to spike errors such as batwing, as illustrated in Figure 7.17(a). A series of the profiles are shown in Figure 7.17(b) divided with a small gap in blue. Compared to other dimensions, the depth of the features (about  $200\ \text{nm}$ ) is tiny, therefore, in Figure 7.17(b) the depth of the features is enlarged so that the features can be seen. A profile of authentic measurement data is also provided for the top and side face, respectively, in red. The dihedral angle between the two sidewalls is calculated and the result is  $89.9646^\circ$ . The deviation compared to the measurement result using autocollimator is  $2.144\ \text{arcminutes}$  which is quite large

but can partially be attributable to the manufacturing quality of the calibration artefact and improvement is believed to be achievable by enhancing the calibration artefact. The measurement was then repeated ten times. The measurement results showed ~95 nm RMS repeatability between the corresponding pixels. The relatively low repeatability can be attributed to the lack of the vibration compensation mechanism and the low data capturing speed, which are expected to be able to bring significant improvement (see Appendix C).

## **7.8 Summary**

The chapter presented the system calibration scheme for the DPWSI system. DPWSI is similar to subaperture stitching interferometry (SASI) in terms of fusing multiple measurements. However, there are also differences. The most important difference is that SASI needs overlapping areas to achieve the stitching but, for DPWSI, there are no overlapping measurable areas. Another important difference is that the relative location between the interferometer and the specimen changes for SASI during the measurement process but for DPWSI there are two interferometers and the measurements are performed simultaneously without any mechanical movement. Therefore, the goal of the system calibration is to achieve the relative location between the two probes. After that, the whole topography can be obtained by transforming the results into one coordinate system.

A custom calibration artefact with special features was used for assisting the calibration. The features played a vital role in matching the datasets. The boundary of the features ought to be clear and well-defined, in other words, the manufacturing quality of the features had a significant impact on the accuracy of the calibration. The experiment showed the average lateral deviation of the registration was micrometre scale, which was similar to the lateral resolution of the two probes (around 4  $\mu\text{m}$ ). As only rigid transformations were applied during the registration, the shapes of the two sidewalls were not changed. Thus, the vertical resolution of the two faces stayed unchanged in nanometre scale after the stitching but the relative location of the two faces was distorted by micrometre level.

All in all, DPWSI is a concept for linking the measurement coordinate systems of two effectively independent areal surface topography measurement systems based on WSI with the aid of a specially designed calibration artefact in order to simultaneously measure two narrow ranges of structured surfaces that are of importance in optics. The research is a pioneering attempt in the

ultra-precision topography measurement of structured surfaces and can potentially be used in the production line of the elements with near-right-angle V-groove microstructures, such as brightness enhancement films (BEF) etc. Part of the content in this chapter has already been published in Optics Express. The next chapter will present the verification result of the DPWSI system by measuring two specimens.

## 8 System verification

### 8.1 Overview

As a proof-of-principle demonstration of an optical system capable of measuring V-groove structures in a single measurement acquisition, this work aims to demonstrate the measurement of near-right-angle V-groove samples, with nominal  $90^\circ$  dihedral angle, but with deviation owing to tool error and process. This chapter reports on the measurement of two specimens to provide some validation of the system: These are a diamond turned multi-stepped artefact and a metallised prismatic film, featuring near right-angle grooves having a peak-to-valley height of  $32\ \mu\text{m}$  and nominal pitch of  $25\ \mu\text{m}$ .

### 8.2 A diamond-turned specimen

The measurand is a cylindrical multi-step diamond-turned specimen with  $20\ \mu\text{m}$  step height and cylinder diameter of around  $20\ \text{mm}$ , as illustrated in Figure 8.1. The measurement result by DPWSI is shown in Figure 8.2. Part of the data is lost in the edge and high-sloped area of the measurand owing to the edge and slope effects. As a comparison, Figure 8.3 shows the measurement result of the same measurand using Taylor Hobson CCI 3000, which is in good agreement with DPWSI result. The only problem is that Taylor Hobson CCI 3000 only retrieves the information in one direction and provides no information about the side face. The data of the side face in Figure 8.3 is not real, but only interpolated.

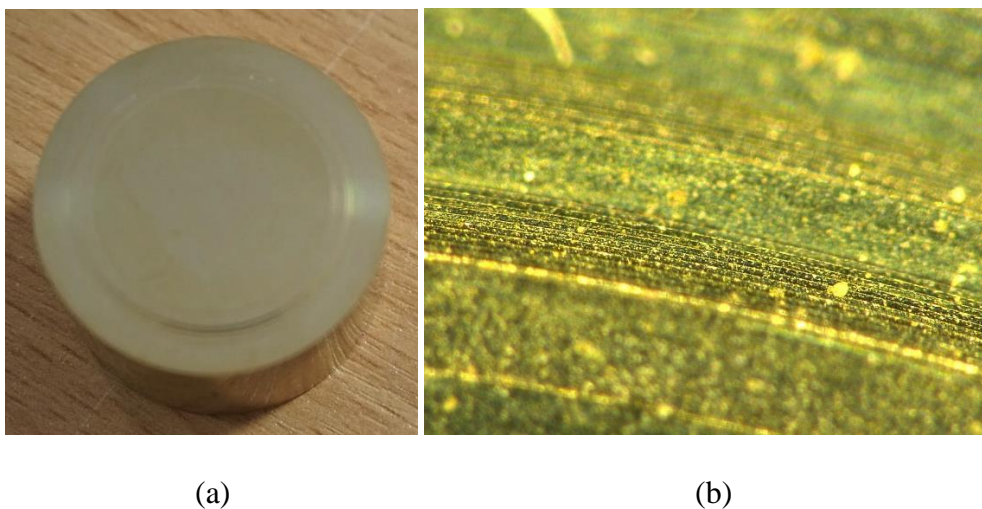
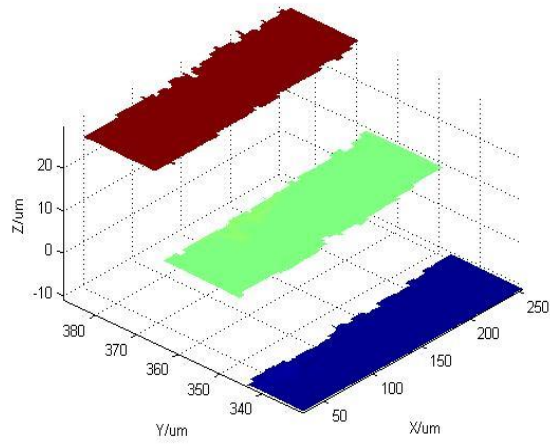
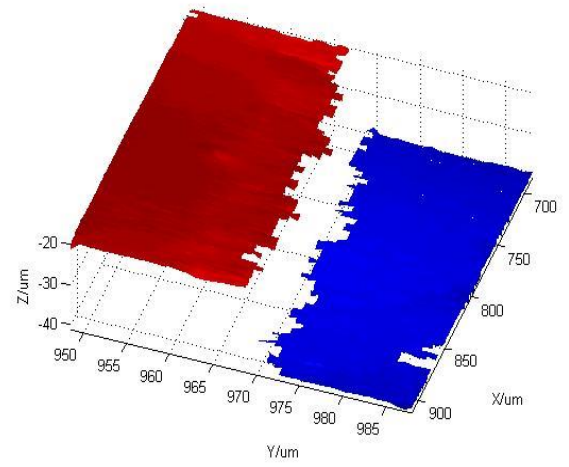


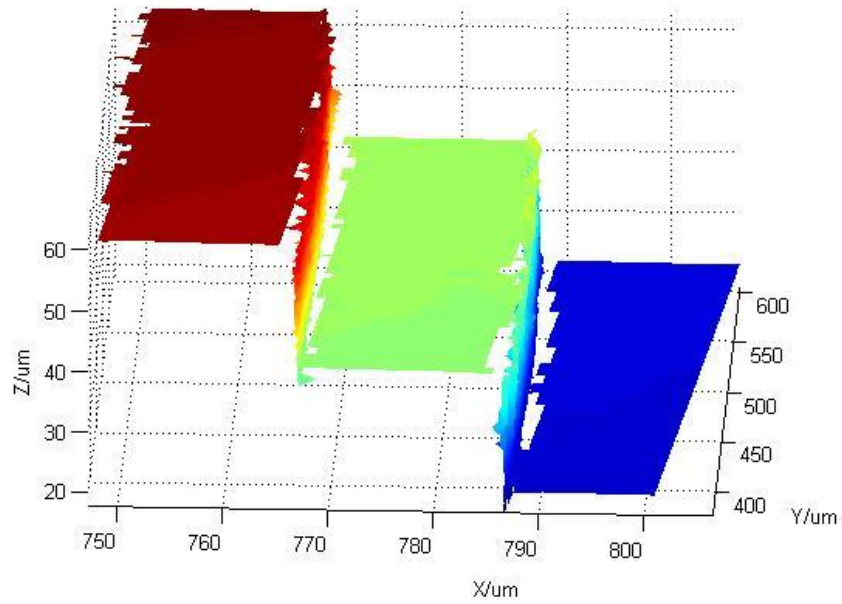
Figure 8.1 (a). A photo of the specimen. (b). A micrograph measured by optical microscope (Keyence VHX-500F).



(a). Probe 1



(b). Probe 2



(c). Stitched result

Figure 8.2 The measurement result of the diamond turned specimen by DPWSI (adapted from Zhang *et al.*, 2017).

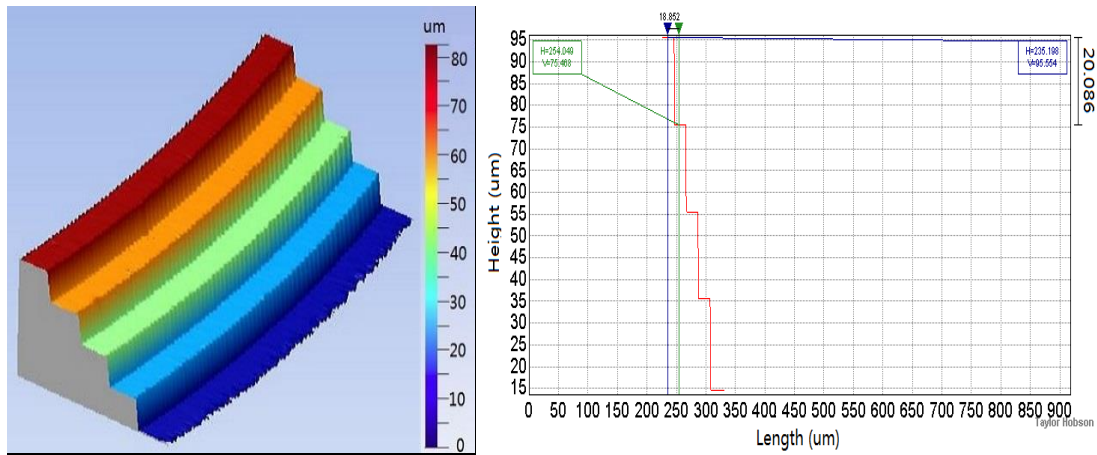
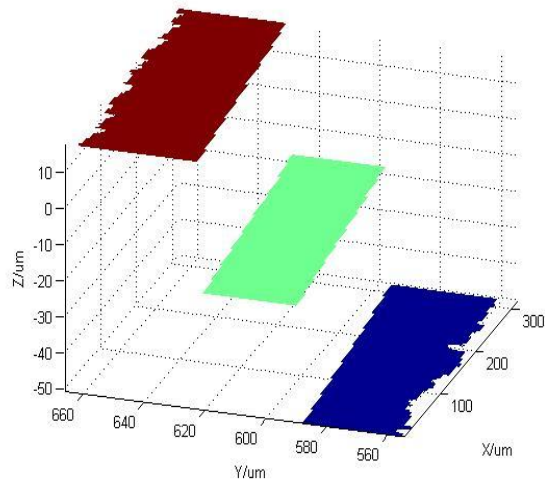


Figure 8.3 The measurement result of the diamond turned specimen by Taylor Hobson CCI 3000 (adapted from Zhang *et al.*, 2017).

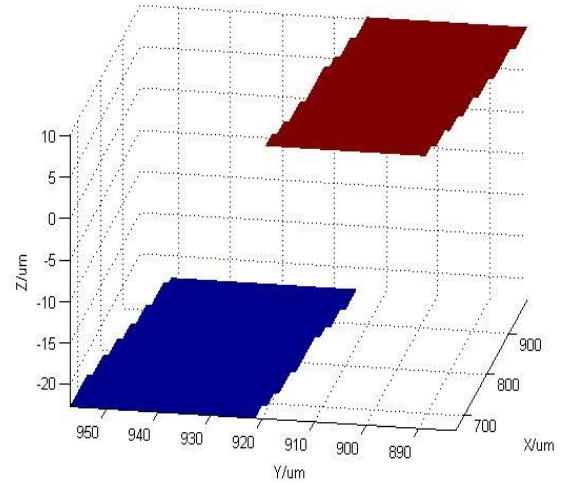
### 8.3 A sawtooth metallised prismatic film

A metallised prismatic film manufactured by Microsharp Co. Ltd. was measured using the DPWSI system. Figure 8.4 shows the individual data obtained from each probe as well as the combined result. The height of the measured step features is  $\sim 32 \mu\text{m}$  and the nominal pitch is  $25 \mu\text{m}$ . It is apparent that in high curvature areas (peaks tops/valley bottoms) some measurement data loss is experienced, which is because of the previously mentioned NA dependent acceptance angle limitation for the optics (Malacara, 2007). Nonetheless, it is clear that a large proportion of the artefact has been successfully measured in a single acquisition, with the instrument in a single orientation.

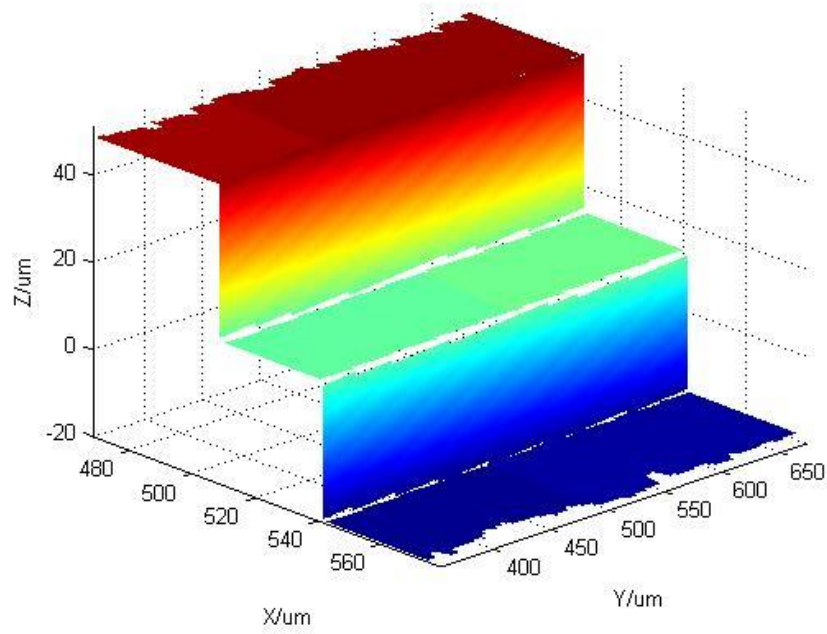
Figure 8.5 compares a profile taken from the DPWSI measurement result with one obtained across a similar region with a stylus profilometer (Taylor Hobson PGI Form Talysurf Series 2) using a  $2 \mu\text{m}$  tip radius stylus. The stylus profile was optimised using a deconvolution filter which provides some limited improvement in the obvious low-pass mechanical filtering exhibited by the tip radius in the peaks/valleys regions of the profile. For the DPWSI profile, the small amount of missing data apparent in Figure 8.4 in those same regions has been interpolated to complete the profile. Note that the peaks/valleys regions were confirmed as being physically sharp using SEM imaging.



(a). Probe 1



(b). Probe 2



(c) Stitched result

Figure 8.4 The measurement result of a metallised prismatic film (adapted from Zhang *et al.*, 2017).

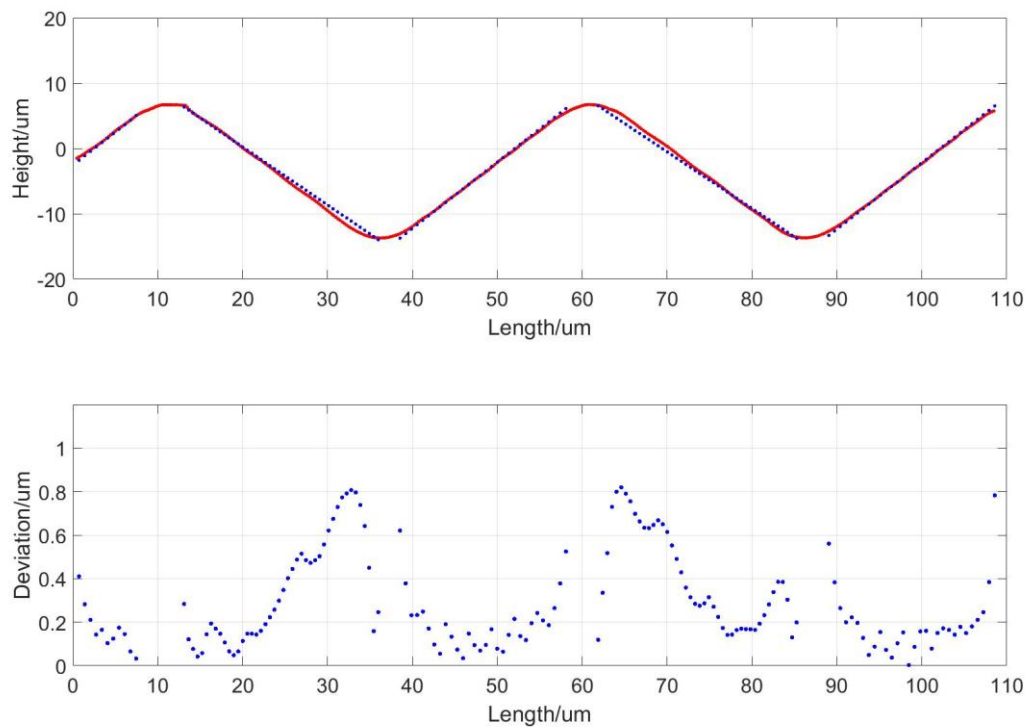


Figure 8.5 Top. The comparison of the measured profiles of the metallised prismatic film by the DPWSI (blue) and stylus profilometry (red).

Bottom. Plot of the residual error between the DPWSI and stylus profiles obtained from the ICP algorithm used to register the two datasets (adapted from Zhang *et al.*, in-press).

#### 8.4 Error source discussion

The system measurement error can mainly be attributed to the calibration error and the measurement error.

The calibration error mainly originates from the following sources:

Fringe analysis error. The interferograms are analysed by the fringe analysis algorithms which would induce some uncertainties. The error is axial and ranging from nanometre to submicrometre level (below 100 nm), irrespective of being processed by the phase slope method or fringe order determination algorithm (Takeda & Yamamoto, 1994; Moschetti *et al.*, 2016; Zhang *et al.*, 2018).

Algorithmic errors, include the error resulting from the image processing, such as the segmentation error and registration residual error. The segmentation error is caused by various reasons, such as the edge effect, which causes the spike error, the fabrication quality of the calibration artefact, and

all of the factors that make it difficult to clearly extract the features. The registration residual error derives not only from the 3D registration algorithm but also from the mismatch between the reference dataset and the measurement dataset. For example, the sampling intervals between the reference results and the measurement results are different, which would contribute largely to the residual error. The algorithmic error can be reduced by reforming the calibration artefact and adding more features to it.

Environmental error. The environmental error is stochastic and mainly refers to the vibration, which is inevitable. To minimise the error of this type, the calibration should be accomplished in a quiet environment with the vibration being well-insulated or compensated.

For each measurement, the results from the two probes are combined together based on the calibration result. Therefore, the calibration error is totally propagated. Apart from this, there also exist other sources of errors—for example, the fringe analysis error of each probe, as well as the environmental error during the measurement.

Despite these error sources, the average deviation of the registration is at a micrometre level. It is in the same order of magnitude as the lateral resolution of the optical apparatus (about 4  $\mu\text{m}$ ). As only rigid transformations are applied during the registration process, the shapes of the two sidewalls are not changed; therefore, the axial resolution of the two faces keeps the same in submicrometre scale after the fusion of the datasets.

To sum up, the experimental results show that the proposed metrology system has provided a demonstration of a novel approach to inspect structured surfaces with double-sided near-right-angle facets and output the topography with submicrometre-scale axial resolution on each facet and micrometre-scale lateral resolution. Most of the surface information can be retrieved apart from the parts of the surfaces where the normals scatter the incident light beyond the NA of the probes and all the surface parameters such as  $S_a$ ,  $S_q$ ,  $S_z$ , flatness, etc., can be calculated from the obtained topography. For a given probe, a range of V-groove angles is measurable, limited by the acceptance angle of the objective lenses employed. This range can be expanded further by designing equivalent probe heads with varying angular separation to achieve the inspection of sawtooth V-groove specimens with arbitrary dihedral angles. There has not been a full uncertainty analysis owing to the time limit, such as type A or B evaluation. But this has been listed in the future work.

## **8.5 Summary**

This chapter demonstrated the capability of the DPWSI system by measuring some near-right-angle V-groove specimens and comparing the measurement results with the corresponding results measured by other commercial instruments, such as CSI or stylus profilometry. The results showed that the reported metrology system has realised a novel approach to achieve the measurement of near-right-angle V-groove structured surfaces and yield the topography with submicrometre-scale vertical resolution on the sidewalls and overall micrometre scale lateral resolution. The method can be expanded further by designing equivalent probe heads with varying angular separation for achieving more universal applications.

## **9 Discussion, Conclusions and Future Work**

### **9.1 Introduction**

The chapter aims to summarise and consider the results obtained from the investigations made in the whole thesis to draw an overall conclusion for the thesis. The future work for further investigation is also summarised and listed in detail.

### **9.2 Discussion**

The development of modern advanced manufacturing technologies generates enormous demand for a diversity of complex structured surfaces such as sawtooth structures, micropyramids, etc. Thus, a huge challenge arises for the inspection. The miniaturisation trend of the structures further exacerbates the challenge. Despite a large number of attempts and efforts to investigate the inspection of the structures, there is still no suitable means of achieving the goal. Because of the significant complexities, the study adopts a divide-and-conquer scheme. That is, first focuses on a special type of structured surfaces as an initial goal, namely near-right-angle sawtooth structures to build confidence, and then expands the solution to other types of structured surfaces, such as V-grooves with arbitrary dihedral angles, pyramidal structures, and so forth to overcome the challenge.

The thesis proposes a novel methodology to tackle the challenge by building an apparatus encompassing two or more measurement probes to acquire the dataset for each facet of the structured surface and then blending the obtained datasets together, based on the relative location of the probes, which was achieved via the system calibration. The method is reliant on wavelength scanning interferometry (WSI), which is able to realise areal measurement with submicrometre-scale axial resolution with no requirement for mechanical scanning of either the specimen or optics, different from comparable techniques such as phase-shifting interferometry (PSI). This lack of mechanical scanning opens up the possibility of applying a multi-probe optics system to achieve simultaneous measurement with multiple adjacent fields of view. However, the thesis focuses on the implementation and verification of the inspection system for near-right-angle V-groove surfaces owing to the limited time period in practice. But it can be anticipated that the solution for structured surfaces with more facets can be realised in this way

The thesis presents a proof-of-principle demonstration of a dual-probe wavelength scanning interferometry (DPWSI) system capable of measuring near-right-angle V-groove structures in a single measurement acquisition. The optical system comprising dual probes, with orthogonal measurement planes has been built. The fringe analysis algorithms for WSI were investigated, some improvements were proposed, and experimental validation has been done. The scheme for calibrating the DPWSI system and obtaining the relative location between the probes to achieve the whole topography has been implemented and was presented as well. The appraisal of the DPWSI system was also carried out using some specimens.

For each probe of the DPWSI system, a range of angles are measurable, restricted by the numerical aperture (NA) of the objectives adopted. This range can be expanded further by designing equivalent probe heads with varying angular separation. More complicated structured surfaces, such as micro-pyramids, can be inspected by increasing the number of probes and establishing the positional relationships between all of the probes. Thus, there is still a huge amount of work to do in order to overcome the challenge.

### **9.3 Conclusion**

The thesis demonstrates the principle, apparatus, algorithm and operation of an optic-mechanical system encompassing two measurement probes based upon wavelength scanning interferometry (WSI) that provided two orthogonally located fields of view to enable near-right-angle V-groove measurement. The fringe analysis algorithms for WSI were investigated and simulated, the approach of improvement based upon the optimisation of filter design in accordance with the simulation results were proposed, and experimental validation was performed. A system calibration procedure involving a custom designed calibration artefact was utilised to provide registration of the two fields to attain the relative location of the two probes to achieve the whole topography.

Some specimens were inspected with the DPWSI system to prove the feasibility of near-right-angle V-groove measurement, including a diamond-turned specimen and a metallised prismatic film. The experimental results showed the proposed measurement system has demonstrated a novel approach to inspect the near-right-angle V-groove surfaces and yield the topography with submicrometre-scale vertical resolution on each facet and micrometre scale lateral resolution.

Part of the work carried out on the DPWSI system in Chapters 5, 7 and 8 has been published in *Optics Express* (Zhang *et al.*, 2017). Some of the content was also presented in the 13th International Symposium on Measurement Technology and Intelligent Instruments hosted by Xi'an Jiaotong University in Xi'an, China and was awarded the best paper, and has been accepted and will soon be published in *The International Journal of Advanced Manufacturing Technology* (Zhang *et al.*, in-press).

The work contained in Chapter 6 of the thesis for improving the fringe analysis algorithm for wavelength scanning interferometry (WSI) via optimising the filter design has been published in *Applied Optics* (Zhang *et al.*, 2018).

#### **9.4 Future work**

The work contained in this thesis suggested the feasibility of a DPWSI system for surface topography acquisition of near-right-angle V-groove surfaces. However, there are several fields that require further development and investigation to advance the research to enable the inspection of multiple types of structured surfaces with high performance such as the resolution, accuracy, repeatability, automaticity, etc.

For a short-term plan, further work should focus on the measurement of near-right-angle V-groove surfaces based upon the existent apparatus to improve performance, including accuracy, measurement speed, stability, repeatability, automaticity, and so forth. The work is listed in detail item by item:

- More verification work is required. For example, more near-right-angle V-groove specimens should be adopted to fully verify the system.
- Examine in more detail the errors associated with the calibration procedure and aim to minimise these through a combination of improved artefact fabrication, improved reference topography construction, feature extraction, and registration algorithm optimisation. All of the listed items will significantly benefit the calibration and help to improve the accuracy of the measurement system.
- Increase the image capturing speed to minimise the impact of the environmental noise, such as air turbulence, thermal drift, environmental vibration, etc. This can be achieved by using faster cameras and storing the interferograms in RAM instead of hard drive. More

rigorous insulation can also be employed to reduce the impact. For example, mechanical insulation can effectively eliminate the vibration while spatial isolation is helpful for tackling the air turbulence.

- Integration of the vibration compensation mechanism to increase the resistance of the measurement system to the environmental noise. For example, Muhamedsalih *et al.* proposed a method that aimed to achieve this using a reference interferometer (Muhamedsalih *et al.*, 2013). This may require some modifications to the interference objectives, as well as the light source.
- Integrate all of the operations, such as interferograms capturing, fringe analysis, and dataset blending into one application program. The processing can be accelerated by using parallel algorithms and high-performance computers with GPU/CUDA (Wilt, 2013). The goal is to realise real-time and fully automatic measurement of the near-right-angle V-groove measurands.
- Improvement of the tunable light source. A reasonably warm white light LED with high intensity should be carefully chosen to replace the tungsten-halogen bulb. This helps to provide better spectral performance and the power consumption can also be saved.

For a long-term plan, the system could be expanded to inspect other types of complex structured surfaces, such as V-groove surfaces with arbitrary dihedral angles, micro-pyramids, and so forth, and the inspection performance could be further improved. The work is summarised in detail as below:

- Enable the measurement of V-groove structures with arbitrary dihedral angles. For a given probe, a range of angles are measurable, restricted by the numerical aperture (NA) of the objective lenses adopted. The range can be expanded further by designing equivalent probe heads with varying angular separation.
- Enable the measurement of complicated structures with more facets, such as micro-pyramids, by adding extra probes. The calibration can be accomplished by establishing the positional relationships between all of the probes.
- Investigate the signal to noise ratio (SNR) estimation algorithm to achieve an adaptive filter to optimise the performance of fringe analysis to attain optimal accuracy and improve the immunity to noise, as described in Chapter 6.

- Integrate the whole system including the hardware, algorithm, and software together to provide a turnkey solution for the measurement of structured surfaces.

## References

- Abbot, E., & Firestone, F. (1933). Specifying surface quality. *Mech. Eng.*, 55(9), 569-572.
- Ai, C., & Novak, E. L. (1997). Centroid approach for estimating modulation peak in broad-bandwidth interferometry. In: Google Patents.
- Alexander, S., Hellemans, L., Marti, O., Schneir, J., Elings, V., Hansma, P. K., . . . Gurley, J. (1989). An atomic-resolution atomic-force microscope implemented using an optical lever. *Journal of Applied Physics*, 65(1), 164-167.
- Anselmetti, D., Behm, R., van Bentum, P., Chiang, S., Hamers, R., van Kempen, H., . . . Wintterlin, J. (2012). *Scanning Tunneling Microscopy I: General Principles and Applications to Clean and Adsorbate-Covered Surfaces* (Vol. 20): Springer Science & Business Media.
- Areef Billah, A. (2016). Investigation of multiferroic and photocatalytic properties of Li doped BiFeO<sub>3</sub> nanoparticles prepared by ultrasonication.
- Bellekens, B., Spruyt, V., Berkvens, R., & Weyn, M. (2014). *A survey of rigid 3d pointcloud registration algorithms*. Paper presented at the AMBIENT 2014: the Fourth International Conference on Ambient Computing, Applications, Services and Technologies, August 24-28, 2014, Rome, Italy.
- Bennett, H., & Porteus, J. (1961). Relation between surface roughness and specular reflectance at normal incidence. *JOSA*, 51(2), 123-129.
- Bennett, J., & Mattsson, L. (1989). Introduction to surface roughness and scattering. *Introduction to Surface Roughness and Scattering by Jean Bennett, Lars Mattsson Washington DC: Optical Society of America, 1989*.
- Bennett, J. M., & Dancy, J. (1981). Stylus profiling instrument for measuring statistical properties of smooth optical surfaces. *Applied optics*, 20(10), 1785-1802.
- Besl, P. J., & McKay, N. D. (1992). *Method for registration of 3-D shapes*. Paper presented at the Sensor Fusion IV: Control Paradigms and Data Structures.
- Beucher, S., & Meyer, F. (1992). The morphological approach to segmentation: the watershed transformation. *Optical Engineering-New York-Marcel Dekker Incorporated-*, 34, 433-433.
- Biegen, J. F. (1990). Interferometric surface profiler for spherical surfaces. In: Google Patents.
- Binnig, G., Quate, C. F., & Gerber, C. (1986). Atomic force microscope. *Physical review letters*, 56(9), 930.
- Binnig, G., & Rohrer, H. (1983). Scanning tunneling microscopy. *Surface science*, 126(1-3), 236-244.
- Blunt, L., Fleming, L., Elrawemi, M., Robbins, D., & Muhamedsalih, H. (2013). In-line metrology of functional surfaces with a focus on defect assessment on large area Roll to Roll substrates. In: EUSPEN.
- Blunt, L., & Jiang, X. (2003). *Advanced techniques for assessment surface topography: development of a basis for 3D surface texture standards" surfstand"*: Elsevier.
- Bowe, B. W., & Toal, V. (1998). White light interferometric surface profiler. *Optical Engineering*, 37(6), 1796-1800.
- Bracewell, R. N., & Bracewell, R. N. (1986). *The Fourier transform and its applications* (Vol. 31999): McGraw-Hill New York.
- Braga, P. C., & Ricci, D. (2004). *Atomic force microscopy: biomedical methods and applications* (Vol. 242): Springer Science & Business Media.
- Bray, M. (1999). *Stitching interferometry: how and why it works*. Paper presented at the Optical

Fabrication and Testing.

- Bray, M. (2009). *Stitching interferometry: the practical side of things*. Paper presented at the Optical Manufacturing and Testing VIII.
- Brown, C., Charles, P. D., Johnsen, W., & Chesters, S. (1993). Fractal analysis of topographic data by the patchwork method. *Wear*, 161(1-2), 61-67.
- Brown, L. G. (1992). A survey of image registration techniques. *ACM computing surveys (CSUR)*, 24(4), 325-376.
- Bucher, E. G., & Carnahan, J. W. (1999). Characterization of an acousto-optic tunable filter and use in visible spectrophotometry. *Applied spectroscopy*, 53(5), 603-611.
- Buhr, E., Senftleben, N., Klein, T., Bergmann, D., Gnieser, D., Frase, C., & Bosse, H. (2009). Characterization of nanoparticles by scanning electron microscopy in transmission mode. *Measurement Science and Technology*, 20(8), 084025.
- Calatroni, J., Guerrero, A. L., Sainz, C., & Escalona, R. (1996). Spectrally-resolved white-light interferometry as a profilometry tool. *Optics & Laser Technology*, 28(7), 485-489.
- Chang, L.-W., Chien, P.-Y., & Lee, C.-T. (1999). Measurement of absolute displacement by a double-modulation technique based on a Michelson interferometer. *Applied optics*, 38(13), 2843-2847.
- Chen, C. J. (1993). *Introduction to scanning tunneling microscopy* (Vol. 4): Oxford University Press on Demand.
- Chen, C.-S., Hung, Y.-P., & Cheng, J.-B. (1999). RANSAC-based DARCES: A new approach to fast automatic registration of partially overlapping range images. *IEEE Transactions on Pattern Analysis and Machine Intelligence*, 21(11), 1229-1234.
- Chen, S., Li, S., & Dai, Y. (2016). *Subaperture stitching interferometry: jigsaw puzzles in 3D space*.
- Chen, X., Raja, J., & Simanapalli, S. (1995). Multi-scale analysis of engineering surfaces. *International Journal of Machine Tools and Manufacture*, 35(2), 231-238.
- Cheng, Y.-Y., & Wyant, J. C. (1984). Two-wavelength phase shifting interferometry. *Applied optics*, 23(24), 4539-4543.
- Church, E. L., & Zavada, J. (1975). Residual surface roughness of diamond-turned optics. *Applied optics*, 14(8), 1788-1795.
- Coker, S. A., & Shin, Y. C. (1996). In-process control of surface roughness due to tool wear using a new ultrasonic system. *International Journal of Machine Tools and Manufacture*, 36(3), 411-422.
- Conchello, J.-A., Kim, J. J., & Hansen, E. W. (1994). Enhanced three-dimensional reconstruction from confocal scanning microscope images. II. Depth discrimination versus signal-to-noise ratio in partially confocal images. *Applied optics*, 33(17), 3740-3750.
- Conroy, M., & Armstrong, J. (2005). *A comparison of surface metrology techniques*. Paper presented at the Journal of Physics: Conference Series.
- Creath, K. (1987). Step height measurement using two-wavelength phase-shifting interferometry. *Applied optics*, 26(14), 2810-2816.
- Creath, K. (1988). V phase-measurement interferometry techniques. In *Progress in optics* (Vol. 26, pp. 349-393): Elsevier.
- De Broglie, L. (1925). Sur la fréquence propre de l'électron. *Compt. Rend. Acad. Sci*, 180, 498.
- De Chiffre, L., Kunzmann, H., Peggs, G., & Lucca, D. (2003). Surfaces in precision engineering, microengineering and nanotechnology. *CIRP Annals-Manufacturing Technology*, 52(2), 561-577.
- de Groot, P., de Lega, X. C., Kramer, J., & Turzhitsky, M. (2002). Determination of fringe order

- in white-light interference microscopy. *Applied optics*, 41(22), 4571-4578.
- De Groot, P. J. (1995). Vibration in phase-shifting interferometry. *JOSA A*, 12(2), 354-365.
- de Lega, X. C., Grigg, D., & de Groot, P. (2004). *Surface profiling using a reference-scanning Mirau interference microscope*. Paper presented at the Interferometry XII: Applications.
- Debnath, S. K., & Kothiyal, M. P. (2006). Improved optical profiling using the spectral phase in spectrally resolved white-light interferometry. *Applied optics*, 45(27), 6965-6972.
- Debnath, S. K., Kothiyal, M. P., & Kim, S.-W. (2009). Evaluation of spectral phase in spectrally resolved white-light interferometry: Comparative study of single-frame techniques. *Optics and Lasers in Engineering*, 47(11), 1125-1130.
- Debnath, S. K., Kothiyal, M. P., Schmit, J., & Hariharan, P. (2006). Spectrally resolved white-light phase-shifting interference microscopy for thickness-profile measurements of transparent thin film layers on patterned substrates. *Optics express*, 14(11), 4662-4667.
- Deck, L. (1996). Vibration-resistant phase-shifting interferometry. *Applied optics*, 35(34), 6655-6662.
- Dunn, D., & Higgins, W. E. (1995). Optimal Gabor filters for texture segmentation. *IEEE Transactions on image processing*, 4(7), 947-964.
- El Gawhary, O., Kumar, N., Pereira, S., Coene, W., & Urbach, H. (2011). Performance analysis of coherent optical scatterometry. *Applied Physics B*, 105(4), 775-781.
- Elrawemi, M., Blunt, L., Muhamedsalih, H., Gao, F., & Fleming, L. (2015). Implementation of in process surface metrology for R2R flexible PV barrier films. *International Journal of Automation Technology*, 9(3), 312-321.
- Evans, C. J., & Bryan, J. B. (1999). "Structured", "textured" or "engineered" surfaces. *CIRP annals*, 48(2), 541-556.
- Fang, F., Zeng, Z., Zhang, X., & Jiang, L. (2016). Measurement of micro-V-groove dihedral using white light interferometry. *Optics Communications*, 359, 297-303.
- Fess, E. (2012). Freeform Optics: The next Generation of Precision Optical Components. *Laser Focus World, On-line Webinar*.
- Fibics Inc. Introduction: Focused Ion Beam Systems [Online]. Available: <http://www.fibics.com/fib/tutorials/introduction-focused-ion-beam-systems/4/>.
- Führer, T., & Walther, T. (2008). Extension of the mode-hop-free tuning range of an external cavity diode laser based on a model of the mode-hop dynamics. *Optics Letters*, 33(4), 372-374.
- Gao, F., Coupland, J., & Petzing, J. (2006). V-groove measurements using white light interferometry. *Photon06, Manchester*, 4-7.
- Gao, F., Leach, R. K., Petzing, J., & Coupland, J. M. (2007). Surface measurement errors using commercial scanning white light interferometers. *Measurement Science and Technology*, 19(1), 015303.
- Gao, F., Muhamedsalih, H., & Jiang, X. (2012). Surface and thickness measurement of a transparent film using wavelength scanning interferometry. *Optics express*, 20(19), 21450-21456.
- Garratt, J. (1977). *An interferometric transducer for surface metrology*. University of Aberdeen.
- Ghim, Y.-S., & Davies, A. (2012). Complete fringe order determination in scanning white-light interferometry using a Fourier-based technique. *Applied optics*, 51(12), 1922-1928.
- Giannuzzi, L. A. (2004). *Introduction to focused ion beams: instrumentation, theory, techniques and practice*: Springer Science & Business Media.
- Goldstein, J. I., Newbury, D. E., Michael, J. R., Ritchie, N. W., Scott, J. H. J., & Joy, D. C. (2017). *Scanning electron microscopy and X-ray microanalysis*: Springer.
- Goshtasby, A. A. (2005). *2-D and 3-D image registration: for medical, remote sensing, and*

- industrial applications*: John Wiley & Sons.
- Gregg, A., York, L., & Strnad, M. (2005). Roll-to-Roll Manufacturing of Flexible Displays, Flexible Flat Panel Displays. In: John Wiley & Sons, New York.
- Grimm, T., Wiora, G., & Witt, G. (2015). Characterization of typical surface effects in additive manufacturing with confocal microscopy. *Surface Topography: Metrology and Properties*, 3(1), 014001.
- Grous, A. (2013). *Applied metrology for manufacturing engineering*: John Wiley & Sons.
- Haneishi, H. (1984). Signal processing for film thickness measurements by white light interferometry. *Graduate thesis Department of Communications and Systems Engineering, University of Electro-communications, Chofu, Tokyo*.
- Harasaki, A., Schmit, J., & Wyant, J. C. (2000). Improved vertical-scanning interferometry. *Applied optics*, 39(13), 2107-2115.
- Harasaki, A., Schmit, J., & Wyant, J. C. (2001). Offset of coherent envelope position due to phase change on reflection. *Applied optics*, 40(13), 2102-2106.
- Hariharan, P. (1991). Optical interferometry. *Reports on Progress in Physics*, 54(3), 339.
- Hariharan, P. (2010). *Basics of interferometry*: Academic Press.
- Hariharan, P., Oreb, B., & Eiju, T. (1987). Digital phase-shifting interferometry: a simple error-compensating phase calculation algorithm. *Applied optics*, 26(13), 2504-2506.
- Hecht, E. (2016). Optics. In: Pearson Education.
- Helmlí, F. (2011). Focus variation instruments. In *Optical Measurement of Surface Topography* (pp. 131-166): Springer.
- Hiersemenzel, F., Petzing, J. N., Leach, R. K., Helmlí, F., & Singh, J. (2012). Areal texture and angle measurements of tilted surfaces using focus variation methods.
- Hlubina, P. (2002). Dispersive white-light spectral interferometry to measure distances and displacements. *Optics Communications*, 212(1-3), 65-70.
- Hocken, R., Chakraborty, N., & Brown, C. (2005). Optical metrology of surfaces. *CIRP Annals-Manufacturing Technology*, 54(2), 169-183.
- Huntley, J. (1989). Noise-immune phase unwrapping algorithm. *Applied optics*, 28(16), 3268-3270.
- Inoué, S. (2006). Foundations of confocal scanned imaging in light microscopy. In *Handbook of biological confocal microscopy* (pp. 1-19): Springer.
- Ismail, M. F., Yanagi, K., & Fujii, A. (2010). An outlier correction procedure and its application to areal surface data measured by optical instruments. *Measurement Science and Technology*, 21(10), 105105.
- Jackson, L. B. (2013). *Digital Filters and Signal Processing: With MATLAB® Exercises*: Springer Science & Business Media.
- Jansen, M. J., Haitjema, H., & Schellekens, P. H. (2004). *Scanning wafer thickness and flatness interferometer*. Paper presented at the Optical Fabrication, Testing, and Metrology.
- Jia, J., & Tang, C.-K. (2008). Image stitching using structure deformation. *IEEE Transactions on Pattern Analysis and Machine Intelligence*, 30(4), 617-631.
- Jiang, X. (1995). *Theory and method for measurement of curved surface topography*. PhD dissertation, Huazhong University of Science and Technology, Wuhan, China.
- Jiang, X., Blunt, L., & Stout, K. (2000). *Development of a lifting wavelet representation for surface characterization*. Paper presented at the Proceedings of the Royal Society of London A: Mathematical, Physical and Engineering Sciences.
- Jiang, X., Scott, P. J., Whitehouse, D., & Blunt, L. (2007a). *Paradigm shifts in surface metrology. Part I. Historical philosophy*. Paper presented at the Proceedings of the Royal Society of London A: Mathematical, Physical and Engineering Sciences.

- Jiang, X., Scott, P. J., Whitehouse, D., & Blunt, L. (2007b). *Paradigm shifts in surface metrology. Part II. The current shift*. Paper presented at the Proceedings of the Royal Society of London A: Mathematical, Physical and Engineering Sciences.
- Jiang, X., Wang, K., Gao, F., & Muhamedsalih, H. (2010). Fast surface measurement using wavelength scanning interferometry with compensation of environmental noise. *Applied optics*, 49(15), 2903-2909.
- Jiang, X. J., & Whitehouse, D. J. (2012). Technological shifts in surface metrology. *CIRP Annals-Manufacturing Technology*, 61(2), 815-836.
- Ju, B.-F., Chen, Y.-L., Zhang, W., & Fang, F. (2012). Rapid measurement of a high step microstructure with 90 steep sidewall. *Review of Scientific Instruments*, 83(1), 013706.
- Kang, C.-m., Woo, H. G., Cho, H., Han, J. W., & Lee, J.-Y. (2001). *Inspection system for microelectronics BGA package using wavelength scanning interferometry*. Paper presented at the Optomechatronic Systems II.
- Kato, J.-i., & Yamaguchi, I. (2000). Phase-shifting fringe analysis for laser diode wavelength-scanning interferometer. *Optical review*, 7(2), 158-163.
- Kemao, Q., Fangjun, S., & Xiaoping, W. (2000). Determination of the best phase step of the Carré algorithm in phase shifting interferometry. *Measurement Science and Technology*, 11(8), 1220.
- Keränen, K., Jaakola, T., Korhonen, P., Antonipieri, M., Salomon, J., Visentin, L., . . . Pira, N. L. (2012). *Demonstrators for autonomous automotive and signage applications by bonding flexible solar cells, batteries and LED elements on large area polycarbonate backplanes*. Paper presented at the Electronic System-Integration Technology Conference (ESTC), 2012 4th.
- Kikuta, H., Iwata, K., & Nagata, R. (1986). Distance measurement by the wavelength shift of laser diode light. *Applied optics*, 25(17), 2976-2980.
- Kimbrough, B., Frey, E., & Millerd, J. (2008). *Instantaneous phase-shift Fizeau interferometer utilizing a synchronous frequency shift mechanism*. Paper presented at the Interferometry XIV: Techniques and Analysis.
- Kimbrough, B., & Novak, E. (2015). *In-line roll-to-roll metrology for flexible electronics*. Paper presented at the Applied Advanced Optical Metrology Solutions.
- Kin, C.-J., & Wyant, J. (1981). Subaperture test of a large flat or a fast aspheric surface. *J. Opt. Soc. America*, Vol. 71, p. 1587, 71, 1587.
- Krebs, F. C., Fyenbo, J., & Jørgensen, M. (2010). Product integration of compact roll-to-roll processed polymer solar cell modules: methods and manufacture using flexographic printing, slot-die coating and rotary screen printing. *Journal of Materials Chemistry*, 20(41), 8994-9001.
- Krystek, M. (1996). Form filtering by splines. *Measurement*, 18(1), 9-15.
- Krystek, M. (1997). Transfer functions of discrete spline filters. *SERIES ON ADVANCES IN MATHEMATICS FOR APPLIED SCIENCES*, 45, 203-210.
- Kumar, U. P., Mohan, N. K., & Kothiyal, M. (2008). *Multiple wavelength interferometry for surface profiling*. Paper presented at the Interferometry XIV: Techniques and Analysis.
- Kuwamura, S., & Yamaguchi, I. (1997). Wavelength scanning profilometry for real-time surface shape measurement. *Applied optics*, 36(19), 4473-4482.
- Larkin, K. G. (1996). Efficient nonlinear algorithm for envelope detection in white light interferometry. *JOSA A*, 13(4), 832-843.
- Le Goïc, G., Brown, C., Favreliere, H., Samper, S., & Formosa, F. (2012). Outlier filtering: a new method for improving the quality of surface measurements. *Measurement Science and Technology*, 24(1), 015001.

- Leach, R. (2011). *Optical measurement of surface topography* (Vol. 14): Springer.
- Lehmann, P., Kühnhold, P., & Xie, W. (2014). Reduction of chromatic aberration influences in vertical scanning white-light interferometry. *Measurement Science and Technology*, 25(6), 065203.
- Lehmann, P., Tereschenko, S., & Xie, W. (2016). Fundamental aspects of resolution and precision in vertical scanning white-light interferometry. *Surface Topography: Metrology and Properties*, 4(2), 024004.
- Leskova, T., Maradudin, A., Garcia-Guerrero, E., & Mendez, E. (2007). Structured surfaces as optical metamaterials. *Metamaterials*, 1(1), 19-39.
- Levin, A., Zomet, A., Peleg, S., & Weiss, Y. (2004). *Seamless image stitching in the gradient domain*. Paper presented at the European Conference on Computer Vision.
- Li, D., Cheung, C. F., Ren, M., Whitehouse, D., & Zhao, X. (2015). Disparity pattern-based autostereoscopic 3D metrology system for in situ measurement of microstructured surfaces. *Optics Letters*, 40(22), 5271-5274.
- Li, D., Cheung, C. F., Ren, M., Zhou, L., & Zhao, X. (2014). Autostereoscopy-based three-dimensional on-machine measuring system for micro-structured surfaces. *Optics express*, 22(21), 25635-25650.
- Lin, D., Jiang, X., Xie, F., Zhang, W., Zhang, L., & Bennion, I. (2004). High stability multiplexed fibre interferometer and its application on absolute displacement measurement and on-line surface metrology. *Optics express*, 12(23), 5729-5734.
- Liu, D., & Yu, J. (2009). *Otsu method and K-means*. Paper presented at the Hybrid Intelligent Systems, 2009. HIS'09. Ninth International Conference on.
- Lou, S., Jiang, X., & Scott, P. J. (2013). Correlating motif analysis and morphological filters for surface texture analysis. *Measurement*, 46(2), 993-1001.
- Lou, S., Jiang, X., & Scott, P. J. (2013). Geometric computation theory for morphological filtering on freeform surfaces. *Proc. R. Soc. A*, 469(2159), 20130150.
- Lowe, D. G. (2004). Distinctive image features from scale-invariant keypoints. *International journal of computer vision*, 60(2), 91-110.
- Malacara, D. (2007). *Optical shop testing* (Vol. 59): John Wiley & Sons.
- Malacara, Z., & Servin, M. (2016). *Interferogram analysis for optical testing* (Vol. 84): CRC press.
- Maradudin, A. A. (2011). *Structured surfaces as optical metamaterials*: Cambridge University Press.
- Marvin, M. (1961). Microscopy apparatus. In: Google Patents.
- Michelson, A. A., & Morley, E. W. (1887). On the Relative Motion of the Earth and of the Luminiferous Ether. *Sidereal Messenger*, vol. 6, pp. 306-310, 6, 306-310.
- Mikolajczyk, K., & Schmid, C. (2004). Scale & affine invariant interest point detectors. *International journal of computer vision*, 60(1), 63-86.
- Mills, A., & Dudek, G. (2009). Image stitching with dynamic elements. *Image and Vision Computing*, 27(10), 1593-1602.
- Moschetti, G., Forbes, A., Leach, R. K., Jiang, X., & O'Connor, D. (2016a). Phase and fringe order determination in wavelength scanning interferometry. *Optics express*, 24(8), 8997-9012.
- Moschetti, G., Forbes, A., Leach, R. K., Jiang, X., & O'Connor, D. (2016b). Quadrature wavelength scanning interferometry. *Applied optics*, 55(20), 5332-5340.
- Moschetti, G., Muhamedsalih, H., Connor, D., Jiang, X., & Leach, R. K. (2015). Vertical axis non-linearities in wavelength scanning interferometry. In *In: Laser Metrology and Machine Performance XI, LAMDAMAP 2015. Huddersfield, UK* (pp. 31-39): EUSPEN.

- Muhamedsalih, H. (2013). *Investigation of wavelength scanning interferometry for embedded metrology*. University of Huddersfield,
- Muhamedsalih, H., Gao, F., & Jiang, X. (2012). Comparison study of algorithms and accuracy in the wavelength scanning interferometry. *Applied optics*, 51(36), 8854-8862.
- Muhamedsalih, H., Jiang, X., & Gao, F. (2013). Accelerated surface measurement using wavelength scanning interferometer with compensation of environmental noise. *Procedia CIRP*, 10, 70-76.
- Munroe, P. R. (2009). The application of focused ion beam microscopy in the material sciences. *Materials characterization*, 60(1), 2-13.
- Murphy, P., Forbes, G., Fleig, J., Dumas, P., & Tricard, M. (2003). Stitching interferometry: a flexible solution for surface metrology. *Optics and Photonics News*, 14(5), 38-43.
- Ng, T., & Thirunavukkarasu, S. (2007). Optical sensing limits in contact and bending mode atomic force microscopy. *Experimental Mechanics*, 47(6), 841-844.
- Niehues, J., Lehmann, P., & Xie, W. (2012). Low coherent Linnik interferometer optimized for use in nano-measuring machines. *Measurement Science and Technology*, 23(12), 125002.
- Onodera, R., & Ishii, Y. (1997). Fourier description of the phase-measuring process in two-wavelength phase-shifting interferometry. *Optics Communications*, 137(1-3), 27-30.
- Pellerin, J., Griffis, D., & Russell, P. (1990). Focused ion beam machining of Si, GaAs, and InP. *Journal of Vacuum Science & Technology B: Microelectronics Processing and Phenomena*, 8(6), 1945-1950.
- Persson, U. (1998). In-process measurement of surface roughness using light scattering. *Wear*, 215(1-2), 54-58.
- Pförtner, A., & Schwider, J. (2003). Red-green-blue interferometer for the metrology of discontinuous structures. *Applied optics*, 42(4), 667-673.
- Platform, A. (2014). Additive manufacturing: Strategic research agenda. *AM SRA final consultation document*. Google Scholar.
- Podulka, P., Pawlus, P., Dobrzański, P., & Lenart, A. (2014). *Spikes removal in Surface measurement*. Paper presented at the Journal of Physics: Conference Series.
- Postek, M. (1993). Scanning electron microscope metrology.
- Postek, M. T., & Joy, D. C. (1987). Submicrometer microelectronics dimensional metrology: scanning electron microscopy. *NBS Journal of Research*, 92(3), 205-228.
- Purcell, D., Suratkar, A., Davies, A., Farahi, F., Ottevaere, H., & Thienpont, H. (2010). Interferometric technique for faceted microstructure metrology using an index matching liquid. *Applied optics*, 49(4), 732-738.
- Raja, J., Muralikrishnan, B., & Fu, S. (2002). Recent advances in separation of roughness, waviness and form. *Precision Engineering*, 26(2), 222-235.
- Reason, R. (1961). Report on reference lines for roughness and roundness. *CIRP annals*, 11(2), 95-104.
- Rugar, D., & Hansma, P. (1990). Atomic force microscopy. *Physics today*, 43(10), 23-30.
- Ruiz, P. D., & Kaufmann, G. H. (1998). Evaluation of a scale-space filter for speckle noise reduction in electronic speckle pattern interferometry. *Optical Engineering*, 37(8), 2395-2402.
- Salvi, J., Matabosch, C., Fofi, D., & Forest, J. (2007). A review of recent range image registration methods with accuracy evaluation. *Image and Vision Computing*, 25(5), 578-596.
- Sandoz, P., Devillers, R., & Plata, A. (1997). Unambiguous profilometry by fringe-order identification in white-light phase-shifting interferometry. *Journal of modern optics*, 44(3), 519-534.

- Sandoz, P., Tribillon, G., & Perrin, H. (1996). High-resolution profilometry by using phase calculation algorithms for spectroscopic analysis of white-light interferograms. *Journal of modern optics*, 43(4), 701-708.
- Sarid, D., Iams, D., Weissenberger, V., & Bell, L. S. (1988). Compact scanning-force microscope using a laser diode. *Optics Letters*, 13(12), 1057-1059.
- Scherer, S. (2007). Fokus-variation zur optischen 3-D-Messung im Mikro-und Nanobereich. *Handbuch zur Industriellen Bildverarbeitung: Qualitätssicherung in der Praxis*, Fraunhofer IRB Verlag, 198-210.
- Schmaltz, G. Technische Oberflächenkunde (1936), 236. J. Springer.
- Schneir, J., Dagata, J. A., Harary, H. H., Evans, C. J., Melmed, A., Elswijk, H., & Sauvageau, J. (1989). *Scanning tunneling microscopy of optical surfaces*. Paper presented at the Surface Characterization and Testing II.
- Schulz-Ruhtenberg, M., Kolbusch, T., Abreu Fernandes, S., Wiesner, M., Melle, T., Bergfeld, S., . . . Ostendorf, A. (2014). Seminal Tools for Roll-to-Roll Manufacturing. *Laser Technik Journal*, 11(1), 21-25.
- Schwider, J., & Zhou, L. (1994). Dispersive interferometric profilometer. *Optics Letters*, 19(13), 995-997.
- Sedra, A. S., & Brackett, P. O. (1978). *Filter theory and design: active and passive*: Matrix Pub.
- Seewig, J. (2005). *Linear and robust Gaussian regression filters*. Paper presented at the Journal of Physics: conference series.
- Semwogerere, D., & Weeks, E. R. (2005). Confocal microscopy. *Encyclopedia of Biomaterials and Biomedical Engineering*, 23, 1-10.
- Singleton, L., Leach, R., Lewis, A., & Cui, Z. (2002). Report on the analysis of the MEMSTAND survey on Standardisation of MicroSystems Technology.
- Smith, K., & Oatley, C. (1955). The scanning electron microscope and its fields of application. *British Journal of Applied Physics*, 6(11), 391.
- Sobel, I., & Feldman, G. A 3x3 isotropic gradient operator for image processing (1968). *a talk at the Stanford Artificial Intelligence Project*.
- Søndergaard, R. R., Hösel, M., & Krebs, F. C. (2013). Roll-to-Roll fabrication of large area functional organic materials. *Journal of Polymer Science Part B: Polymer Physics*, 51(1), 16-34.
- Standard, I. 25178-2: 2012. *Geometrical product specifications (GPS). Surface texture: Areal. Part, 2*.
- Standards, V. Dimensional products, Step Height Standards (Quartz) [Online]. Available: <http://www.vlsistandards.com/products/dimensional/step.asp?SID=100>.
- Stover, J. C. (1995). *Optical scattering: measurement and analysis* (Vol. 2): SPIE optical engineering press Bellingham.
- Suen, S. T., Lam, E. Y., & Wong, K. K. (2006). *Curvature domain image stitching*. Paper presented at the Systems, Man and Cybernetics, 2006. SMC'06. IEEE International Conference on.
- Tafti, A. P., Kirkpatrick, A. B., Alavi, Z., Owen, H. A., & Yu, Z. (2015). Recent advances in 3D SEM surface reconstruction. *Micron*, 78, 54-66.
- Takeda, M., & Yamamoto, H. (1994). Fourier-transform speckle profilometry: three-dimensional shape measurements of diffuse objects with large height steps and/or spatially isolated surfaces. *Applied optics*, 33(34), 7829-7837.
- Tang, D., Gao, F., & Jiang, X. (2014). On-line surface inspection using cylindrical lens-based spectral domain low-coherence interferometry. *Applied optics*, 53(24), 5510-5516.
- Teague, E. C., Scire, F. E., Baker, S. M., & Jensen, S. W. (1982). Three-dimensional stylus

- profilometry. *Wear*, 83(1), 1-12.
- Technologies, A. C. F. o. A. M., & Terminology, A. C. F. o. A. M. T. S. F. o. (2012). *Standard Terminology for Additive Manufacturing Technologies*: ASTM International.
- Thiel, J., Pfeifer, T., & Hartmann, M. (1995). Interferometric measurement of absolute distances of up to 40 m. *Measurement*, 16(1), 1-6.
- Thompson, K. P., & Rolland, J. P. (2012). Freeform optical surfaces: a revolution in imaging optical design. *Optics and Photonics News*, 23(6), 30-35.
- Thunen, J. G., & Kwon, O. Y. (1983). *Full aperture testing with subaperture test optics*. Paper presented at the Wavefront sensing.
- Tian, A., Liu, X., Chetwynd, D., & Cai, Z. (2007). Stylus contact on short wavelength random surfaces: a simulation study. *Measurement Science and Technology*, 18(6), 1694.
- Tomlinson, C. H. (1919). Car and electric coupling device. In: Google Patents.
- Triantaphyllou, A., Giusca, C. L., Macaulay, G. D., Roerig, F., Hoebel, M., Leach, R. K., . . . Milne, K. A. (2015). Surface texture measurement for additive manufacturing. *Surface Topography: Metrology and Properties*, 3(2), 024002.
- Tseng, A. A., Notargiacomo, A., & Chen, T. (2005). Nanofabrication by scanning probe microscope lithography: A review. *Journal of Vacuum Science & Technology B: Microelectronics and Nanometer Structures Processing, Measurement, and Phenomena*, 23(3), 877-894.
- Vaghela, D., & Naina, P. (2014). A review of image mosaicing techniques. *arXiv preprint arXiv:1405.2539*.
- Van Loenen, E., Dijkkamp, D., Hoeven, A., Lenssinck, J., & Dieleman, J. (1990). Evidence for tip imaging in scanning tunneling microscopy. *Applied physics letters*, 56(18), 1755-1757.
- Vincent, L. (1994). Morphological area openings and closings for grey-scale images. In *Shape in Picture* (pp. 197-208): Springer.
- VLSI Standards. Dimensional products, Step Height Standards (Quartz) [Online]. Available: <http://www.vlsistandards.com/products/dimensional/step.asp?SID=100>.
- Volkert, C. A., & Minor, A. M. (2007). Focused ion beam microscopy and micromachining. *MRS bulletin*, 32(5), 389-399.
- Von Weingraber, H. (1956). Zur definition der Oberflächen raugheit Werk Strattstechnik. *Masch, Bass*, 46.
- Vorburger, T. V., Marx, E., & Lettieri, T. R. (1993). Regimes of surface roughness measurable with light scattering. *Applied optics*, 32(19), 3401-3408.
- Vorburger, T. V., Rhee, H.-G., Renegar, T. B., Song, J.-F., & Zheng, A. (2007). Comparison of optical and stylus methods for measurement of surface texture. *The International Journal of Advanced Manufacturing Technology*, 33(1-2), 110-118.
- Walsh, C. (1987). Measurements of absolute distances to 25 m by multiwavelength CO<sub>2</sub> laser interferometry. *Applied optics*, 26(9), 1680-1687.
- Wang, C., Caja, J., & Gómez, E. (2018). Comparison of methods for outlier identification in surface characterization. *Measurement*, 117, 312-325.
- Ward, J., Pannell, C., Wachman, E., & Seale, W. (2006). Applications of acousto-optic devices for spectral imaging systems. In: NEOS Technologies, USA.
- Whitehouse, D. (1982). The parameter rash—is there a cure? *Wear*, 83(1), 75-78.
- Whitehouse, D., & Archard, J. (1969). *The properties of random surfaces in contact*. Paper presented at the Surface Mechanics, Proceedings of the ASME Annual winter meeting.
- Whitehouse, D. J. (1997). Surface metrology. *Measurement Science and Technology*, 8(9), 955.
- Whitehouse, D. J. (2004). *Surfaces and their Measurement*: Elsevier.

- Whitehouse, D. J. (2010). *Handbook of surface and nanometrology*: CRC press.
- Wickramasinghe, H. K. (1990). Scanning probe microscopy: current status and future trends. *Journal of Vacuum Science & Technology A: Vacuum, Surfaces, and Films*, 8(1), 363-368.
- Wiesendanger, R. (1994). *Scanning probe microscopy and spectroscopy: methods and applications*: Cambridge University Press.
- Willmann, J., Stocker, D., & Dörsam, E. (2014). Characteristics and evaluation criteria of substrate-based manufacturing. Is roll-to-roll the best solution for printed electronics? *Organic Electronics*, 15(7), 1631-1640.
- Wilson, L., Matsudaira, P. T., Jena, B. P., & Horber, J. H. (2002). *Atomic force microscopy in cell biology* (Vol. 68): Academic Press.
- Wilt, N. (2013). *The cuda handbook: A comprehensive guide to gpu programming*: Pearson Education.
- Wong, Y.-f. (1993). Clustering data by melting. *Neural computation*, 5(1), 89-104.
- Wong, Y.-F. (1995). Nonlinear scale-space filtering and multiresolution system. *IEEE Transactions on image processing*, 4(6), 774-787.
- Xie, G., Chang, J., Zhang, K., Zhou, J., & Niu, Y. (2016). Off-axis three-mirror reflective zoom system based on freeform surface. *Frontiers of Optoelectronics*, 9(4), 609-615.
- Xiong, Y., & Turkowski, K. (1998). *Registration, calibration and blending in creating high quality panoramas*. Paper presented at the Applications of Computer Vision, 1998. WACV'98. Proceedings., Fourth IEEE Workshop on.
- Xu, J., & Stroud, R. (1992). *Acousto-optic devices: principles, design, and applications* (Vol. 12): Wiley-Interscience.
- Yamaguchi, I., Yamamoto, A., & Kuwamura, S. (1998). Speckle decorrelation in surface profilometry by wavelength scanning interferometry. *Applied optics*, 37(28), 6721-6728.
- Ye, J., Chen, L., Li, X., Yuan, Q., & Gao, Z. (2017). Review of optical freeform surface representation technique and its application. *Optical Engineering*, 56(11), 110901.
- Yoshizawa, T. (2015). *Handbook of optical metrology: Principles and Applications*: CRC Press.
- Zeng, W., Jiang, X., & Scott, P. (2011). A generalised linear and nonlinear spline filter. *Wear*, 271(3-4), 544-547.
- Zhang, T., Gao, F., & Jiang, X. (2017). Surface topography acquisition method for double-sided near-right-angle structured surfaces based on dual-probe wavelength scanning interferometry. *Optics express*, 25(20), 24148-24156.
- Zhang, T., Gao, F., Martin, H., & Jiang, X. A method for inspecting near-right-angle V-groove structured surfaces based on dual-probe wavelength scanning interferometry. *The International Journal of Advanced Manufacturing Technology* (accepted, in- press).
- Zhang, T., Gao, F., Muhamedsalih, H., Lou, S., Martin, H., & Jiang, X. (2018). Improvement of the fringe analysis algorithm for wavelength scanning interferometry based on filter parameter optimization. *Applied optics*, 57(9), 2227-2234.
- Zhou, W., & Wang, Z. L. (2007). *Scanning microscopy for nanotechnology: techniques and applications*: Springer science & business media.
- Zhu, P., & Wang, K. (2012). Single-shot two-dimensional surface measurement based on spectrally resolved white-light interferometry. *Applied optics*, 51(21), 4971-4975.
- Zitova, B., & Flusser, J. (2003). Image registration methods: a survey. *Image and Vision Computing*, 21(11), 977-1000.

## Publications and Awards

### Refereed Journal Papers

- T. Zhang, F. Gao and X. Jiang. "Surface topography acquisition method for double-sided near-right-angle structured surfaces based on dual-probe wavelength scanning interferometry," *Optics Express*, 25(20), 24148-24156 (2017).
- T. Zhang, F. Gao, H. Muhamedsalih, S. Lou, H. Martin and X. Jiang. "Improvement of the fringe analysis algorithm for wavelength scanning interferometry based on filter parameter optimization," *Applied Optics*, 57, 2227-2234 (2018).
- T. Zhang, F. Gao, H. Martin and X. Jiang. "A method for inspecting near-right-angle V-groove surfaces based on dual-probe wavelength scanning interferometry," *The International Journal of Advanced Manufacturing Technology* (accepted, in press).

### Refereed Conference Papers

- T. Zhang, F. Gao and X. Jiang. "A method for inspecting double-sided high-sloped structured surfaces based on dual-probe wavelength scanning interferometry," *The 13th International Symposium on Measurement Technology and Intelligent Instruments*, Xi'an, China.

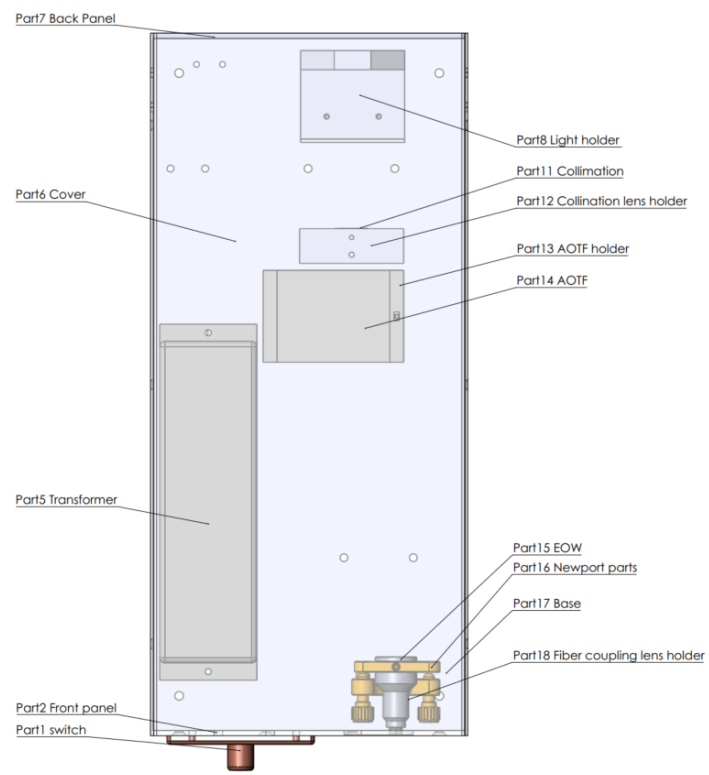
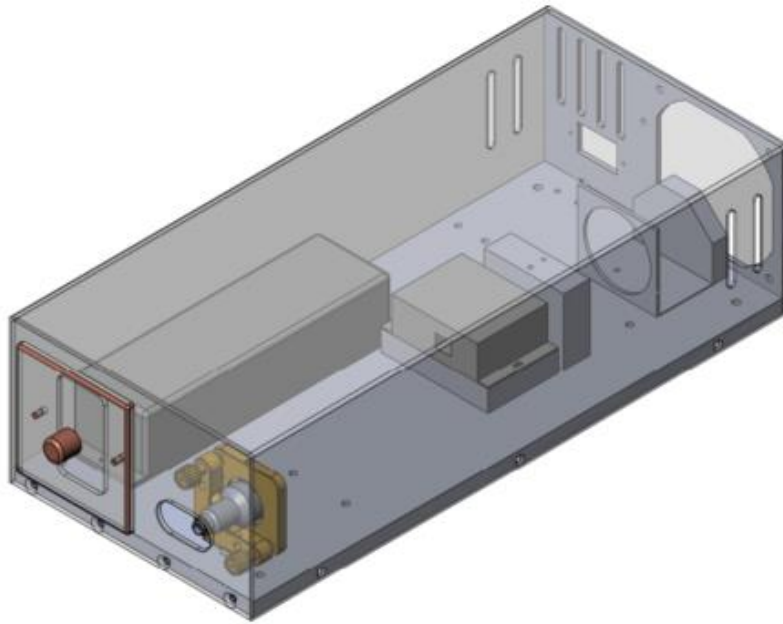
### Awards

- T. Zhang, F. Gao and X. Jiang. **Best paper awards.** *The 13th International Symposium on Measurement Technology and Intelligent Instruments*, Xi'an, China.

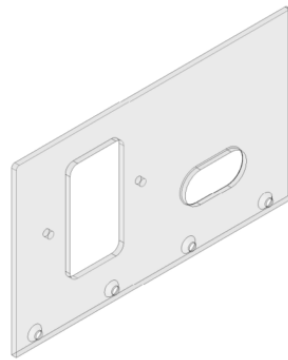
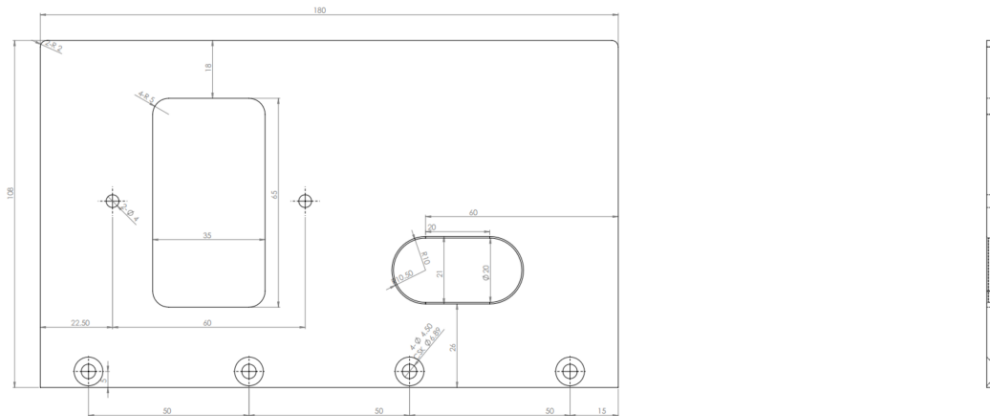


# Appendix B. The light box design

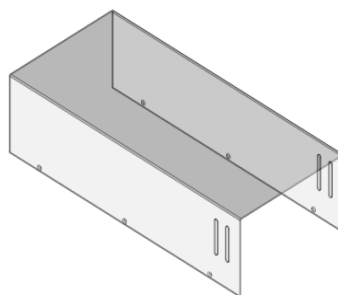
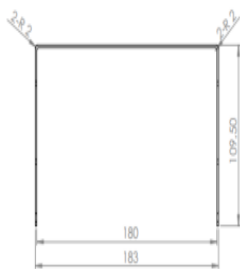
## Assembly



## Front panel

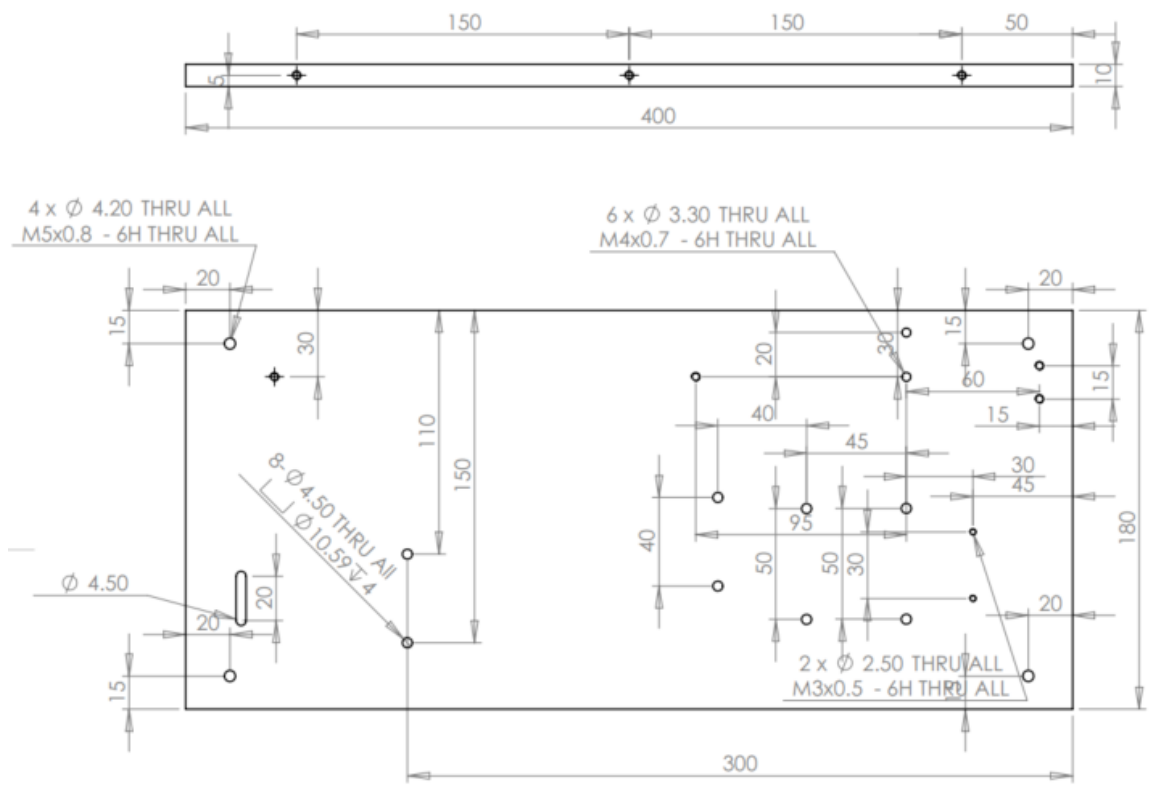


## Cover

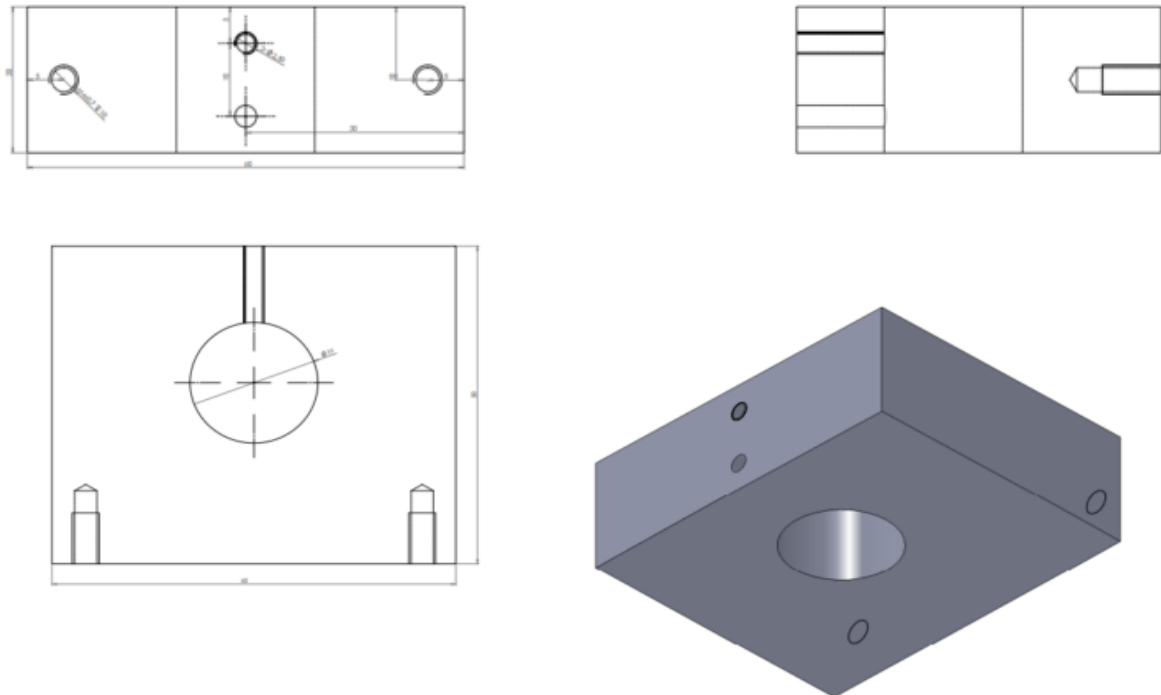




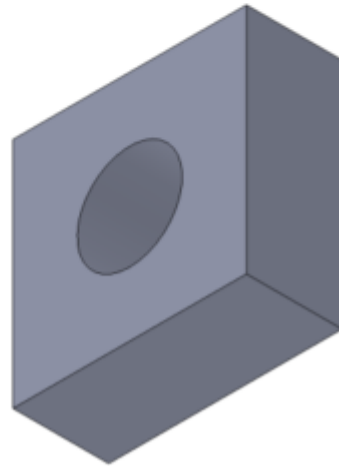
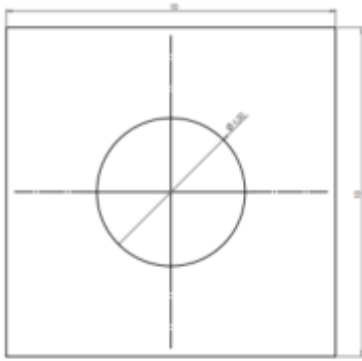
## Base



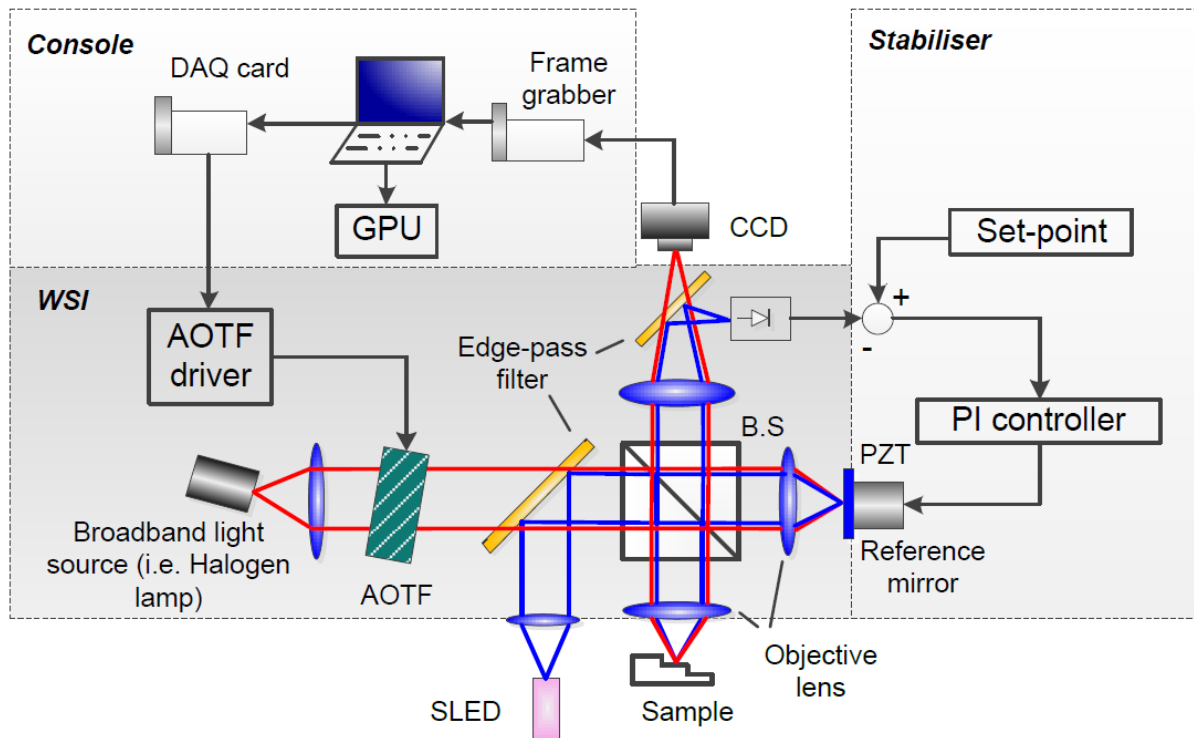
## Collimation lens holder



## Fibre coupler holder block



## Appendix C. A brief introduction about Muhamedsalih's thesis



As illustrated in the above schematic, the system can be divided into 3 parts, a wavelength scanning interferometer which was employed as a measurement probe, a console for controlling the whole system and analysing the captured fringe patterns, and a stabiliser using an active servo control system to compensate for the environmental disturbances.

The illumination scheme of the system adopts a combination of a visible light source and an infrared light source. The visible light source comprising a tungsten-halogen bulb and an acousto-optic tuneable filter (AOTF) is for measurement, while the infrared source adopting a super luminescent light emitting diode (SLED) is for stabilisation. The system is illuminated simultaneously by the two light sources. There are two interferometers sharing a same optical path inside the system. One is the wavelength scanning interferometer for measurement and the other one plays a role of a feedback sensor for stabilising the system.

The interferograms are captured by a high-speed CCD, and then are transferred to the console which performs the processing to determine the topography of the specimen surface. A graphic processing unit (GPU) is used to speed up the processing. Compared to a central processing unit (CPU), the GPU can perform highly-parallel processing with a massive number of threads

using many cores, which significantly increases the overall measurement throughput and potentially enables the real-time/online measurement. The specification of the system is listed in the following table:

Performance target		Value
Measurement range		> focal depth of the objective lens (e.g. > 92 $\mu\text{m}$ for 2X objective)
Vertical resolution		< 30 nm
Lateral resolution		Diffraction limited
Measurement time	Capturing time	< 3 s
	Analysis time	< 2 s
Stabilisation bandwidth		> 200 Hz

The system was verified to be able to achieve nanometre scale vertical accuracy when measuring step-height specimens. The following table compares the measurement results of a 4.707  $\mu\text{m}$  standard step-height sample before and after switching on the stabiliser. The standard deviation of the measurement results is 6.18 nm and 3.5 nm, respectively. The stabiliser improves the repeatability by nearly 50%.

NO.	Measured height value ( $\mu\text{m}$ )		NO.	Measured height value ( $\mu\text{m}$ )	
	Stabilisation off	Stabilisation on		Stabilisation off	Stabilisation on
1	4.72	4.691	8	4.718	4.697
2	4.723	4.688	9	4.718	4.689
3	4.714	4.685	10	4.727	4.692
4	4.717	4.695	11	4.705	4.689
5	4.719	4.693	12	4.71	4.692
6	4.726	4.694	13	4.726	4.697
7	4.72	4.689	14	4.722	4.694

## Appendix D. Simulation code for fringe analysis

```
%Fringe Analysis using FFT
clc
clear;
close all

FrameNumber=256*1;
m=1;
A=60;
B=40;

% Read the capture Data into 3D matrix (bdouble)
StartHeight=5000;
EndHeight=30000;
SF=EndHeight-StartHeight+1;
hTrue=linspace(StartHeight,EndHeight,SF);

LambdaS=683.42; % Start wavelength (nm)
LambdaE=590.98; % End wavelength (nm)
KvStart=1/LambdaS;
KvEnd=1/LambdaE;

Kv=linspace(KvStart,KvEnd,FrameNumber);
tic
for px=1:SF
I=B*cos(4*pi*Kv*hTrue(px));
I=A+awgn(I, 2, 'measured');
yt1=double(I); % (1) gathering the pixel values; once at a time
w=hamming(FrameNumber);
% w=hann(FrameNumber);
% w=rectwin(FrameNumber);
% w=Gaussian(FrameNumber);
% yt1=yt1.*w';
fftResult=(1/FrameNumber)*fft(yt1); % (2) find the fft
% fftResult = fftResult.*w';
signalABS=abs(fftResult);
[m1,l1]=max(signalABS(2:FrameNumber/2));
l1=l1+1
% [m3,l2]=max(signalABS((l1+30):FrameNumber/2));
% ---END-----

% if (SNR_yt1(px)>= 0)
fftFilter(1:FrameNumber)=0; % (3) filter out the unwanted DC and phase conjugate
% fftFilter(3:15)=fftResult(3:15);
halfBW=1;
```

```

if(round(l1-halfBW)>2)
    w1=round(l1-halfBW);
else
    w1=2;
end

fftFilter(w1:round(l1+halfBW))=fftResult(w1:round(l1+halfBW));
% fftFilter(2:26)=fftResult(2:26);

% if(round(l1-2)>2)
%     w1=round(l1-2);
% else
%     w1=2;
% end
% b = fir1(256, [w1/256 (l1+halfBW)/256]);
% ifftFilter=filter(b, 1, yt1);
ifftFilter=ifft(fftFilter);           % (4) inverse fft to retrieve the 1/2Be^(phase)
phase=imag(log(ifftFilter));          % (5) extract the phase from the imaginary
phase_set(1)=0;                       % (6) phase unwrapping

for i=1:length(phase)-1               % (6.a) construct the Phase set function
    if abs(phase(i+1)-phase(i)) >(2*pi*0.4)
        phase_set(i+1)=phase_set(i)+ 2*pi;
    else
        phase_set(i+1)=phase_set(i);
    end
end

phase_final = phase + phase_set;      % (6.b) add the Phase set to the determined phase

%%%%%%%%%% Linear Fitting using least square
approach%%%%%%%%%%
% Numerical Methods for Engineers and Scientists 2nd Edition 2001 page 228
% by Marcel Dekker
%-----
C=0;
D=0;
E=0;
F=0;
CutoffLength=50;
CropStart=CutoffLength+1;
CropEnd=FrameNumber-CutoffLength;
N=CropEnd-CropStart+1;

for(i=CropStart:CropEnd)
    C=C+i;
    D=D+phase_final(i);
    E=E+(i*i);

```

```

    F=F+(phase_final(i)*i);
end

slop=(F-(1/N)*D*C)/(E-(1/N)*(C^2));
DC=((1/N)*D)-((slop/N)*C);
for i=1:FrameNumber
    PhaseFit(i)=DC+(slop*i);
end

% phase = phase - DC;
% plot(PhaseFit,'k')
%%%%%%%%%%%%%%%%%%%%%%%%%%%%%%%%%%%%%%%%%%%%%%%%%%%%%%%%%%%%%%%%%%%%%%%%
% ArealHeight(px,py)=(phase_final(FrameNumber-5)-
phase_final(5))*(1/(4*pi*(Kv(FrameNumber-5)-Kv(5)))); % (7) calculate the height
HeightCal(px)=(PhaseFit(FrameNumber)-PhaseFit(1))*(1/(4*pi*(Kv(FrameNumber)-
Kv(1)))); % (7) calculate the height

%--- Modified calculation by Prashant-----
for sample_num = 1:length(phase)
    N (sample_num) = -round((phase(sample_num)-
4*pi*Kv(sample_num)*HeightCal(px))/(2*pi)); % fringe order calculation using the slope &
z
    deltaD (sample_num) =
((1/(4*pi*Kv(sample_num)))*(phase(sample_num)+2*pi*(N(sample_num))));% calculated
height using the fringe order method
end

% hCal(px)=mean(deltaD);
% hCal(px)=deltaD(250);
hCal(px)=deltaD(128);
%--- End-----

% else
%   HeightCal(px)=NaN;
%   hCal(px)=NaN;
% end

end

toc

Error=abs(hTrue-HeightCal);
ErrorModified=abs(hTrue-hCal);

figure;
plot(hTrue,'k')
hold on

```

```

plot(HeightCal,'r')
plot(hCal,'g')
xlabel('Sampling number')
ylabel('Height (nm)')
figure;
plot(hTrue, Error,'k')
hold on
% plot(hTrue, ErrorModified,'r')
xlabel('Sampling number')
xlabel('Height(half OPD/nm)', 'FontSize', 22)
ylabel('Error (nm)', 'FontSize', 22)
set(gca,'fontsize',22)

figure;
% plot(hTrue, Error,'k')
hold on
plot(hTrue, ErrorModified,'r')
xlabel('Sampling number')
xlabel('Height(half OPD/nm)', 'FontSize', 22)
ylabel('Error (nm)', 'FontSize', 22)
set(gca,'fontsize',22)

```

## Appendix E. Feature extraction code

### SEM data

```
clc
clear

% SEM Segmentation
load TOP_HALF
figure(1)
subplot(3,2,1)
title('Raw'); hold on
imshow(top_half);

%% Denoise
% h = fspecial('gaussian');
% top_half_Gau = imfilter(top_half, h);

subplot(3,2,2); title('Denoise'); hold on
top_half_Med = medfilt2(top_half, [5 5]);
imshow(top_half_Med);

%% Edge detection
% subplot(2,2,3); title('Edge detection'); hold on
% top_half_Canny = edge(255-top_half_Med, 'sobel');
% imshow(top_half_Canny);

%% Otsu
subplot(3,2,3); title('Otsu'); hold on
top_half_adjust = imadjust(top_half_Med);
level = graythresh(top_half_adjust);
top_half_Otsu = im2bw(top_half_adjust, level);
imshow(top_half_Otsu);

%% Morphological closing
subplot(3,2,4); title('Morphological closing'); hold on
SE = strel('square', 6);
top_half_Morph = imopen(top_half_Otsu, SE);
imshow(top_half_Morph);
%% SECTION TITLE
% DESCRIPTIVE TEXT

%% Fill the holes
subplot(3,2,5); title('Fill holes'); hold on
top_half_Fill = imfill(top_half_Morph, 'holes');
% top_half_Fill = imfill(top_half_Fill, 'holes');
imshow(top_half_Fill);
```

```

%% Edge detection
subplot(3,2,6); title('Edge detection'); hold on
% top_half_Sobel = edge(top_half_Fill, 'sobel');
se = strel('square',5);
top_half_erode = imerode(top_half_Fill, se);
top_half_edge = top_half_Fill - top_half_erode;
imshow(top_half_edge);

```

```

figure(2)
clf
imshow(top_half_edge); hold on

```

## Topography data

```

clear all;
clc;

[h1,SPACING1,FILEINFO1] = ReadSUR ( '\dual_probe\3D.sur' );
a1=SPACING1(2)*(1:size(h1,1));
b1=SPACING1(1)*(1:size(h1,2));
[X1,Y1]=meshgrid(b1,a1);
Z1=h1/1000;
figure;
surf(X1,Y1,Z1);
xlabel('X');
ylabel('Y');
zlabel('Z');
hold on
axis tight
%axis equal
shading interp

filty = fspecial('sobel');
filtx = filty;
Z1y = imfilter(double(Z1), filty, 'replicate');
Z1x = imfilter(double(Z1), filtx, 'replicate');
gradmag = sqrt(Z1x.^2 + Z1y.^2);

delta=max(max(gradmag))-min(min(gradmag));
im=imhmin(gradmag,delta*6/100,8);
L1 = watershed(im,8);
edge=L1==0;
figure;
imshow(edge);

```

## Appendix F. Taylor Hobson CCI 3000 specification

<b>Optical specifications</b>					
Magnification	X 2.5	X 5	X 10	X 20	X 50
Numerical aperture	0.075	0.13	0.3	0.4	0.55
Working distance (mm)	10.3	9.3	7.4	4.7	3.4
Optical resolution ( $\mu\text{m}$ )	7.2	3.6	1.8	0.9	0.36
Maximum slope (degrees)	2.0	4.0	7.7	14.6	27.7
Measurement area (mm)	7.2 x 7.2	3.6 x 3.6	1.8 x 1.8	0.9 x 0.9	0.36 x 0.36
Lateral sampling resolution ( $\mu\text{m}$ )	7	3.5	1.75	0.88	0.35

<b>System specifications</b>	
<b>Performance</b>	
Vertical range [Z]	100 $\mu\text{m}$
Vertical resolution (max)	0.1 $\text{\AA}$ (10pm)
RMS repeatability [Z]	0.03 $\text{\AA}$ (3pm)
Vertical scanning speed (max)	7mm / second
Measurement range [X, Y]	0.36mm <sup>2</sup> - 7.2mm <sup>2</sup>
Number of measurement points	1,048,576 (1024 x 1024 pixel array)
Lateral resolution [X, Y]	0.36 $\mu\text{m}$ (max)
Step height repeatability	0.1nm (25mm step)
Linearity [Z]	0.03% of measured value
Pixel noise [Z]	0.2nm
Surface reflectivity	0.3% - 100%
Component size (max)	X and Y = 300mm; Z = 200mm
Component weight (max)	10 kg
Measurement Time	Typical 10-20 seconds

<b>Installation conditions</b>	
Temperature / humidity	15 - 30C° / 80% non-condensing
Vibration	Pneumatic anti-vibration system included
Dimensions (floor space)	750mm wide x 500mm deep